



HAL
open science

Theory of electrostatic probes in a flowing continuum low-density plasma

Chang Jen-Sin, J.G. Laframboise

► **To cite this version:**

Chang Jen-Sin, J.G. Laframboise. Theory of electrostatic probes in a flowing continuum low-density plasma. [Rapport de recherche] Note technique CRPE n° 30, Centre de recherches en physique de l'environnement terrestre et planétaire (CRPE). 1976, 126 p. hal-02191402

HAL Id: hal-02191402

<https://hal-lara.archives-ouvertes.fr/hal-02191402>

Submitted on 23 Jul 2019

HAL is a multi-disciplinary open access archive for the deposit and dissemination of scientific research documents, whether they are published or not. The documents may come from teaching and research institutions in France or abroad, or from public or private research centers.

L'archive ouverte pluridisciplinaire **HAL**, est destinée au dépôt et à la diffusion de documents scientifiques de niveau recherche, publiés ou non, émanant des établissements d'enseignement et de recherche français ou étrangers, des laboratoires publics ou privés.

12182 (3)
**CENTRE NATIONAL D'ETUDES
DES TELECOMMUNICATIONS**

**CENTRE NATIONAL DE LA
RECHERCHE SCIENTIFIQUE**

**CENTRE DE
RECHERCHES
EN PHYSIQUE DE
L'ENVIRONNEMENT
TERRESTRE
ET PLANETAIRE**

CRPE

**NOTE TECHNIQUE
CRPE / 30**

*Theory of electrostatic probes
in a flowing continuum low-density plasma*

by

JEN-SHIH CHANG

J.G. LAFRAMBOISE

B

CENTRE NATIONAL D'ETUDES
DES TELECOMMUNICATIONS

CENTRE NATIONAL DE
LA RECHERCHE SCIENTIFIQUE

CENTRE DE RECHERCHE EN PHYSIQUE DE
L'ENVIRONNEMENT TERRESTRE ET PLANETAIRE

NOTE TECHNIQUE CRPE/30

THEORY OF ELECTROSTATIC PROBES IN A
FLOWING CONTINUUM LOW-DENSITY PLASMA

by

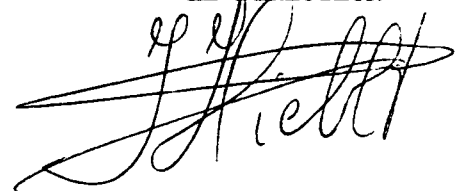
JEN-SHIH CHANG and J.G. LAFRAMBOISE

CRPE/PCE

45045 ORLEANS-LA-SOURCE, FRANCE

SEPTEMBRE, 1976

LE DIRECTEUR

A handwritten signature in black ink, appearing to be 'J. Laframboise', written over the printed text 'LE DIRECTEUR'.

SUMMARY

A method has been developed and used to obtain theoretical predictions of the current collected from a continuum, incompressible flowing low charge density plasma by an electrostatic probe having spherical or cylindrical symmetry. The solutions for the low density continuum case, i.e. with mean free path \ll probe radius \ll Debye length, are calculated for Reynolds numbers from 0.1 to 100 for cylinders, 0.1 to 60 for spheres, for charged particle Schmidt numbers from 0 to 10^5 , and for scaled probe potentials from -12 to 10 for arbitrary ion-to-electron temperature ratios. Each current collection result has been computed to a relative accuracy of 2% or better in an average time of approximately 20 minutes on the CDC 6600 at CNES, including a relative accuracy of 0.4% or better at stationary conditions compared with the analytic solution. The charge transport equations are solved using upwind difference methods developed for time independent situations. Numerical solutions of the Navier-Stokes equations by other authors are used for the neutral flow. The electric potential profiles used for the cylinder are logarithmic, obtained by using the Laplace potential at the equator of a prolate spheroid, approximated for radii \ll major axis. The electric potential profiles used for the sphere are proportional to r^{-1} , the Laplace potential.

The numerical results show that: (1) For a probe at retarding

potentials, the effects of the flow increase with potential, and the usual retarding potential method for temperature determination of electrons leads to large errors, (2) For small potentials, the effect of the flow is to smooth the "knee" of the probe characteristics and to render more imprecise the determination of the space potential. (3) At a large enough attracting potential, the linear dependence for probe current from stationary theory is recovered as one would expect. (4) The probe surface current densities become unsymmetrical when flow is increased. (5) Recirculation in the neutral wake behind the body has larger effects on downstream than upstream probe surface current density. (6) In the presence of flow, the profiles of net charge density can include several regions of alternating sign downstream of the probe.

Computed charge densities and probe surface current densities are presented graphically. Computed probe characteristics are presented in graphical and tabular form. A listing is included of the Fortran programs used to obtain these results.

ACKNOWLEDGMENTS

We wish to express our special appreciation to K. Kodera for valuable discussions and comments, and to Dr. L.R.O. Storey for varieties of assistance too numerous to list.

We are indebted to the C.N.E.S., Toulouse and Bretigny, to the C.R.P.E., Orleans-La Source, and to York University, Toronto, Canada, for the use of their CDC 7600, CDC 6600, IBM 360 and IBM 370 computers.

Special thanks are due to Dr. S.C.R. Dennis (University of Western Ontario, London, Canada), J.D. Hudson (University of Sheffield, England), and K. Takami (Tokyo University, Japan) for providing us with numerical viscous flow data.

We wish to thank the Director of C.R.P.E. for the opportunity to conduct this study.

TABLE OF CONTENTS

List of Symbols

1. Introduction	9
2. Statement of the Problem	15
3. Basic Equations and Boundary Conditions	17
3.1 Cylindrical Coordinates	18
3.2 Spherical Coordinates	21
4. Numerical Methods and Calculation Procedure	23
4.1 Time Independent Upwind Difference Methods	24
4.2 Numerical Integration and Difference Methods	37
4.3 Calculation Procedure	40
5. Results and Discussion for Cylinder in Cross-Flow	43
5.1 Charge Density Profiles	43
5.2 Local Current Density	45
5.3 Total Probe Current	47
5.4 Application to Presence of Magnetic Field	50
6. Results and Discussion for Spherical Probe.	51
6.1 Charge Density Profiles	51
6.2 Local Current Density	52
6.3 Total Probe Current	54
7. Comparison with Experiments and Other Theories	57
7.1 Cylinder in Cross-Flow	59
7.2 Sphere in Flow	62

8. Concluding Remarks

65

References

68

Tables

Figures

Appendix A: Application of Theory to Quasi-Neutral Conditions:

$$R_p / \lambda_D \rightarrow \infty$$

Appendix B: Application to Plasma Diagnostic Method

Appendix C: Computer Program Listings

List of Symbols

- D diffusion coefficient
- e magnitude of electron charge
- h shape constant
- I total collected current for spherical probe; total collected current per unit length for cylindrical probe.
- J local current density
- k Boltzmann's constant
- $K_0(x)$ modified Bessel function of zero order
- l probe length
- N number density
- R radius
- Re Reynolds number based on diameter, $2U_{\infty} R_p / \nu$
- S surface area
- Sc Schmidt number, ν/D
- T temperature
- U flow velocity
- V potential
- λ_D Debye length, $(\epsilon_0 kT_e / e^2 N_{\infty})^{1/2}$
- λ mean free path
- μ mobility
- ψ stream function
- ν kinematic viscosity
- θ angle

Nondimensional Symbols

$i = I/I_d$, total current, $I_d = eN_\infty DS_p/R_p$

$j = JR_p/N_\infty D$, local current

$L =$ major to minor axis ratio of prolate spheroid used to model cylindrical probe; for relation between L and Λ see p. 11.

$n = N/N_\infty$, number density

$Re = 2U_\infty R_p/\nu$, Reynolds number

$Ra = 2U_\infty R_p/D$, diffusion Reynolds number

$Sc = \nu/D$, Schmidt number

$u = U/U_\infty$, flow velocity

$\varphi = eV/kT_e$, potential

$\epsilon = T/T_e$, temperature ratio

$\Lambda = l/R_p$; length of cylindrical probe. For relation between Λ and L see page 11.

Subscripts

a ambipolar

b boundary

c charged particle

d diffusion

e electron

i ion

K iteration number

k, l, m grid point

o at space potential

p probe

r radial component

z axial component

θ angular component

∞ at infinite radius

Note: Additional symbols are defined as they occur in the text.

CHAPTER I

1. INTRODUCTION

A method has been developed and used to calculate the space charge density profiles near spherically and cylindrically symmetric electrostatic probes immersed in a flowing low charge density continuum plasma, and thereby to calculate the current collected by such probes from the surrounding plasma. A low density continuum plasma is one in which mean free path \ll probe radius \ll Debye length.

An electrostatic probe is a piece of conducting material that is inserted into a plasma on a mechanical support which provides electrical connection from the probe to external circuitry (Fig. 1.1). The probe potential is varied, slowly enough to eliminate transient effects, over a range that normally includes the plasma potential. The electric current collected by the probe from the plasma is recorded as a function of probe potential. The shape of this curve, known as the "probe characteristic", depends on the composition, the flow velocity and the thermodynamic state of the plasma, and therefore information about these plasma state parameters can often be obtained from one simple curve. Compared to many other diagnostic tools the probe is distinguished by the possibility of direct local measurements of plasma parameters. These facts enable the experimenter to use plasma probes as instruments to measure the state parameters of plasmas

that exist either in the laboratory or in nature. Figure 1.2 shows the general appearance of a probe characteristic. Two phenomena which appear in figure 1.2, i.e. secondary ionization caused by accelerated electrons and electron emission from probe surface due to ion bombardment, are not studied in the present work.

Two important examples of low density continuum plasmas exist in nature, that is planetary lower ionospheres and stratospheres, and electrostatic probes are frequently carried by planetary probes or balloons in order to investigate their surroundings.

The local disturbances created in the ionosphere or stratosphere by the entire planetary probe or balloon can often be analysed using theories developed for electrostatic probes, since the vehicle itself constitutes a conducting object immersed in a plasma; in this case there is no external connection to allow current to drain off, and the planetary probe or balloon will arrive at an equilibrium or "floating" potential at which it collects no net current (Fig. 1.2).

Recent developments of flowing afterglow plasmas, flowing gaseous lasers, diffusion flame plasmas, discharge physics and atmospheric electricity have created a need for probe measurements in conditions of low charge density ($< 10^8 \text{cm}^{-3}$) and medium neutral pressure ($> 1 \text{ torr}$) plasma, i.e. under conditions in which the Debye

length may be relatively large but the mean free path is relatively small. The approximate range of probe conditions in these various flowing plasmas is shown in figure 1.3. Also, in probe measurements it is always advantageous to use the smallest probe size consistent with electrical and mechanical constraints, in order to get minimum plasma disturbance and maximum localization of measurements. In this work, we develop a numerical method to obtain the probe characteristic for the limit in which ionization is slight enough that Debye length \gg probe radius, so that the electric potential profile surrounding the probe obeys Laplace's equation. Numerical solutions by other authors are used for the neutral flow.

In order to solve the partial differential equations arising in this problem, we have developed an "upwind difference method" for the time independent case, in order to obtain faster computation time and stability of calculations (Chapter 4).

In Chapters 5 and 6, we present results of computations carried out for cylinders in cross-flow and spheres in flow. We use the numerical results to demonstrate that the usual retarding potential method for electron temperature measurement leads to serious error in flowing continuum conditions. We also examine the charge density distributions around spheres and cylinders in the presence of flow. Then we find that the profiles of net charge density can include several regions of alternating sign downstream of the probe. Comparisons with experiments and other

theories are discussed in Chapt. 7. The application of the present work to the limit $R_p/\lambda_D \rightarrow \infty$ is discussed in Appendix A.

1.1 SUMMARY OF INCOMPRESSIBLE FLOWING CONTINUUM PROBE THEORIES

A summary of probe theories for both spheres and cylinders in incompressible flowing plasmas is shown in figure 1.4. The present work is for Debye ratio $R_p/\lambda_D = 0$ (Chapts. 5 and 6) and ∞ (Appendix A), values for which no previous theories exist.

The general theory for probes in flowing plasmas has been first done by Lam (1964). He assumed that under the condition $\lambda_D/R_p \ll Re^{-1/2}$, the neutral flow affects the charge density only in the quasi-neutral region, since the plasma sheath is much smaller than the neutral flow boundary layer. He obtained a general expression for flow effects on current-voltage characteristics. Clements and Smy (1969)(1970) obtained approximate solutions for spheres and cylinders by combining the model of Lam with an assumed circular sheath edge centered downstream of the probe center. Huggins (1974) used the same model with an approximate thick sheath solution by Keil (1968) to extend the theory to $R_p/\lambda_D \sim 1$ for spheres. Hirano (1973) obtained an approximate solution for cylinders by applying the model of Lam with his own approximate neutral flow solution at the front stagnation point. Yastrebov (1972) obtained solutions for the sphere front stagnation point by using the incompressible nonviscous flow solution for $R_p/\lambda_D \geq 1$.

All of these theories deal primarily with conditions in which the neutral Reynolds number Re is comparable with the charged particle diffusion Reynolds number Ra , i.e. the charged particle Schmidt number $Sc_c = Ra/Re$ is of

order unity. But the important range of the diffusion Reynolds number is 0 to 10^4 , i.e. 0.1 to 10^2 times larger than the neutral Reynolds number, in the applications indicated in figure 1.3 for low density plasmas. Kodera (1975) used the analytical solutions of Van Dyke (1964, p.159) to estimate the neutral flow for Reynolds numbers 0 to 10^3 at the front stagnation point. He obtained solutions for $R_p/\lambda_D \rightarrow 0$, and Ra from 0 to 10^4 .

A large number of references exist on the problem of a flat-plate probe in a continuum flowing plasma. These have been reviewed by Chung, Talbot and Touryan (1974).

CHAPTER II

2. STATEMENT OF THE PROBLEM

In order to define a mathematical model for the plasma, the following assumptions have been made:

1. The plasma consists of two species of charged particles, one positive and one negative together with neutrals. Far from the probe, the net charge density approaches zero. Linear relations between current density and gradients are assumed for both species. In many experimental situations, thermal contact between species is weak enough to allow significant temperature differences to exist between them if one of them acts as an energy source or sink. Therefore, an arbitrary temperature ratio is allowed in the theoretical model. In most applications the electrons have the weakest thermal contact with other species.

2. We assume an unbounded, steady state, constant-property frozen-chemistry plasma with no magnetic field.

3. The plasma is slightly ionized, so that the mean free paths between ions or electrons and neutral particles are much smaller than the mean free path between ions and electrons.

4. The neutral flow is assumed incompressible.

5. The probe surface is assumed fully charge absorbing.

6. We assume that the Einstein relation $\mu = \frac{eD}{kT}$ between diffusion coefficient D and mobility μ is valid for all charged species, where e is magnitude of electron charge, k is Boltzmann's

constant and T is temperature.

7. We assume that Debye length $\lambda_D \gg$ probe radius $R_p \gg$ all charged particle mean free paths, so that the electric potential near the probe obeys Laplace's equation.

8. We assume that the diffusion coefficient and mobility are constant everywhere. This means that the so-called "cooling effect", (Chapkis and Baum 1971) in which the probe cools the local plasma, thereby locally changing the diffusion coefficient and mobility, is not considered in this theory.

9. The plasma is slightly ionized, so that the coupling between the charge transport problem and the neutral flow is neglected.

CHAPTER III

3. BASIC EQUATIONS AND BOUNDARY CONDITIONS

According to the above assumptions (Chap. 2), the governing equations and boundary conditions (Lam 1964) then are:

$$\underline{J}_i = N_i \underline{U} - \mu_i N_i \nabla V - D_i \nabla N_i; \quad \nabla \cdot \underline{J}_i = 0 \quad (3.1)$$

$$\underline{J}_e = N_e \underline{U} + \mu_e N_e \nabla V - D_e \nabla N_e; \quad \nabla \cdot \underline{J}_e = 0 \quad (3.2)$$

$$\nabla^2 V = 0 \quad (3.3)$$

$$\left. \begin{array}{l} R = R_p: \quad N_i = 0, \quad N_e = 0, \quad V = V_p \\ R \rightarrow \infty: \quad N_i \rightarrow N_{\infty i}, \quad N_e \rightarrow N_{\infty e}, \quad V \rightarrow 0 \end{array} \right\} \quad (3.4)$$

where N is the number density, V is the potential, R is the radius and J is the current per unit area. Subscripts i , e , p , ∞ refer to the ions, electrons, probe surface and infinite radius respectively.

The total ion or electron current I collected by the probe is given by:

$$I = \pm e \iint \underline{J} \cdot d\underline{S} \quad (3.5)$$

evaluated over the probe surface S , where the differential area vector $d\underline{S}$ is oriented outwardly. We introduce nondimensional variables as follows;

$$\begin{aligned} j &= \frac{JR_p}{N_{\infty} D}, & \Lambda &= \frac{l}{R_p}, & n &= \frac{N}{N_{\infty}} \\ Ra &= \frac{2U_{\infty} R_p}{D}, & u &= \frac{U}{U_{\infty}}, & \varphi &= \frac{eV}{kT_e} \\ \epsilon &= \frac{T}{T_e}, & \mu &= \frac{eD}{kT}, & r &= \frac{R}{R_p} \end{aligned}$$

$$\nabla = R_p \nabla$$

The governing equations and boundary conditions then reduce

to:

$$\epsilon_i \underline{j}_i = \frac{\epsilon_i Ra_i}{2} n_i \underline{u} - n_i \nabla \varphi - \epsilon_i \nabla n_i; \quad \nabla \cdot \underline{j}_i = 0 \quad (3.6)$$

$$\underline{j}_e = \frac{Ra_e}{2} n_e \underline{u} + n_e \nabla \varphi - \nabla n_e; \quad \nabla \cdot \underline{j}_e = 0 \quad (3.7)$$

$$\nabla^2 \varphi = 0 \quad (3.8)$$

$$r = 1: n_i = 0, n_e = 0, \varphi = \varphi_p$$

$$r \rightarrow \infty: n_i \rightarrow 1, n_e \rightarrow 1, \varphi \rightarrow 0 \quad (3.9)$$

Using equation (3.8) and assuming that the flow is incompressible, i.e. $\nabla \cdot \underline{u} = 0$, we obtain from equations (3.6) and (3.7).

$$\epsilon_i \frac{Ra_i}{2} \underline{u} \cdot \nabla n_i - \nabla n_i \cdot \nabla \varphi - \epsilon_i \nabla^2 n_i = 0 \quad (3.10)$$

$$\frac{Ra_e}{2} \underline{u} \cdot \nabla n_e + \nabla n_e \cdot \nabla \varphi - \nabla^2 n_e = 0 \quad (3.11)$$

From the governing equations (3.8), (3.10) and (3.11), we have an uncoupled situation for n_i and n_e . Also, equation (3.10) is similar to equation (3.11), but with φ/ϵ_i and Ra_i replaced by $-\varphi$ and Ra_e , respectively. If we solve equation (3.10) for ion density this solution can then be applied to the equation (3.11) for electron density. Equations (3.10) and (3.11) cannot be solved by analytic methods because \underline{u} in these equations is obtained from numerical results by other authors. Their solution by numerical methods is discussed in Chapter 4.

3.1 CYLINDRICAL COORDINATES

A cylindrical coordinate system (r, θ, z) with axis along the center of the cylinder is chosen with $\theta = 0$ as the downstream radius.

The fluid motion and electric potential field are assumed to be two-dimensional and hence independent of the coordinate z . The fluid motion is described by radial and transverse components of velocity (u_r, u_θ) . The velocity components are expressed in terms of a dimensionless stream function $\psi(r, \theta)$ by the equations

$$u_r = \frac{1}{r} \frac{\partial \psi}{\partial \theta}, \quad u_\theta = - \frac{\partial \psi}{\partial r} \quad (3.12)$$

Since we want a fine computational grid close to the probe surface and we also need a large outer boundary radius for computations, we transform the radial coordinate using the relation $s = \ln r$, as follows:

$$\frac{\partial}{\partial s} = r \frac{\partial}{\partial r}, \quad \frac{\partial^2}{\partial s^2} = r \frac{\partial}{\partial r} \left(r \frac{\partial}{\partial r} \right)$$

Equation (3.11) then becomes, removing subscripts:

$$\frac{Ra \exp(s)}{2} \left(u_s \frac{\partial n}{\partial s} + u_\theta \frac{\partial n}{\partial \theta} \right) - \frac{\partial n}{\partial s} \frac{\partial \varphi}{\partial s} - \frac{\partial n}{\partial \theta} \frac{\partial \varphi}{\partial \theta} - \left(\frac{\partial^2 n}{\partial s^2} + \frac{\partial^2 n}{\partial \theta^2} \right) = 0 \quad (3.13)$$

The appropriate solution of Laplace's equation (3.8) for the cylindrical case can be obtained from the solution for the equatorial plane of a prolate spheroid, approximated for radii \ll major axis (Moon and Spencer 1961 p. 240, Chang and Laframboise 1975).

For a spheroid of equatorial radius (semi-minor axis) R_p and half-length (semi-major axis) LR_p , with $L \gg 1$, this potential is:

$$\varphi = \varphi_p \left(1 - \ln r / \ln 2L \right) \quad (3.14)$$

$$\frac{d\varphi}{dr} = - \frac{\varphi_p}{\ln 2L} \frac{1}{r} \quad (3.15)$$

By inspection of (3.15), we see that we may apply a non-dimensional

scaled potential $\varphi_p / \ln 2L$ as a parameter in solving (3.13) for a cylindrical problem. This is important because it enables us to treat together all sufficiently long cylindrical probes. In using our results to interpret probe measurements, L must be related to the probe length-to-radius ratio Λ . Clearly $\Lambda \approx 2L$; the exact relation between Λ and L will depend slightly on e.g. whether the probe support is insulating or conducting. With this kept in mind, we assume $\Lambda = 2L$ in what follows.

The neutral flow solutions of Takami and Kellar (1969) and Dennis and Chang (1970) were used to provide (u_s, u_θ) in (3.13). Takami and Kellar (1969) solved the Navier-Stokes equations numerically for steady two-dimensional viscous flow of an incompressible fluid past a circular cylinder for Reynolds numbers from 1 to 60 (Fig. 3.1). Dennis and Chang (1970) have extended the work of Takami-Kellar to Reynolds numbers from 0.1 to 100 (Fig. 3.2). The numerical values of (u_s, u_θ) of Takami-Kellar and Dennis-Chang were used during the numerical solution (Ch. 4) of equation (3.13). These authors have not provided sufficient information to permit us to evaluate the effects of errors in their solutions on our results. However, for Reynolds numbers of 7, 20 and 40, neutral flow solutions from both of these papers are available (Figs: 3.1, 3.2). For $Re = 40$, we have calculated total probe current using both flow solutions. In this calculation we also used the values $Sc = 10$ and $\varphi_p = 0$. The two results agreed to within 2%, even though grids of 40×40 and 60×60 points were used respectively.

3.2 SPHERICAL COORDINATES

A spherical polar coordinate system (r, θ, ξ) with the origin at the center of the sphere is chosen with $\theta = 0$ as the downstream radius. Both the fluid motion and electric potential field are axially symmetric and hence independent of the azimuthal coordinate ξ . The fluid motion is described by radial and transverse components of velocity (u_r, u_θ) in a plane through the axis of symmetry. The velocity components are

$$u_r = \frac{1}{r^2 \sin \theta} \frac{\partial \psi}{\partial \theta}, \quad u_\theta = -\frac{1}{r \sin \theta} \frac{\partial \psi}{\partial r} \quad (3.16)$$

Equation (3.10) then becomes, after removing subscripts:

$$\epsilon \frac{Ra \exp(s)}{2} (u_s \frac{\partial n}{\partial s} + u_\theta \frac{\partial n}{\partial \theta}) - \frac{\partial n}{\partial s} \frac{\partial \varphi}{\partial s} - \frac{\partial n}{\partial \theta} \frac{\partial \varphi}{\partial \theta} - \epsilon (\frac{\partial^2 n}{\partial s^2} + \frac{\partial n}{\partial s} + \frac{\partial^2 n}{\partial \theta^2} + \cot \theta \frac{\partial n}{\partial \theta}) = 0 \quad (3.17)$$

Boundary conditions are the same as in equations (3.9).

The appropriate solution of Laplace's equation (3.8) is:

$$\varphi = \frac{\varphi_p}{r}, \quad \frac{d\varphi}{dr} = -\frac{\varphi_p}{r^2} \quad (3.18)$$

The neutral flow solutions of Dennis and Hudson (1973) were used in (3.17). Dennis and Hudson (1973) solved the Navier-Stokes equations numerically for steady flow past a sphere for Reynolds numbers from 0.1 to 60 (Fig. 3.3). The numerical values of (u_s, u_θ) of Dennis and Hudson were used during the numerical solution (Ch. 4) of equation (3.17).

CHAPTER IV

4. NUMERICAL METHODS AND CALCULATION PROCEDURE

According to Chapter 3, we need to solve the elliptic partial differential equations (3.13) and (3.17) by numerical methods.

In this chapter, we present new "upwind difference" methods (Sec. 4.1) developed for time-independent situations in order to obtain faster computation time and stability of calculations.

The local current fluxes are calculated by an extrapolation method (Sec. 4.2) and the total currents are calculated by Simpson's integration rule with Richardson's extrapolation method (McCormick and Salvadori 1964) (Sec. 4.2).

4.1 TIME INDEPENDENT UPWIND DIFFERENCE METHODS

The usual methods for numerically solving elliptic partial differential equations with variable coefficients are the Successive Over-Relaxation Method, the Alternating Direction Implicit Method and the Quasi-Linearization Method (Smith 1965). Each method involves writing $\frac{dn}{dx}$ and $\frac{d^2n}{dx^2}$ in finite-difference approximation form and solving for n approximately using the iterative method called relaxation (Smith 1965), in which the values of n at points in the computational grid are successively replaced by linear combinations of the surrounding values.

The usual finite-difference approximation of $\frac{d^2n}{dx^2}$ is

$$\frac{d^2n}{dx^2} = \frac{n_{m+1} + n_{m-1} - 2n_m}{\Delta x^2} + O(\Delta x^2) \quad (4.1)$$

The usual expressions for the difference $\frac{dn}{dx}$ are as follows.

- (i) forward difference: leads always to stable solutions

$$\frac{dn}{dx} = \frac{n_{m+1} - n_m}{\Delta x} + O(\Delta x) \quad (4.2)$$

- (ii) backward difference: always leads to stable solutions

$$\frac{dn}{dx} = \frac{n_m - n_{m-1}}{\Delta x} + O(\Delta x) \quad (4.3)$$

- (iii) centered difference: leads to a solution stable only for small enough Δx (Fukuda 1969)

$$\frac{dn}{dx} = \frac{n_{m+1} - n_{m-1}}{2\Delta x} + O(\Delta x^2) \quad (4.4)$$

where $\Delta x = x_m - x_{m-1} = x_{m+1} - x_m$

The usual way for solving elliptic partial differential equations uses centered differences, because the accuracy is higher than for the other two methods. However, numerical instabilities occur in this centered difference method because of round off error and the "hereditary error" (Fukuda 1969) for large Δx . The backward and forward difference methods always lead to a stable solution for any Δx (Fukuda 1969).

We suppose that the (s, θ) space is divided into a grid of $L \times M$ points separated by distance increments h . Then we can write the coordinate distances as $s = \ell h$ and $\theta = mh$ where $m = 0, 1, 2, \dots, M$ and $\ell = 0, 1, 2, \dots, L$. Thus any point on the grid is uniquely identified by the indices (ℓ, m) . A portion of such a grid space is shown in Fig. 4.1.

Next we write the partial differential equation in finite-difference form. We now consider the problem of solving the equation for $n_{\ell, m}$. The substitution procedure for $n_{\ell, m}$ is determined by substituting the chosen difference expressions into the given equation and solving the result for $n_{\ell, m}$ in terms of the surrounding values. Relaxation schemes may be divided

into two classes: (1) simultaneous relaxation, and (2) successive relaxation.

Since relaxation is an iterative procedure, some method is needed to identify the order of approximation. We thus label n with the superscript K to indicate the K th guess n^K . If the method is convergent, n^K should approach the true solution n at all points as $K \rightarrow \infty$. In the simultaneous relaxation, the $(K+1)$ th guess can then be computed according to (Smith 1965) $n_{l,m}^{K+1} = n_{l,m}^K + \alpha R_{l,m}^K$, where $R_{l,m}^K$ is the residual, which is equal to the difference between the result for $n_{l,m}$ in terms of surrounding values, and the previous value $n_{l,m}^K$, and α is a constant which depends on the finite-difference form and the constants in the differential equation. Then in the simultaneous relaxation, the entire new field $n_{l,m}^{K+1}$ is calculated using residuals computed from the old field.

However, it is clear that once a new guess has been made at a given point, the new values can be used to modify the residuals at the surrounding points. Thus, the residuals can be computed sequentially starting from grid point (1,1) and working to the right along the grid to point (L-1,1), then skipping to the second interior row of points and working from point (1,2), to (L-1, 2), etc., as shown in fig. 4.1. This scheme is called successive relaxation. In this case the residual at (l,m) is computed using two old guesses and two new guesses at surrounding points $(l+1,m)$, $(l-1,m)$, $(l, m+1)$ and $(l,m-1)$ as shown in fig. 4.1. In this method, the error decreases twice as fast as in the case of simultaneous

relaxation (Smith 1965).

Upwind difference methods were introduced by Leith (1965) for solving time dependent differential equations. The results show that the solutions are well stabilized during the calculations. We have developed upwind methods for our governing equations with convection term for the time-independent case, in order to obtain faster computation time and stability of calculations. In the partial differential equation as follows

$$\frac{Ra}{2} \underline{u} \cdot \nabla n + \nabla n \cdot \nabla \varphi - \nabla^2 n = 0 \quad (4.5)$$

calculation instabilities occur when Ra is relatively large in all centered difference methods. This is believed to be caused by loss of diagonal dominance (Greenspan 1975, p. 218).

In our equation (4.5), \underline{u} sometimes contains a wake (region of recirculation) behind the probe (Figs. 3.1-3.3), and this might also be an important source of instability in calculations by other authors.

The idea of upwind difference methods is based on the observation that in a convective situation, physical information is transported from the upwind direction, so that some combination of numerically stable forward differences may give the most useful approximation of the $(\underline{u} \cdot \nabla n)$ term. Also, we shall see that the methods are very easy to apply to the successive relaxation procedure.

4.1.1 LOWER ORDER METHOD

The grid structure of the method is shown in figure 4.2 with the local wind vector \underline{u} at the central point (l,m) . Here we use rectangular coordinates x and y . In figure 4.2, the wind direction has been chosen such that $u_x > 0$ and $u_y > 0$. The $(\underline{u} \cdot \nabla n)$ term in (4.5) can be approximated by either of the following backward difference expressions:

$$\underline{u} \cdot \nabla n = \frac{u_x}{\Delta x} (n_{l,m} - n_{l-1,m}) + \frac{u_y}{\Delta y} (n_{l,m} - n_{l,m-1}) = \beta_1 \quad (4.6a)$$

or

$$\underline{u} \cdot \nabla n = \frac{u_x}{\Delta x} (n_{l,m-1} - n_{l-1,m-1}) + \frac{u_y}{\Delta y} (n_{l-1,m} - n_{l-1,m-1}) = \beta_2 \quad (4.6b)$$

We first consider the purely convective situation in which no diffusion or potential gradients exist, and (4.5) reduces to $\underline{u} \cdot \nabla n = 0$. We wish the information to be transported only from the upwind direction, so we require that our substitution process have the following properties:

$$\text{If } u_x = u_y \quad \text{then} \quad n_{l,m} = n_{l-1,m-1} .$$

$$\text{If } u_x = 0 \quad \text{then} \quad n_{l,m} = n_{l,m-1} . \quad (4.7)$$

$$\text{If } u_y = 0 \quad \text{then} \quad n_{l,m} = n_{l-1,m} .$$

The following linear combinations of (4.6a) with (4.6b) have these properties.

$$\text{If } u_x > u_y \quad \text{then} \quad \underline{u} \cdot \nabla n = \frac{\beta_1 \frac{u_x}{\Delta x} + \beta_2 \frac{u_y}{\Delta y}}{u_x/\Delta x + u_y/\Delta y} \quad (4.8)$$

$$\text{If } u_x < u_y \text{ then } \underline{u} \cdot \nabla n = \frac{\beta_1 \frac{u_y}{\Delta y} + \beta_2 \frac{u_x}{\Delta y}}{u_x/\Delta x + u_y/\Delta y} \quad (4.9)$$

The fact that (4.8) and (4.9) satisfy the conditions (4.7) can be readily verified by assuming $\underline{u} \cdot \nabla n = 0$, substituting (4.8) and (4.9) into this relation, and solving for $n_{l,m}$.

These relations also have another important feature, which we can see as follows.

We define $q = \left| \frac{u_y \Delta x}{u_x \Delta y} \right|$, and we then obtain: (i) if $u_x > u_y$ ($q < 1$)

$$\text{then } \underline{u} \cdot \nabla n = \frac{|u_x|}{\Delta x} [n_{l,m} + (q-1)n_{l-1,m} - qn_{l-1,m-1}] \quad (4.10)$$

(ii) If $u_x < u_y$ ($q > 1$)

$$\text{then } \underline{u} \cdot \nabla n = \frac{|u_x|}{\Delta x} [qn_{l,m} - (q-1)n_{l,m-1} - n_{l-1,m-1}] \quad (4.11)$$

If we again assume $\underline{u} \cdot \nabla n = 0$ and equations (4.10) and (4.11) for $n_{l,m}$ we obtain if $q < 1$,

$$\text{then } n_{l,m} = (1-q) n_{l-1,m} + qn_{l-1,m-1} \quad (4.10')$$

if $q > 1$,

$$\text{then } n_{l,m} = \left(1 - \frac{1}{q}\right) n_{l,m-1} + \frac{1}{q} n_{l-1,m-1} \quad (4.11')$$

i.e. if $q > 1$, $n_{l,m}$ becomes just the value of n at the upstream point A in figure 4.2, as determined by linear interpolation between the values $n_{l-1,m-1}$ and $n_{l,m-1}$. If $q < 1$, $n_{l,m}$ then becomes the value at the corresponding upstream point on the left-hand vertical boundary between $(l-1, m-1)$ and $(l-1, m)$.

Similar relations can be obtained easily for the other three cases; (a) if $u_x < 0$, $u_y < 0$, we replace $n_{l-1,m}$, $n_{l-1,m-1}$, and $n_{l,m-1}$ by $n_{l+1,m}$, $n_{l+1,m+1}$ and $n_{l,m+1}$, respectively, (b) if $u_x > 0$, $u_y < 0$ we replace these values by $n_{l-1,m}$, $n_{l-1,m+1}$ and $n_{l,m+1}$, respectively (c) if $u_x < 0$, $u_y > 0$, we replace these same values by $n_{l+1,m}$, $n_{l+1,m-1}$ and $n_{l,m-1}$, respectively. We therefore have an algorithm which is always in accord with the essential physics of our situation, i.e. in the purely convective limit it causes information always to be transferred in the downstream direction along streamlines. A similar method by Carlson (1967 p. 240) exists for problems involving time and one space variable.

4.1.2 HIGHER ORDER METHOD

The interpretation of (4.10') and (4.11') in terms of linear interpolations suggests that a more accurate method can be obtained by simply replacing these interpolations by higher-order ones, involving more than two collinear points (figs. 4.2, 4.3). For the sake of illustration, we consider this time the case when $u_x < 0$, $u_y < 0$ and $q > 1$. We first fit the density values $n_{l-1, m+1}$, $n_{l, m+1}$ and $n_{l+1, m+1}$ with a parabola as follows.

$$n = n_{l, m+1} + A_1 \xi + A_2 \xi^2, \quad \text{where } \xi = (x - x_l) / \Delta x.$$

We then have:

$$n_{l-1, m+1} = n_{l, m+1} - A_1 + A_2$$

and:

$$n_{l+1, m+1} = n_{l, m+1} + A_1 + A_2$$

(4.12)

Solving, we obtain:

$$A_1 = \frac{n_{l+1, m+1} - n_{l-1, m+1}}{2}$$

$$A_2 = \frac{n_{l-1, m+1} + n_{l+1, m+1} - 2n_{l, m+1}}{2}$$

(4.13)

$$\text{and } n_{kl} = n_{l, m+1} + A_1 q' + A_2 q'^2, \quad \text{where } q' = 1/q$$

Next, we fit $n_{l, m+1}$, $n_{l+1, m+1}$ and $n_{l+2, m+1}$ with another parabola.

Similarly, we obtain

$$\left. \begin{aligned} n_{k2} &= n_{l+1,m+1} + A_1'(q'-1) + A_2'(q'-1)^2 \\ A_1' &= \frac{n_{l+2,m+1} - n_{l,m+1}}{2} \\ A_2' &= \frac{n_{l+2,m+1} + n_{l,m+1} - 2n_{l+1,m+1}}{2} \end{aligned} \right\} \quad (4.14)$$

Again when $\underline{u} \cdot \nabla n = 0$, we recover, as we should, the following:

if $q' = 0$ then $n_{k1} = n_{l,m+1}$ and $n_{k2} = n_{l,m+1}$,

if $q' = 1$ then $n_{k1} = n_{l+1,m+1}$ and $n_{k2} = n_{l+1,m+1}$.

The best way of also satisfying the conditions corresponding to (4.10') and (4.11') is:

$$n_{l,m} = n_{k2} + (n_{k1} - n_{k2})(1 - q') \quad (4.15)$$

Therefore, we obtain

$$\begin{aligned} n_{l,m} &= \frac{(q'-1)}{2} [n_{l,m+1}(3q'^2 - 2q' - 2) + n_{l-1,m+1}(1 - q')q' \\ &\quad + n_{l+2,m+1}q'^2] + \frac{q'}{2} [n_{l+1,m+1}(1 - 3q'^2 + 4q')] \end{aligned} \quad (4.16a)$$

and $\underline{u} \cdot \nabla n = \frac{|u_y|}{\Delta y} (n_{l,m} - \beta_3)$ where β_3 is the right hand side of (4.16a).

For $q < 1$, from the same mathematical process, we obtain

$$\begin{aligned} n_{l,m} &= \frac{(q-1)}{2} [n_{l+1,m}(3q^2 - 2q - 2) + n_{l+1,m-1}(1-q)q \\ &\quad + n_{l+1,m+2}q^2] + \frac{q}{2} [n_{l+1,m+1}(1 - 3q^2 + 4q)] \end{aligned} \quad (4.16b)$$

and $\underline{u} \cdot \nabla n = \frac{|u_x|}{\Delta x} (n_{l,m} - \beta_4)$ where β_4 is the right hand side of (4.16b).

In special cases where $n_{l,m}$ is near an edge or a corner, so that the point $(l+2,m+1)$ or $(l+1,m+2)$ is outside our domain,

we use $n_{l,m} = n_{k1}$ instead of equation (4.16a) or (4.16b).

Similar relations can be obtained easily for the other three cases: (a) $u_x > 0, u_y > 0$ (b) $u_x < 0, u_y > 0$ and (c) $u_x > 0, u_y < 0$.

Therefore, the numerical method in our case is to express the $\nabla^2 n, \nabla\phi \cdot \nabla n$ terms by central differences and $\underline{u} \cdot \nabla n$ by the higher order upwind difference form and to use successive relaxation to solve the charge transport equation (3.13) or (3.17) for n (we call this method "upwind difference method" in later chapters). In applying these methods to (3.13) and (3.17), x and y are replaced by θ and s , respectively, and u_x and u_y are replaced by u_θ and u_s , respectively.

4.1.3 ACCURACY OF NUMERICAL METHOD

In order to estimate the accuracy in our numerical methods, we numerically solved two problems which have known analytic solutions. These problems involve the usual convection-diffusion equation:

$$\frac{UR_p}{D} \frac{\partial n}{\partial x} - \left(\frac{\partial^2 n}{\partial x^2} + \frac{\partial^2 n}{\partial y^2} + \frac{\partial^2 n}{\partial z^2} \right) = 0 \quad (4.17)$$

where we have assumed uniform flow in the x direction. An analytic solution of (4.17) (Dennis et al 1973) for spherical coordinates is

$$n = 1 + \frac{C_1}{r} \exp\left[\frac{Ra}{2} \frac{r}{r} (\cos \theta - 1) \right] \quad (4.18)$$

where $Ra = UR_p / D$, $r = \sqrt{x^2 + y^2 + z^2}$ and $n \rightarrow 1$ when $r \rightarrow \infty$ (point source in uniform flow). An analytic solution for cylindrical coordinates is (Dennis et al 1968).

$$n = 1 + C_2 \exp\left[\frac{Ra}{2} \frac{r}{r} \cos \theta \right] K_0\left(\frac{Ra}{2} \frac{r}{r} \right) \quad (4.19)$$

where $K_0(w)$ is the modified Bessel function of zero order, and $r = \sqrt{x^2 + y^2}$ (line source in uniform flow). For example in cylindrical coordinates, if we solve equation (4.17) numerically with boundary conditions obtained using numerical values of equation (4.19), we can obtain the relative error in our numerical methods. We solve (4.18) and (4.19) numerically in the domain ($r_a < r < r_b$, $0 < \theta < \pi$).

Now the boundary conditions from (4.19) are:

$$r = r_a: n_{l,m} = 1 + 2 \exp \left[\frac{Ra r_a}{2} \cos \theta_m \right] K_0 \left(\frac{Ra r_a}{2} \right)$$

$$r = r_b: n_{b,m} = 1 + 2 \exp \left[\frac{Ra r_b}{2} \cos \theta_m \right] K_0 \left(\frac{Ra r_b}{2} \right)$$

with similar boundary conditions from (4.18). In either case we also have:

$$\theta = 0, \theta = 180^\circ: \frac{\partial n}{\partial \theta} = 0$$

where we choose $C_a = 2$, $Ra = 10$, $r_a = 1$, $r_b = 25$ to define our two test problems. With this choice the variation in each solution over the chosen domain is of the same order as the solution itself. The values which the analytic solutions then have at $r = 1$, $\theta = 0^\circ$ and 180° are 2.181 and 1.0 respectively for the cylinder, 3 and 10, respectively for the sphere.

The uniform flow in the (r, θ) coordinates is $u_\theta = -\sin \theta_m$,
 $u_r = \cos \theta_m$.

We again transform the radial coordinate using the relation $s = \ln r$. In figure 4.4, we show the relative error between analytic solutions and numerical solutions for a) cylindrical coordinates b) spherical coordinates, for $\Delta\theta = \Delta s = \pi/30$. From figure 4.4, we find the maximum error at $\theta = 0^\circ$ and $\theta = 40^\circ - 50^\circ$. We also find that the error at the determination of local current fluxes to the inner boundary $r = 1$ is smaller than 0.1% in both spherical and cylindrical cases. The reason for the larger errors downstream than upstream is the larger density gradients in these

analytical solutions downstream. The maximum relative error of both spherical and cylindrical cases is shown as a function of $\Delta\theta$ in figure 4.5 (where $\Delta\theta = \Delta s$ for each calculation, $\Delta\theta = \theta_l - \theta_{l-1}$ and $\Delta s = \ln r_m - \ln r_{m-1}$). From the slopes of the lines in figure 4.5, we have obtained graphical estimates of the actual order of the methods. For the sphere, we obtained $O(\Delta\theta^{1.06})$ for the lower order method and $O(\Delta\theta^{1.48})$ for the higher order method. For the cylinder we obtain $O(\Delta\theta^{1.22})$ for the lower order method and $O(\Delta\theta^{1.57})$ for the higher order method. For the lower order method, we can say the order of the method is slightly better than 1, but for the higher order method the order of the method is about 1.5. The computation time on the CDC 6600 computer by our numerical methods is shown as a function of the number of grid points in figure 4.6. The computation time at 30×30 grid points is less than 200 sec and 140 sec by our numerical method with the upwind higher order difference and the lower order difference, respectively. Iterative times for the sphere and the cylinder were approximately 1.6 iterations/sec and 3.1 iterations/sec using the higher-order method, and the iteration was stopped in the condition $\sum |n_{l,m}^{K+1} - n_{l,m}^K| \leq 10^{-4}$.

4.2 NUMERICAL INTEGRATION AND DIFFERENCE METHODS

4.2.1 LOCAL CURRENT DENSITY

The local current density from equations (3.6) and (3.7) is defined as

$$j = \left. \frac{dn}{dr} \right|_{r=1} = \left. \frac{dn}{ds} \frac{ds}{dr} \right|_{s=0} = \left. \frac{dn}{ds} \right|_{s=0} \quad (4.20)$$

In order to obtain a second order difference approximation for equation (4.20) we fit $n_{1,m}$, $n_{2,m}$, and $n_{3,m}$ using a parabola as follows

$$n = A_3 s^2 + A_4 s + A_5$$

$$n_{1,m} = A_5 = 0 \text{ from boundary condition, at probe surface (Eq. 3.4)}$$

$$n_{2,m} = A_3 (\Delta s)^2 + A_4 (\Delta s)$$

$$n_{3,m} = 4A_3 (\Delta s)^2 + 2A_4 (\Delta s)$$

$$\therefore \frac{dn}{ds} = A_4 + 2A_3 s$$

$$\therefore j = \left. \frac{dn}{ds} \right|_{s=0} = A_4 + 0(\Delta s^2) = \frac{4n_{2,m} - n_{3,m}}{2\Delta s} + 0(\Delta s^2) \quad (4.21)$$

Similarly, we fit a parabola through $n_{1,m}$, $n_{3,m}$ and $n_{5,m}$ to obtain immediately

$$j = \left. \frac{dn}{ds} \right|_{s=0} = \frac{4n_{3,m} - n_{5,m}}{4\Delta s} + 0[(2\Delta s)^2] \quad (4.22)$$

Equations (4.21) and (4.22) have an error of $0(\Delta s^2)$ and $0[(2\Delta s)^2]$, respectively. Therefore we may use the Richardson extrapolation method (McCormick and Salvadori 1964) to obtain a more accurate value of the local current density. If j_1 and j_2 are the two

approximate expressions for j given in (4.21) and (4.22), respectively, then the Richardson extrapolation method yields, to second order:

$$j = (4j_1 - j_2)/3 = \frac{32n_{2,m} - 12n_{3,m} + n_{5,m}}{12\Delta s} \quad (4.23)$$

4.2.2 TOTAL CURRENT

The total current for the sphere and current per unit length for the cylinder are from Chapter 3, Eq. (3.5) as follows:

$$i = \frac{1}{2} \int_0^{\pi} j(\theta) \sin \theta \, d\theta \quad (\text{sphere}) \quad (4.24)$$

$$i = \frac{1}{2\pi} \int_0^{2\pi} j(\theta) \, d\theta \quad (\text{cylinder})$$

In order to obtain the most accurate possible value of i , we used integration by Simpson's rule with intervals $\Delta\theta$ and $2\Delta\theta$. We then carried out Richardson extrapolation on the results obtained in this way (McCormick and Salvadori, 1964).

4.3 CALCULATION PROCEDURE

The block diagram of a calculation is shown in Fig. 4.7.

The charge transport equations (3.13) and (3.17) are solved using the upwind difference methods which we have developed in Sec. 4.1.

Boundary conditions are from Eqs. (3.9), (4.18) and (4.19) as follows:

$$s = 0: \quad n_{1,m} = 0 \quad (\text{from kinetic theory, Lam 1964})$$

$$\theta = 0^\circ \text{ and } 180^\circ: \quad \frac{\partial n}{\partial \theta} = 0 \quad (\text{from symmetry})$$

$$s = s_b = \ln r_b :$$

$$n_{l,m} = 1 - (1 - n_{l-1,m}) \left(\frac{r_{l-1}}{r_l} \right)^{\frac{1}{2}} \exp \left[-\frac{Ra}{2} (r_l - r_{l-1}) (1 - \cos \theta_m) \right] \\ (\text{cylinder})$$

$$n_{l,m} = 1 - (1 - n_{l-1,m}) \left(\frac{r_{l-1}}{r_l} \right) \exp \left[-\frac{Ra}{2} (r_l - r_{l-1}) (1 - \cos \theta_m) \right] (\text{sphere})$$

where we have used Eq. (4.19) with the approximation:

$$K_0(x) \simeq \left(\frac{\pi}{2x} \right)^{\frac{1}{2}} \exp(-x) \text{ for large } x \text{ (Dennis et al 1968).}$$

The boundary conditions at $s = s_b$ are from (4.18) and (4.19), which we assume to give the ratio of the two values $n_{l-1,m}$ and $n_{l,m}$ (Dennis et al 1968, 1973). This procedure is based on the fact that at large radii, the disturbance in number density due to the probe can be expected to approach that of a sink (negative source) in a uniform flow. These boundary conditions are solved together with the charge transport equation for each iteration in our calculations.

The iterative calculation was continued until sufficient

convergence was attained. This decision was made by requiring

$$\sum |n_{l,m}^{K+1} - n_{l,m}^K| \leq 10^{-3}.$$

In order to achieve the fastest possible convergence the successive relaxation was done in a generally upstream to downstream order during each iteration. The calculation procedure for local currents and total currents was checked by trying several values of the grid intervals $\Delta\theta$ and Δs , and several positions of the outer boundary r_b . The values of $\Delta\theta$, Δs and r_b which we used for calculation of densities, local currents and total currents are shown in Table I. One more check of the calculation procedure involves the limit in which Ra ($=Sc \times Re$) is small. In this condition, the numerical values of total currents and local currents are in good agreement with the analytical values from the stationary (no-flow) theory (Appendix B). Each total and local current collection result has been computed to a relative accuracy of 2% and 5% or better, respectively, in an average time of approximately 20 minutes on the CDC 6600. In the spherical case the calculations yielded a relative accuracy of 0.4% or better in comparison to the analytical solution at stationary conditions. In flowing conditions these accuracies refer only to the solution of the charge transport equation, and not to the accuracy of the numerical Navier-Stokes solutions used as input to the calculations. The accuracy of the latter has been discussed in Sec. 6.3. In the cylindrical case the results cannot be compared with the stationary (no-flow) limit for reasons discussed in Appendix B.

CHAPTER V

5. RESULTS AND DISCUSSIONS FOR CYLINDER IN CROSS-FLOW

5.1 CHARGE DENSITY PROFILES

Numerical results for charge density contours are shown in Fig. 5.1 using the solutions of Eqs. (3.12) to (3.15). The effect of the neutral wake (recirculation region, Figs. 3.1, 3.2) is shown in Fig. 5.1a for a cylinder at space potential with charged-particle Schmidt number $Sc_c = 10^2$. The neutral wake for the cylinder in cross flow occurs for $Re \geq 7$ (Takami et al 1969). Figure 5.1a shows that for a flow with wake ($Re = 20$), the charge density is larger in the rear stagnation region than in the case of flow without a wake ($Re = 0.4$ in Figure 5.1a). The reason is that in the case with wake, the recirculation of the neutral flow brings charge to the rear stagnation region.

The effect of charged particle Schmidt number is shown in Fig. 5.1b for Reynolds number 40. We see that the effect of the wake in the rear stagnation region increases as the Schmidt number increases. The effects of surface potential on flow with wake and flow without wake are shown in Fig. 5.1c ($Re = 40, Sc_c = 1$) and 5.1d ($Re = 0.4, Sc_c = 10^2$) for both attracting potential ($\varphi_p / \epsilon \ln \Lambda = 4$) and retarding potential ($\varphi_p / \epsilon \ln \Lambda = -4$). For the attracting potential, the effect of the potential tends to symmetrize the charge density profile around the body for both flow with wake and flow without wake.

If we only have two species (ions and electrons) in a plasma, we can numerically subtract density profiles between ions and electrons. We may thereby find the net charge density profile ($n_i - n_e$) for a cylindrical probe.

Usually the diffusion Reynolds number for ions is much larger than that for electrons. Therefore, we can numerically subtract density profiles between two different values of Ra for the same Reynolds number. The general appearance of some typical net charge density profiles is shown in Fig. (5.2): (a) for a stationary case (b) for flow without wake, (c) and (d) for flow with wake. Figure (5.2) shows that in the presence of flow, the net charge density profiles can include several regions of alternating sign downstream of the body. In the case when a wake is present, these net charge density profiles show more complicated dependence on the Reynolds number and the ion or electron Schmidt number. This phenomenon may be a very important problem in interactions between an antenna, electrostatic probe or mass spectrometer and a balloon or planetary probe. The measured plasma parameters can be affected by these several regions of alternating sign of the net charged particle density downstream of the balloon or planetary probe.

5.2 LOCAL CURRENT DENSITY

Numerical results for ion or electron local current density j at the probe surface are shown as functions of angle θ , where we define $\theta = 0$ at the rear stagnation point, in Fig. 5.3 for various surface potentials, (a) and (b) for $Re = 0.1$, $Sc_c = 10^3$ and 10^4 respectively, (c) for $Re = 1$, $Sc_c = 10^3$, (d) and (e) for $Re = 10$, $Sc_c = 10$ and 10^2 respectively, (f) for $Re = 40$, $Sc_c = 10$, (g) and (h) for $Re = 100$, $Sc_c = 0.1$ and 10 respectively. Figure 5.3 shows that for flows without a wake (Fig. 5.3(a) - (c)), the effect of the attracting surface potential is to symmetrize the local current collection and of the retarding surface potential is to unsymmetrize it. For flows with a wake (Fig. 5.3(d) - (h)), we observe large current collections at the rear stagnation region. The effect of the attracting surface potential in these cases is to symmetrize the current collection at large potentials, and also to increase the asymmetry of the collection at small potentials.

Figure 5.4 shows the influence of the Reynolds number on the local current angle dependence for $Sc_c = 1$, $\varphi_p / \epsilon \ln \Lambda = 0$ (a), 4 (b), -2 (c) and for $Sc_c = 10^2$, $\varphi_p / \epsilon \ln \Lambda = 0$ (d), 4 (e), -2 (f). Figures 5.4 (a) - (f) show more clearly the effect of the wake on the local current collection. As noted earlier (Sec. 3) a wake exists for the cylinder when $Re \geq 7$. We find that the minimum point of the local current is always close to the flow separation point and this minimum point is not moved appreciably when probe

potential is changed.

The local currents are shown as functions of the angle in Fig. 5.5 for various charged particle Schmidt numbers, for $Re = 0.4$ (a) $\varphi_p / \epsilon \ln \Lambda = 0$, (b) 4, (c) -2, and for $Re = 20$, (d) $\varphi_p / \epsilon \ln \Lambda = 0$, (e) 4 and (f) -2. Figure 5.5 shows that the effect of the charged-particle Schmidt number on the local current is larger in the front stagnation region than in the rear stagnation region.

The above numerical values of the local current density can be used to estimate ion collection by a mass spectrometer orifice electrode located in a blunt surface under continuum conditions, for instance in rocket or balloon measurements up to the D-region, in flames or in flowing afterglows (Parker 1974, Chang 1975).

5.3 TOTAL PROBE CURRENT

The numerical results for the ion or electron currents per unit length are shown as functions of the charged particle Schmidt number in Fig. 5.6 for various scaled surface potentials $\varphi_p/\epsilon \ln \Lambda$ at Reynolds number $Re = 40$. Figure 5.6 shows that for retarding potentials ($\varphi_p/\epsilon \ln \Lambda < 0$), the effect of charged particle Schmidt number increases with the potential. For large enough attracting potentials, the currents become only slightly affected by the charged particle Schmidt number.

Figure 5.7 shows the ion or electron currents per unit length for various scaled probe potentials at $Sc_c = 100$. Figure 5.7 shows that the effect of the flow increases with retarding surface potentials and decreases with increasing attracting surface potential. Also, in these two figures there is a slight decrease of current as either Re or Sc_c increases, for larger values of attracting surface potentials ($\varphi_p/\epsilon \ln \Lambda \geq 6$ in both Figs. 5.6 and 5.7).

Figure 5.8 shows logarithmic current-potential characteristics for various charged particle Schmidt numbers for (a) $Re = 2$, (b) $Re = 7$, (c) $Re = 10$, (d) $Re = 20$ and (e) $Re = 100$. Figure 5.9 shows similar characteristics for various Re at $Sc_c = 10^3$. In comparison with the usual exponential dependence from stationary collisionless probe theory (Mott-Smith and Langmuir,

1926; not shown), we see that misuse of the usual retarding potential method for the temperature determination would lead to increasing T_e overestimates as the flow effects increase (See also Sec.6.3). Also we observe that the effect of the flow is to smooth the "knee" of the probe characteristics and to render more imprecise the determination of the space potential.

Logarithmic current-potential characteristics are shown in Fig. 5.10 for various Reynolds numbers at a diffusion Reynolds number of 10^3 . Figure 5.10 shows that the model developed by Lam (1964) (Sec. 1.1) cannot be applied to a low density plasma ($\lambda_D \gg R_p$), for the currents have a large dependence on Re even if Ra is constant. The previous work (Hoult 1965) which extended Lam's model to the low density plasma case should be reconsidered.

Figures 5.11 and 5.12 show currents vs probe potential for various charged particle Schmidt numbers at Reynolds number 0.4, and for various Re at $Sc_c = 10$ respectively. At a large enough attracting potential, Figs. 5.11 and 5.12 show that the linear dependence $I \propto \phi_p$ from stationary theory (Appendix B) is recovered. This point is important for the determination of the electron or ion temperature (Appendix B).

Nondimensional current at space potential is shown as

a function of the Reynolds number in Fig. 5.13 for various charged particle Schmidt numbers, and as a function of the charged particle Schmidt number in Fig. 5.14 for various Reynolds numbers. Figures 5.13 and 5.14 show that the effects of flow on nondimensional current at space potential increase rapidly as Re and Sc_c increase.

Computed values of probe current are presented in tabular form in Table II. As we discussed in Chap. 3, the above solutions for total current, local current density and density contour maps can be applied to both ions and electrons, but with $\varphi_p / \epsilon_i \ln \Lambda$ and Ra_i for ions replaced by $-\varphi_p / \ln \Lambda$ and Ra_e , respectively, for electrons.

5.4 APPLICATION TO PRESENCE OF MAGNETIC FIELD

An important application of the present results is to a cylindrical probe with its axis parallel to an imposed magnetic field (Fig. 5.15). We can use unchanged the results described in this chapter except that D_i and D_e are replaced by $D_{i\perp}$ and $D_{e\perp}$, respectively, where we again assume that the neutral flow is not affected by the magnetic field, i.e. we have a slightly ionized plasma, and D_{\perp} is the diffusion coefficient perpendicular to the magnetic field, $D_{\perp} = D/[1+(\omega_B \tau_B)^2]$, (Bohm et al, 1949). Here $\omega_B = eB/m$ is the cyclotron angular frequency, and τ_B is the mean time between collisions with neutrals. The usual Reynolds number is then replaced by a magneto-diffusion Reynolds number which is defined as:

$$Ra_{\text{mag}} = \frac{2U R}{D_{\perp}} = Re Sc/[1+(\omega_B \tau_B)^2]$$

CHAPTER VI

6. RESULTS AND DISCUSSION FOR SPHERE

6.1 CHARGE DENSITY PROFILES

Numerical results for charge density contours are shown in Fig. 6.1 for charged particle Schmidt numbers of 0, 1, and 10 at $Re = 5$, where the solution for $Sc_c = 0$ is just the diffusion profile $n = 1 - 1/r$. Figure 6.1 shows that the charge density around the sphere becomes unsymmetrical when the charged particle Schmidt number increases. The effect of a wake on the charge density distribution is shown in Fig. 6.2. Figure 6.2 shows that for the flow with wake ($Re = 40$), the same phenomenon as in the case of cylinder in cross-flow (Fig. 5.1) occurs in the rear stagnation region. In both cases this concentration of charge behind the body occurs at larger values of Sc_c .

Effects of surface potential on charge density profiles are shown in Fig. 6.3 at $Re = 5$, $Sc_c = 1$ for the surface potentials $\phi_p/\epsilon = -4, 0, \text{ and } 4$. Figure 6.3 shows that the effect of an attracting potential is to symmetrize the charge density profile around the body. For retarding potentials, the effect of the potential is to unsymmetrize the charge density profile. Figure 6.4 shows density-angle dependence for two different distances from the probe surface, (a) $r = 4.22$ (b) $r = 1.1275$, at $Re = 5$, $Sc_c = 1$. From Fig. 6.4, we see again that the effect of surface potential changes is to symmetrize or desymmetrize the charge density profiles around the body.

6.2 LOCAL CURRENT DENSITY

Numerical results for the ion or electron local current density at the probe surface are shown as a function of the angle θ in Fig. 6.5 for various surface potentials, (a) for $Re = 20$, $Sc_c = 1$ (b) for $Re = 60$, $Sc_c = 1$. Figure 6.5a shows that for flow without a wake, the effect of the attracting surface potential is to symmetrize the current collection and the effect of the retarding surface potential is to unsymmetrize the current. The corresponding diagrams for the cylinder are Figs 5.3(a) - (d). For the flow with wake (Fig. 6.5b), we observe a wake collection effect in the rear stagnation region as in the case of the cylinder in cross-flow (Fig. 5.3(e) - (h)). The effect of attracting surface potential (Fig. 6.5) in the wake is not to symmetrize the current collection, but to increase the asymmetry of the collection as in the case of the cylinder in cross-flow (Fig. 5.3). Figure 6.6 shows the influence of the Reynolds number on the local current angle dependence for (a) $\phi_p/\epsilon = 0$, (b) 2 and (c) -4 at $Sc_c = 10^2$. In Fig. 6.6, we show the stationary solution (Eq. B1) together with the solutions for nonzero Reynolds numbers. Figure 6.6 shows that in the front stagnation region, the local currents are larger than the stationary value. In the rear stagnation region, the local current is smaller than the stationary value in the flow without wake and sometimes is larger in flow with wake.

The local currents are shown as functions of the angle in Fig.6.7 for various charged particle Schmidt numbers at $Re = 40$, for (a)

$\varphi_p/\epsilon = 0$, (b) $\varphi_p/\epsilon = 2$ and (c) $\varphi_p/\epsilon = -2$. Figure 6.7 shows that the wake effects increase with the charged particle Schmidt number.

6.3 TOTAL PROBE CURRENT

Numerical results for the ion or electron currents are shown as functions of the charged particle Schmidt number in Fig. 6.8 for various surface potentials φ_p/ϵ at the Reynolds number $Re = 5$. Figure 6.8 shows that for retarding potentials ($\varphi_p/\epsilon < 0$), the effect of the charged particle Schmidt number increases with the potential. For attracting potentials, the currents become less affected by charged particle Schmidt number.

Figure 6.9 shows ion or electron currents for various probe potentials at $Sc_c = 100$. Figure 6.9 shows that the effects of the flow increase with retarding surface potentials and decrease with increasing attracting surface potential.

Figure 6.10 shows logarithmic current-potential characteristics for various charged particle Schmidt numbers at $Re = 60$. Figure 6.11 shows similar characteristics for various Re at $Sc_c = 10$. The result for $Sc_c = 0$ is the analytic solution from the stationary (no-flow) theory (Eq. B.1). The dotted lines in Figs. 6.10 and 6.11 represent the usual exponential characteristic from the stationary collisionless probe theory (Mott-Smith and Langmuir, 1926). Comparison of our continuum results with this stationary collisionless curve shows that the usual retarding potential method for temperature determination will lead to an

increasing T_e overestimate as flow effects increase. Again, we also observe that the effect of the flow is to smooth the "knee" of the probe characteristics and to render more imprecise the determination of the space potential.

Figure 6.12 shows the diffusion Reynolds number dependence of the total current for various surface potentials at $Re = 0.5$. From the figure, we can obtain an idea of the limitations of the stationary probe theory. For example, for diffusion Reynolds numbers above about 0.5 at space potential, we need to use these numerical results instead of the stationary theory.

Nondimensional current at space potential is shown as a function of Reynolds number in Figure 6.13 for various charged particle Schmidt numbers, and as a function of the charged particle Schmidt number in Fig. 6.14 for various Reynolds numbers. Figs. 6.13 and 6.14 show that the effects of flow on nondimensional current at space potential increase rapidly as Re and Sc_c increase.

Computed values of probe current are presented in tabular form in Table III. As we discussed in Chap. 3, the above solutions for total current, local current density and density contour maps can be applied to both ions and electrons, but with φ_p/ϵ_1 and Ra_i for ions replaced by $-\varphi_p$ and Ra_e , respectively, for electrons.

CHAPTER VII

7. COMPARISON WITH EXPERIMENTS AND OTHER THEORIES

No good experimental comparisons can be made with this work at the present time because of the difficulty of measuring small gas velocities (Barker 1922, Eckert and Soehngen 1952). However, we can apply experimental data on forced-convection heat or mass transfer to compare with our solutions for the space potential ($\varphi_p = 0$), because these problems are mathematical analogues of ours. To show this we rewrite equation (2.10) for $\varphi_p = 0$:

$$\frac{Re Sc_c}{2} \underline{u} \cdot \nabla n_c - \nabla^2 n_c = 0 \quad (7.1)$$

The equations of mass transfer and heat transfer, respectively, to a sphere or cylinder in flow are;

$$\frac{Re Sc}{2} \underline{u} \cdot \nabla \eta - \nabla^2 \eta = 0 \quad (\text{mass}) \quad (7.2)$$

$$\frac{Re Pr}{2} \underline{u} \cdot \nabla T - \nabla^2 T = 0 \quad (\text{heat}) \quad (7.3)$$

where Pr is the Prandtl number ($= c_v/\sigma$), σ is thermal conductivity, c is specific heat, and η is mass density of the diffusing constituent.

Comparing Eqs. (7.1) (7.2) and (7.3), we see that all of these problems are mathematical analogues of each other. As a result, the form of the current dependence on Re and Sc_c in the plasma probe problem is the same as that of the heat transfer on Re and the Prandtl number Pr, or that of the mass transfer on Re and the Schmidt number, respectively (Parker, 1974). The usual nondimensional forms of the heat and mass transfer are the Nusselt number Nu and the Sherwood

number Sh , respectively, where $Nu = 2R_p h / \sigma(T_\infty - T_{\text{surface}})$,
 h = total heat transfer, and $Sh = 2R_p b / D \eta_\infty$, b = total mass
transfer .

In Appendix A we show that a fourth problem also falls into
this category, namely the electrostatic probe problem in the
quasineutral limit $R_p / \lambda_D \rightarrow \infty$. In this case, we replace $i = f(Re, Sc_c)$
at space potential by $i_a = f(Re, Sc_a)$, where $Sc_a = v / D_a$, and D_a is
the ambipolar diffusion coefficient. In this condition, there is
no potential dependence in the probe current.

7.1 CYLINDER IN CROSS-FLOW

In Fig. 7.1, the numerical results for the ratio j/i of the ion or the electron local currents to the total current per unit length are compared with the heat transfer theory of Dennis et al (1968) and the heat transfer experimental data of Eckert and Soehngen (1952) for $Sc_c = 0.73$ (or $Pr = 0.73$). Both the present work and the work of Dennis et al are for $Re = 20$. The dotted lines are the experimental results of Eckert and Soehngen at $Re = 23$ (Eckert and Soehngen determined Re by the empirical expression for total Nusselt number $Nu = 0.43 + 0.48\sqrt{Re}$. If we instead use our numerical total Nusselt number results, this value is 25.) with the correction for the finite length effect which is suggested by Jensen and Kurzius (1969).

The theory of Dennis et al (1968) is based on their numerical neutral-flow solution (Dennis and Shimshoni 1965), and on solving Eq. (7.3) by a series truncation method. But this series truncation method causes calculation difficulty at larger values of the Reynolds number and the Prandtl number (Dennis et al 1973).

The wake effect in the rear stagnation region is apparent in both the experimental work and the present work in Fig. 7.1 and we observe differences between the present numerical values and experimental values of up to about 50%. This may be partly due to

differences in location of separation point of the neutral flow in the two cases. The disagreement between the work of Dennis et al and the present work may be due to computational instability in the numerical method of Dennis et al in the wake region (Chapter 4). On the basis of numerical tests (Sec. 4.3) of our own calculation, we believe that our results are accurate to within 5%. The ratio j/i of local current density to the total current per unit length is shown as a function of angle in Fig. 7.2 for $Re = 100$, $Ra_a = 10^4$, $R_p/\lambda_D \rightarrow \infty$. The points are the combustor duct experimental results of Tsuji and Hirano (1973) for $Re = 87 - 144$, $Ra_a = (8.87 - 14.4) \times 10^3$ and $R_p/\lambda_D \simeq 10^3$. Also shown in Fig. 7.2 is the arrangement of test cylinder and local current probe used in their experiment. The largest disagreement with the experiment occurs in the range $\theta = 95^\circ - 145^\circ$. Causes of this may include the following:

(1) The dimensions of the experimental chamber were only 56 and 5.6 probe diameters parallel and perpendicular to the cylinder axis, respectively, so that the boundary layer of the chamber may have significantly disturbed the neutral flow around the test cylinder.

(2) Edge effects on the local current probe (Fig. 7.2) may have affected the local current density measurements.

(3) $R_p/\lambda_D \simeq 10^3$ may not be large enough for a good comparison with a theory for $R_p/\lambda_D \rightarrow \infty$, because the local current density for this theory has no potential dependence and the experimental

results still show a substantial dependence (Tsuji and Hirano 1973).

The total current at space potential is compared with various heat and mass transfer experiments in Fig. 7.3. In this diagram, the experimental values are corrected for finite length effects (Jensen and Kurzius 1969). Differences up to 50% between the results are apparent. On the other hand, our results for this case appear to be accurate to 2%. This disagreement might be due to a basic instrumental difficulty in measuring velocities at these Reynolds numbers (Barker, 1922, Eckert and Soehngen 1952). Another possibility of error in heat transfer data might be from the thermal conductivity vs temperature relationship (Kassoy, 1967). The experimental calibration of Tsuji and Hirano (1973) for $Re = 87 - 167$ shows:

$$i \propto Re^{0.52}$$

This relationship agrees well with the present result for $R_p/\lambda_D \rightarrow \infty$, that is $i \propto Re^{0.5}$ for larger Schmidt numbers (Appendix A and Fig. 5.13).

7.2 SPHERE IN FLOW

Numerical results for ion or electron local currents at space potential are compared with the heat transfer theory of Dennis et al (1973) in Fig. 7.4 for $Re = 20, 0.5$ and 0 . The solutions disagree with each other even if we consider the difference of the value of Sc (according to the result for total current (Fig. 6.14), we expect the current for $Sc = 0.73$ to be a few percent smaller than for $Sc = 1$, and their values in fig. 7.5 are always larger than ours). Furthermore, local current density values in the rear stagnation region must always be smaller than in the stationary ($Re = 0$) case because the effect of flow without a wake is always to carry charge away from the rear stagnation region. The solution of Dennis et al for $Re = 20$ in fig. 7.4 clearly violates this requirement. This result may be due to computational instability of their numerical method in the rear stagnation region (see Chapter 4.1). Total currents at space potential are compared with various heat and mass transfer experiments in Fig. 7.5. The theory of Rimmer (1968) agrees well at smaller Reynolds numbers with the present results. At larger Reynolds numbers ($Re > 1$), the Rimmer theory becomes inapplicable because it is based on the small Reynolds number solution of the Navier-Stokes equation and the numerical solution of Dennis et al may be affected by instabilities as described above. The theory of Gupalo and Ryazantsev (1972) agrees reasonably well with ours at larger Reynolds numbers ($Re \gtrsim 60$). Their work is based on an analytic neutral flow solution (Van Dyke 1964, p. 159) which is applicable at Reynolds numbers up to 120.

The present results for local current density at the front stagnation point are compared in Fig. 7.6 with other theories for charged particle Schmidt numbers $Sc_c = 1$ and 100. The present results agree well with the results of Koderá (1975), Dennis et al (1973), Gupalo and Ryazantsev (1969) and Rimmer (1968, 1969) for smaller charged particle Schmidt numbers and also with Koderá (1975) and Eckert and Drake (1972 p. 413) at larger charged particle Schmidt numbers. They do not agree well with Eckert and Drake (1972) at smaller charged particle Schmidt numbers, nor with Gupalo and Ryazantsev (1969) at larger charged particle Schmidt numbers.

CHAPTER VIII

8. CONCLUDING REMARKS

A method has been developed and used to obtain theoretical predictions of the current collected from a continuum, low density flowing plasma by an electrically conducting electrostatic probe having spherical or cylindrical symmetry; the results for the cylinder have the advantage of being applicable to a magnetoplasma measurement. The probe characteristic has been determined for both spherical and cylindrical geometries for charged Schmidt numbers up to 10^5 , for Reynolds numbers from 0.1 to 100 for the cylinder and 0.1 to 60 for the sphere, for nondimensional probe potentials from -12 to 10 and for arbitrary ion-to-electron temperature ratios. Each current collection result has been computed to a relative accuracy of 2% or better in an average time of approximately 20 minutes on the CDC 6600 including a relative accuracy of 0.4% or better at stationary conditions compared with the analytic solution (Eq. B.1). Numerical solutions by other authors (Figs. 3.1 and 3.2 for the cylinder and Fig. 3.3 for the sphere) have been used for the neutral flow. The electric potential profiles used for the cylinder are logarithmic, obtained by using the Laplace potential at the equator of a prolate spheroid approximated for radii \ll the major axis. This leads to a scaling for probe potential which makes the results applicable to all large enough values of probe length to diameter ratio. The electric potential profiles used for the sphere are proportional to r^{-1} , obtained by using the Laplace potential. The charge transport equations are solved using an upwind difference method developed for time independent situations.

The numerical results for the total current show that :

(1) For a probe at retarding potentials, the effects of Re and Sc_c increase with the potential and the usual "retarding potential" method for temperature determination leads to large errors (Sec. 5.3 and Sec. 6.3, Figs. 5.8, 6.10 and 6.11).

(2) For small potentials, the effects of Re and Sc_c decrease with increasing attracting potential and the effect of the flow is to smooth the "knee" of the probe characteristics and to render more imprecise the determination of the space potential (Figs. 5.8, 6.10, and 6.11).

(3) At large enough attracting potential, the linear dependence for probe current $i \propto \varphi_p$ from the stationary theory is recovered as one would expect (Fig. 5.11 and 5.12). Therefore, an improved method for probe measurements can be applied to the determination of the electron or ion temperature (Sec. 5.3, Appendix B).

(4) The probe current has only very slight dependence on both Re and Sc_c at large attracting surface potentials (Sec. 5.3 and Sec. 6.3, Figs. 5.8, 6.10 and 6.11).

(5) Comparison between the present work and experiments shows good agreement in many but not all cases. (Chapter 7, Figs. 7.3, 7.5 and 7.6). Explanations are proposed for cases showing substantial disagreement.

(6) The present theory for a cylinder in a cross-flow can be applied with minor changes to a magneto-plasma with field aligned with

the cylinder axis (Sec. 5.4).

The numerical results for the charge density distribution around the body show that:

- (1) the charge density profiles near a body become unsymmetrical when Sc_c and Re are increased (Sec. 5.1 and Sec. 6.1, Figs. 5.1, 6.1, and 6.2).
- (2) A wake (recirculation region) in the neutral flow behind the body can have large effects on the charge density profiles downstream. (Sec. 5.1, and Sec. 6.1, Figs. 5.1 and 6.2).
- (3) the effects of surface potential on the charge density profiles of a body are larger downstream than upstream (Sec. 5.1 and Sec. 6.1, Figs. 5.1 and 6.3).
- (4) at large enough attracting potentials the charged particle density profiles become symmetrical (Sec. 5.1 and Sec. 6.1, Figs. 5.1, 6.3 and 6.4).
- (5) in the presence of flow, the profiles of net charge density can include several regions of alternating sign downstream of the body (Sec. 5.1 and Fig. 5.2).
- (6) the numerical results of local current density can be used to estimate ion collection by a mass spectrometer on a rocket or balloon up to the D region, or in flames and flowing afterglows. (Sec. 5.2, Figs. 5.3, 5.4, 5.5; Sec. 6.2, Figs. 6.5, 6.6 and 6.7).

REFERENCES

- M. Barker (1922), On the Use of Very Small Pitot Tubes for Measuring Wind Velocities, Proc. Royal Soc. London 101, 435
- D. Bohm, E. Burhop and H. Massey (1949) "The Characteristics of Electrical Discharge in Magnetic Fields", ed. A. Guthrie and R.K. Wakerling, New York, McGraw-Hill.
- B.G. Carlson (1953) in R.D. Richtmyer and K.W. Morton (1957) p. 240 "Difference Methods for Initial-Value Problems" Interscience Publishers, New York
- J.S. Chang (1973) The Inadequate Reference Electrode, a Widespread Source of Error in Plasma Probe Measurements, J. Phys. D. 6, 1674-83.
- ____ (1975) Theory of Mass-Discrimination Effects on Ion Extraction from Continuum Flowing Plasmas, Int. J. Mass. Spect. & Ion Phys. 16, 448-450.
- J.S. Chang and J.G. Laframboise (1975) Probe Theory for Arbitrary Shape in a Large Debye Length, Stationary Plasma (Submitted to Phys. Fluids)
- R.L. Chapkis and E. Baum (1971) Theory of a Cooled Spherical Electrostatic Probe in a Continuum Gas, AIAA J. 9, 1963-8.
- S.L. Chen, J.S. Chang and S. Matsumura (1970) Electrostatic Probe Determination of Electron Density in a Medium Pressure (0.2-22 Torr) Discharge Plasma of Argon, J. Appl. Phys. 41, 1711-5.

- _____ (1971) Studies of the Large Sheath Concept for the Continuum Theory, J. Appl. Phys. 42, 499-501.
- P.M Chung, L. Talbot and K.J. Touryan (1974) Electrostatic Probes in Stationary and Flowing Plasma: Part 2. Continuum Probes, AIAA J. 12, 144-54.
- R.M. Clements and P.R. Smy (1969) Electrostatic Probe Studies in a Flame Plasma, J. Appl. Phys. 40, 4553-8.
- _____ (1970) Ion Current from a Collision-Dominated Flowing Plasma to a Cylindrical Electrode Surrounded by a Thin Sheath, J. Appl. Phys. 41, 3745-9.
- I.R. Cohen (1963) Asymptotic Theory of Spherical Electrostatic Probes in a Slightly Ionized, Collision-Dominated Gas, Phys. Fluids 6, 1492-9.
- D.C. Collis and M.J. Williams (1959) Two-Dimensional Convection from Heated Wires at Low Reynolds Numbers, J. Fluid Mech. 6, 357-84.
- S.C.R. Dennis and G.Z. Chang (1970) Numerical Solutions for Steady Flow Past a Circular Cylinder at Reynolds Numbers up to 100, J. Fluid Mech. 42, 411-89.
- S.C.R. Dennis, J.D. Hudson and N. Smith (1968) Steady Laminar Forced Convection from a Circular Cylinder at Low Reynolds Number, Phys. Fluids 11, 933-40.

- S.C.R. Dennis and J.D. Hudson (1973), Private Communication
- S.C.R. Dennis and M. Shimshoni (1965) Calculation of the Steady Flow Past a Circular Cylinder at Low Reynolds Numbers, Aeronautical Research Council, Current Paper No. 797 (Her Majesty's Stationery Office, London, England)
- S.C.R. Dennis and J.D.A. Walker (1971) Calculation of the Steady Flow Past a Sphere at Low and Moderate Reynolds Numbers, J. Fluid Mech. 48, 771-89.
- S.C.R. Dennis, J.D.A. Walker and J.D. Hudson (1973) Heat Transfer from a Sphere at Low Reynolds Numbers, J. Fluid Mech. 60, 273-83.
- R. Dobry and R.K. Finn (1956) Mass Transfer to a Cylinder at Low Reynolds Number, Ind. Eng. Chem. 48, 1540-3.
- E.R.G. Eckert and E. Soehngen (1952) Distribution of Heat Transfer Coefficients Around Circular Cylinders in Crossflow at Reynolds Numbers from 20 to 500, Trans. ASME Heat Trans. 74, 343-7.
- E.R.G. Eckert and R.M. Drake, Jr. (1972) "Analysis of Heat and Mass Transfer", McGraw-Hill, New York.
- F. Fendell (1970) Nonequilibrium Continuum Theory of Spherical Electrostatic Probes at Large Debye Number, Comb. Sci. & Tech. 1, 331-8.
- S.K. Friedlander (1957) Mass and Heat Transfer to Single Spheres and Cylinders at Low Reynolds Numbers. A.I. Ch. E. J.3, 43-8.
- T. Fukuda (1969) "Difference Equations", Iwaname Press, Tokyo. (in Japanese)
- D. Greenspan (1974) "Discrete Numerical Methods in Physics and Engineering" Academic Press, New York.

- Yu. P. Gupalo and Yu. S. Ryazantsev (1969) Diffusion to a Solid Spherical Particle in a Viscous Fluid Flow for Finite Reynolds Number, Fluid Dynamics, (U.S.S.R.) 6, 82-3.
- T. Hirano (1972) An Analysis of the Positive-Ion Current to a Cylinder in a Weakly Ionized Gas, Bulletin of JSME 15, 1402-9.
- D.R. Hoult (1965) D-Region Probe Theory, J. Geophys. Res. 70, 3183-7.
- R.W. Huggins (1974) Interpretation of Electrostatic Probe Data Taken in a Flowing Plasma, J. Appl. Phys. 45, 710-16.
- D.E. Jensen and S.C. Kurzius (1969) Determination of Positive Ion Concentrations in High-Velocity Laminar Flames, Comb. Flame 13, 219-21.
- D.R. Kassoy (1967) Heat Transfer from Circular Cylinders at Low Reynolds Numbers I: Theory for Variable Property Flow, Phys. Fluids 10, 938-46.
- K. Kodera (1975) Theory of Electrostatic Probes in a Flowing Continuum Plasma: Exact Solution for Sphere Stagnation Point. (In Press; Groupe de Recherches Ionosphériques, Paris, France, note technique No. 137).
- R.E. Keil (1968) Continuum Electrostatic Probe Theory for Large Sheaths on Spheres and Cylinders J. Appl. Phys., 40, 3668-73.
- J.G. Laframboise (1966) Theory of Spherical and Cylindrical Langmuir Probes in a Collisionless, Maxwellian Plasma at Rest. Univ. of Toronto, Institute for Aerospace Studies, Report No. 100.
- S.H. Lam (1964) A General Theory for the Flow of Weakly Ionized Gases, AIAA J. 2, 256-62.

- C.E. Leith (1965) Numerical Simulation of the Earth's Atmosphere, Methods in Comp. Phys. 4, 1-28.
- J.M. McCormick and M.G. Salvadori (1964) "Numerical Methods in FORTRAN", Prentice-Hall Press, New Jersey.
- P. Moon and D.E. Spencer (1961) "Field Theory for Engineers" D. Van Nostrand Co. Inc., Princeton, New Jersey.
- H.M. Mott-Smith and I. Langmuir (1926) Theory of Collectors in Gaseous Discharges, Phys. Rev. 28, 727-63.
- L.W. Parker (1974) Theory of Ion Collection in the D-Region by a Rapidly Moving Blunt Probe or Mass Spectrometer, National Oceanic and Atmospheric Administration Technical Report ERL 311-AL-1D.
- P.L. Rimmer (1968) Heat Transfer from a Sphere in a Stream of Small Reynolds Numbers, J. Fluid Mech. 32, 1-7 (See also 35, 827-29), (1969)]
- G.D. Smith (1965) "Numerical Solution of Partial Differential Equations", Oxford University Press.
- C.H. Su and R.E. Keil (1966) Continuum Theory of Electrostatic Probes, J. Appl. Phys. 37, 4907-10.
- C.H. Su and S.H. Lam (1963) Continuum Theory of Spherical Electrostatic Probes, Phys. Fluids 6, 1479-91.
- H. Takami and H.B. Keller (1969) Steady Two-Dimensional Viscous Flow of an Incompressible Fluid Past a Circular Cylinder, Phys. Fluids. Suppl. II, II 51-6.

H. Tsuji and T. Hirano (1973) Ion-Current Distributions Around
an Electrically Conductive Body in Ionized Gas Flow, AIAA
J. 11, 100-3.

A.A. Yastrebov (1971) Contribution to the Theory of Probe Measurements
in the Lower Ionosphere, Geomagn. & Aeronomy (U.S.S.R.)
12, 748-53.

M.D. Van Dyke (1964) "Perturbation Methods in Fluid Mechanics"
Academic Press, New York.

T. Yuge (1956) Theory of Heat Transfer of Spheres in Uniform
Stream at Low Reynolds Numbers, Reports of Institute of
High Speed Mechanics, Japan, 6, 143-51.

____ (1960) Experiments on Heat Transfer From Spheres Including
Combined Natural and Forced Convection, Trans. ASME. Heat
Transfer C 82, 214-20.

Williams (1954) in W.H. McAdams "Heat Transmission" McGraw-Hill
Press N.Y. p. 266.

APPENDICES

APPENDIX A: Application of Theory to Quasi-Neutral Conditions :

$$R_p / \lambda_D \rightarrow \infty$$

Our numerical treatment of Eqs. (3.13) and (3.17) can also be applied to large Debye ratio continuum plasmas, i.e. $R_p / \lambda_D \rightarrow \infty$. In this limit we can assume $N_i \simeq N_e \simeq N$. Then from Eqs. (3.1) and (3.2), we obtain (Lam, 1964)

$$\underline{J} = \underline{J}_e - \underline{J}_i = (D_i - D_e) \nabla N + (\mu_e + \mu_i) N \nabla V \quad (\text{A-1})$$

$$\therefore \nabla V = \frac{\underline{J}}{(\mu_e + \mu_i) N} + \frac{(D_e - D_i)}{\mu_e + \mu_i} \frac{\nabla N}{N} \quad (\text{A-2})$$

$$\text{and } \underline{J}_e - \frac{\mu_e}{\mu_e + \mu_i} \underline{J} = N \underline{U} - D_a \nabla N \quad (\text{A-3})$$

$$\underline{J}_i + \frac{\mu_i}{\mu_e + \mu_i} \underline{J} = N \underline{U} - D_a \nabla N \quad (\text{A-4})$$

$$\text{where } D_a = \frac{D_e \mu_i + D_i \mu_e}{\mu_e + \mu_i}$$

Now we take the divergence of either (A-3) or (A-4). We recall that

$\nabla \cdot \underline{u} = 0$ and $\nabla \cdot \underline{J}_e = \nabla \cdot \underline{J}_i = 0$. In non-dimensional form, we obtain:

$$\frac{Ra_a}{2} \underline{u} \cdot \nabla n - \nabla^2 n = 0 \quad (\text{A-5})$$

where

$$Ra_a = \frac{2U R_p}{D_a} = Re Sc_a = \frac{2U R_p}{\nu} \times \frac{\nu}{D_a}$$

We note that $D_a = 2D_i$ when $T_i = T_e$, $D_a \rightarrow D_e$ when $T_e \gg T_i$.

In this quasineutral problem the boundary conditions are
(Lam, 1964, Eq. 4.2):

$$n \rightarrow 1 \text{ as } r \rightarrow \infty$$

$$n = 0 \text{ at } r = r^* \simeq 1 \quad (\text{sheath edge})$$

Lam then shows that $r^* \rightarrow 1$ in the limit as $R_p/\lambda_D \rightarrow \infty$ (See discussion following Eq. 6.13 in Lam, 1964). Our situation therefore is equivalent to that for space potential in Chapters 5 and 6, but with Sc_c replaced by Sc_a . Therefore no potential dependence will exist in probe characteristics in the limit $R_p/\lambda_D \rightarrow \infty$.

APPENDIX B: Application to Plasma Diagnostic Method

The exact analytic current-voltage characteristic previously obtained by Fendell (1970) and by Chapkis and Baum (1971) for spheres in the continuum Laplace limit $\lambda_c \ll R_p \ll \lambda_D$, has been obtained by Chang and Laframboise (1975) for arbitrarily shaped probes in the same limit. This is

$$i_e = \frac{\varphi_p}{1 - \exp(-\varphi_p)} ; \quad i_i = \frac{-\varphi_p}{[1 - \exp(\varphi_p/\epsilon_i)]\epsilon_i} \quad (\text{B-1})$$

At a large attracting potential, Eq. B.1 immediately yields $i_e = \varphi_p$ or $i_i = -\varphi_p/\epsilon_i$. (note: Equation B.1 cannot be used to provide the stationary limit for our results for cylinders in flow (Sec. 5.3), because these are in terms of the scaled surface potential $\varphi_p/\ln\Lambda$ instead of φ_p . However, if we have a large attracting potential, we obtain $i_e = \varphi_p/\ln\Lambda$ or $i_i = -\varphi_p/\epsilon_i \ln\Lambda$ from the analysis of Chang and Laframboise (1975, Sec. III) in the limit $L \rightarrow \infty$). We have also seen that this limiting linear behaviour is also recovered at large enough probe potentials in the flowing case (Sec. 5.3, 6.3, figs. 5.8-5.12, 6.10 and 6.11). We now propose a plasma diagnostic method based on this limiting behaviour. The method first requires measurement of currents I_1 , I_2 and I_3 at three potentials V_{1f} , V_{2f} and V_{3f} relative to floating potential V_f , where $V_{jf} \equiv V_j - V_f$. These potentials are arranged so that V_1 and V_2 are large and positive, and V_3 is large and negative. Therefore, from eq. B.1 we obtain approximately:

$$i_1 = \varphi_{1f} + \varphi_f \quad (\text{B-3a})$$

$$i_2 = \varphi_{2f} + \varphi_f \quad (\text{B-3b})$$

$$\epsilon_i i_3 = -\varphi_{3f} - \varphi_f \quad (\text{B-3c})$$

where φ_f is the floating potential of the probes relative to space. We solve (B-3a) and (B-3b) to obtain:

$$\varphi_f = \frac{i_2 \varphi_{1f} - i_1 \varphi_{2f}}{i_1 - i_2}$$

or
$$V_f = \frac{I_2 V_{1f} - I_1 V_{2f}}{I_1 - I_2} \quad (\text{B-4})$$

From equation (B-4), we obtain the floating potential V_f relative to space. The electron reference current I_{oe} can now be obtained from the probe current at space potential by using the relation

$I_e = I_{oe} i_e(0, Re, Sc_e)$ with $i_e = i_e(-\varphi_p, Re, Sc_e)$ provided by the results in Sections 5 and 6.

The electron temperature now can be obtained from Eqs.

(B-3a) and (B-3b) as

$$\frac{kT_e}{e} = \frac{I_{oe}(V_{1f} - V_{2f})}{I_1 - I_2} \quad (\text{B-5})$$

From Eqs. (B-3c), (B-4) and (B-5), we obtain the ion to electron temperature ratio as

$$\frac{T_i}{T_e} = \frac{D_i}{D_e} \frac{(I_2 V_{13} - I_1 V_{23})}{I_3 V_{21}} \quad (\text{B-6})$$

The current-voltage characteristic at large enough attracting potential, $i_p \propto \varphi_p$, is in good agreement with available experimental results for both sphere and cylinder geometry (Chen et al, 1970, 1971).

APPENDIX C. Computer Program Listings

R42C

THEORY OF ELECTROSTATIC PROBES IN A FLOWING CONTINUUM PLASMA

SUB-SONIC, INCOMPRESSIBLE FLOW
 POTENTIAL PROFILE = LAPLACE POTENTIAL
 NEUTRAL FLOW PROFILE = NUMERICAL SOLUTION OF NAVIER-STOKES EQUATION

SPHERICAL PROBE

NI=ION DENSITY, UT, UR=FLOW FIELD, S=STREAM FUNCTION, R=RADIUS,
 PJ=LOCAL CURRENT, PI=TOTAL CURRENT, F=SURFACE POTENTIAL,
 RE=DIFFUSION REYNOLDS NUMBER/2., ITER=ITERATIVE TIME, EPS=RESIDUAL

```

REAL NI,UT,UR,S,R,TD,PI1,RO,PI2,Q ,CO,DQ,PJ ,Q1,Q0,PJJ,T1,T2
DIMENSION NI(125,65),UT(125,65),UR(125,65),T2(65),R(125),Q(125,65)
1,CO(125,65),DQ(125),PJ(65),Q0(125,65),Q1(125,65),PJJ(65),T1(65)
RO=0.03
N=63
TD=3.141615/(N-3.)
ITMAX=4000
EPSMAX=1.0F-3
NP1=N+1
NP4=N-2
NP2=N-1
NP3=N+2
F=10
K=123
KP1=K+1
KP2=K-1
KP3=K+2
KP4=K-2
KP5=K+3

```

FLOW PROFILE

```

READ(5,300)((UR(I,J),I=2,120),J=3,N)
WRITE(6,209)
READ(5,300)((UT(I,J),I=2,120),J=3,N)
WRITE(6,208)
DO 53 J=1,NP3
T1(J)=SIN((J-3.)*TD)
53 T2(J)=COS((J-3.)*TD)
DO 55 J=1,NP3
DO 55 I=121,KP3
UR(I,J)=T2(J)+0.00001
55 UT(I,J)=-T1(J)
DO 56 I=121,KP3
UT(I,3)=0.
56 UT(I,N)=0.
DO 10 I=1,KP3
10 Q(I)=EXP(RO*(I-2.))
WRITE(6,204)
WRITE(6,301)(R(I),I=1,KP3)

```

ION DENSITY PROFILE

BOUNDARY CONDITIONS

```

DO 2 J=1,NP3
NI(1,J)=0.0
NI(2,J)=0.0
DO 2 I=3,KP3
2 NI(I,J)=1.-1./R(I)

```

2ND. ORDER UP-WIND DIFFERENCE METHOD
UP-WIND DIFFERENCE FACTOR

```

DO 97 J=4,NP2
DO 97 I=3,K
97 Q(I,J)=(ABS((UT(I,J)/UR(I,J))))*RO/TD

```

```

DO 96 J=4, NP2
DO 96 I=3, K
96 QO(I, J)={ABS((UR(I, J)/UT(I, J)))*YO/RD
WRITE(6, 215)
1 READ(5, 505) RE
WRITE(6, 505) RE
C
DO 5 I=3, K
DO 5 J=4, NP2
IF(O(I, J)-1.0) 58, 58, 59
58 CO(I, J)=RE*ABS(UR(I, J))/RD
GO TO 5
59 CO(I, J)=RE*ABS(UT(I, J))/TD
5 CONTINUE
C
ITER=0
3 FPS=0.0
ITER=ITER+1
DO 4 I=3, K
DO 4 J=3, N
HOLDT=NI(I, J)
V=RD**2.
U=TD**2.
NI(I, 1)=NI(I, 5)
NI(I, 2)=NI(I, 4)
NI(I, NP1)=NI(I, NP2)
NI(I, NP3)=NI(I, NP4)
NI(KP3, 2)=NI(KP3, 4)
NI(KP3, 1)=NI(KP3, 5)
NI(KP3, NP3)=NI(KP3, NP4)
NI(KP3, NP1)=NI(KP3, NP2)
NI(KP1, 1)=NI(KP1, 5)
NI(KP1, 2)=NI(KP1, 4)
NI(KP1, NP3)=NI(KP1, NP4)
NI(KP1, NP1)=NI(KP1, NP2)
NI(KP1, J)=1.-(1.-NI(K, J))*((R(K)/R(KP1))*EXP(-RE*(R(KP1)-
R(K)))*(1.-T2(J))/2.)
NI(KP3, J)=1.-(1.-NI(KP1, J))*((R(KP1)/R(KP3))*EXP(-RE*(R(KP3)-
R(KP1)))*(1.-T2(J))/2.)
Q1(I, J)=(ABS((UT(I, J)+0.00001)/(UR(I, J)+0.00001)))*RD/TD
DQ(I)=2.*(V+U)/(U*V*R(I))
IF(UR(I, J)-0.0) 70, 70, 71
70 IF(UT(I, J)-0.0) 72, 84, 74
72 IF(Q1(I, J)-1.0) 76, 77, 77
76 NI(I, J)={((1.-Q(I, J))*NI(I+1, J))*((3.*Q(I, J)-1.)*Q(I, J)+2.)
+NI(I+1, J+2)*Q(I, J)*(Q(I, J)-1.)-NI(I+1, J-1)*(Q(I, J)**2.))/2.
+Q(I, J)*NI(I+1, J+1)*(4.+Q(I, J))*(-5.+3.*Q(I, J))/2.}
1*(CO(I, J)/(CO(I, J)+DQ(I)))+(NI(I+1, J)*(2.+RD)+NI(I-1, J)*(2.-RD))
2*U+(NI(I, J+1)*(2.+TD*(T2(J)/T1(J)))+NI(I, J-1)*(2.-TD*(T2(J)/T1(J))
3)*V)*DQ(I)/((CO(I, J)+DQ(I))*(4.*(U+V)))+(F/((R(I)**3.)*2.*RD)**
4(NI(I+1, J)-NI(I-1, J))*(1./(DQ(I)+CO(I, J)))
GO TO 90
77 NI(I, J)={((1.-QO(I, J))*NI(I, J+1))*((3.*QO(I, J)-1.)*QO(I, J)+2.)
+NI(I+2, J+1)*QO(I, J)*(QO(I, J)-1.)-NI(I-1, J+1)*QO(I, J)**2.))/2.
+NI(I+1, J+1)*QO(I, J)*(4.+QO(I, J))*(-5.+3.*QO(I, J))/2.}
1*(CO(I, J)/(CO(I, J)+DQ(I)))+(NI(I+1, J)*(2.+RD)+NI(I-1, J)*(2.-RD))
2*U+(NI(I, J+1)*(2.+TD*(T2(J)/T1(J)))+NI(I, J-1)*(2.-TD*(T2(J)/T1(J))
3)*V)*DQ(I)/((CO(I, J)+DQ(I))*(4.*(U+V)))+(F/((R(I)**3.)*2.*RD)**
4(NI(I+1, J)-NI(I-1, J))*(1./(DQ(I)+CO(I, J)))
GO TO 90
84 NI(I, J)=NI(I+1, J)
1*(CO(I, J)/(CO(I, J)+DQ(I)))+(NI(I+1, J)*(2.+RD)+NI(I-1, J)*(2.-RD))
2*U+(NI(I, J+1)*(2.+TD*(T2(J)/T1(J)))+NI(I, J-1)*(2.-TD*(T2(J)/T1(J))
3)*V)*DQ(I)/((CO(I, J)+DQ(I))*(4.*(U+V)))+(F/((R(I)**3.)*2.*RD)**
4(NI(I+1, J)-NI(I-1, J))*(1./(DQ(I)+CO(I, J)))
GO TO 90
74 IF(O1(I, J)-1.0) 80, 81, 81
80 NI(I, J)={((1.-Q(I, J))*NI(I+1, J))*((3.*Q(I, J)-1.)*Q(I, J)+2.)
+NI(I+1, J+2)*Q(I, J)*(Q(I, J)-1.)-NI(I+1, J+1)*Q(I, J)**2.))/2.
+Q(I, J)*NI(I+1, J+1)*(4.+Q(I, J))*(-5.+3.*Q(I, J))/2.}
1*(CO(I, J)/(CO(I, J)+DQ(I)))+(NI(I+1, J)*(2.+RD)+NI(I-1, J)*(2.-RD))
2*U+(NI(I, J+1)*(2.+TD*(T2(J)/T1(J)))+NI(I, J-1)*(2.-TD*(T2(J)/T1(J))
3)*V)*DQ(I)/((CO(I, J)+DQ(I))*(4.*(U+V)))+(F/((R(I)**3.)*2.*RD)**
4(NI(I+1, J)-NI(I-1, J))*(1./(DQ(I)+CO(I, J)))
GO TO 90
81 NI(I, J)={((1.-QO(I, J))*NI(I, J-1))*((3.*QO(I, J)-1.)*QO(I, J)+2.)
+NI(I+2, J-1)*QO(I, J)*(QO(I, J)-1.)-NI(I-1, J-1)*QO(I, J)**2.))/2.
+NI(I+1, J-1)*QO(I, J)*(4.+QO(I, J))*(-5.+3.*QO(I, J))/2.}
1*(CO(I, J)/(CO(I, J)+DQ(I)))+(NI(I+1, J)*(2.+RD)+NI(I-1, J)*(2.-RD))
2*U+(NI(I, J+1)*(2.+TD*(T2(J)/T1(J)))+NI(I, J-1)*(2.-TD*(T2(J)/T1(J))
3)*V)*DQ(I)/((CO(I, J)+DQ(I))*(4.*(U+V)))+(F/((R(I)**3.)*2.*RD)**

```

```

4(NI(I+1,J)-NI(I-1,J))*(1./(DQ(I)+CO(I,J)))
GO TO 90
71 IF(UT(I,J)-0.0)73,85,75
73 IF(CO(I,J)-1.0)73,79,79
78 NI(I,J)=((1.-O(I,J))*(NI(I-1,J)*((3.*O(I,J)-1.)*O(I,J)+2.)
+NI(I-1,J+2)*O(I,J)*(O(I,J)-1.-NI(I-1,J-1)*(O(I,J)**2.))/2.
+O(I,J)*(NI(I-1,J+1)*(4.+O(I,J)*(-5.+3.*O(I,J))))/2.)
1*(CO(I,J)/(CO(I,J)+DQ(I)))+(NI(I+1,J)*(2.+RD)+NI(I-1,J)*(2.-RD))
2*U+(NI(I,J+1)*(2.+TD*(T2(J)/T1(J)))+NI(I,J-1)*(2.-TD*(T2(J)/T1(J))
3)*V)*(DQ(I)/(CO(I,J)+DQ(I))*(4.*(U+V)))+(F/((R(I)**3.)*2.*RD))*
4(NI(I+1,J)-NI(I-1,J))*(1./(DQ(I)+CO(I,J)))
GO TO 90
79 NI(I,J)=((1.-OQ(I,J))*(NI(I,J+1)*((3.*OQ(I,J)-1.)*OQ(I,J)+2.)
+NI(I-2,J+1)*(OQ(I,J)-1.)*OQ(I,J)-NI(I+1,J+1)*(OQ(I,J)**2.))/2.
+NI(I-1,J+1)*OQ(I,J)*(4.+OQ(I,J)*(-5.+3.*OQ(I,J)))/2.)
1*(CO(I,J)/(CO(I,J)+DQ(I)))+(NI(I+1,J)*(2.+RD)+NI(I-1,J)*(2.-RD))
2*U+(NI(I,J+1)*(2.+TD*(T2(J)/T1(J)))+NI(I,J-1)*(2.-TD*(T2(J)/T1(J))
3)*V)*(DQ(I)/(CO(I,J)+DQ(I))*(4.*(U+V)))+(F/((R(I)**3.)*2.*RD))*
4(NI(I+1,J)-NI(I-1,J))*(1./(DQ(I)+CO(I,J)))
GO TO 90
85 NI(I,J)=NI(I-1,J)
1*(CO(I,J)/(CO(I,J)+DQ(I)))+(NI(I+1,J)*(2.+RD)+NI(I-1,J)*(2.-RD))
2*U+(NI(I,J+1)*(2.
)+NI(I,J-1)*(2.
3)*V)*(DQ(I)/(CO(I,J)+DQ(I))*(4.*(U+V)))+(F/((R(I)**3.)*2.*RD))*
4(NI(I+1,J)-NI(I-1,J))*(1./(DQ(I)+CO(I,J)))
GO TO 90
75 IF(OI(I,J)-1.0)82,83,83
82 NI(I,J)=((1.-O(I,J))*(NI(I-1,J)*((3.*O(I,J)-1.)*O(I,J)+2.)
+NI(I-1,J-2)*O(I,J)*(O(I,J)-1.-NI(I-1,J+1)*(O(I,J)**2.))/2.
+O(I,J)*(NI(I-1,J-1)*(4.+O(I,J)*(-5.+3.*O(I,J))))/2.)
1*(CO(I,J)/(CO(I,J)+DQ(I)))+(NI(I+1,J)*(2.+RD)+NI(I-1,J)*(2.-RD))
2*U+(NI(I,J+1)*(2.+TD*(T2(J)/T1(J)))+NI(I,J-1)*(2.-TD*(T2(J)/T1(J))
3)*V)*(DQ(I)/(CO(I,J)+DQ(I))*(4.*(U+V)))+(F/((R(I)**3.)*2.*RD))*
4(NI(I+1,J)-NI(I-1,J))*(1./(DQ(I)+CO(I,J)))
GO TO 90
83 NI(I,J)=((1.-OQ(I,J))*(NI(I,J-1)*((3.*OQ(I,J)-1.)*OQ(I,J)+2.)
+NI(I-2,J-1)*(OQ(I,J)-1.)*OQ(I,J)-NI(I+1,J-1)*(OQ(I,J)**2.))/2.
+NI(I-1,J-1)*OQ(I,J)*(4.+OQ(I,J)*(-5.+3.*OQ(I,J)))/2.)
1*(CO(I,J)/(CO(I,J)+DQ(I)))+(NI(I+1,J)*(2.+RD)+NI(I-1,J)*(2.-RD))
2*U+(NI(I,J+1)*(2.+TD*(T2(J)/T1(J)))+NI(I,J-1)*(2.-TD*(T2(J)/T1(J))
3)*V)*(DQ(I)/(CO(I,J)+DQ(I))*(4.*(U+V)))+(F/((R(I)**3.)*2.*RD))*
4(NI(I+1,J)-NI(I-1,J))*(1./(DQ(I)+CO(I,J)))
90 CONTINUE
4 EPS=EPS+ARS(NI(I,J)-HOLDT)
IF(EPS.LE.EPSMAX)GO TO 6
IF(ITER-ITMAX)3,7,8
6 WRITE(6,201) ITER
DO 7 I=3,K
7 WRITE(6,501)(NI(I,J),J=3,N)
WRITE(7,503)((NI(I,J),I=3,KP4),J=3,N)
GO TO 91
8 WRITE(6,203)
DO 9 I=1,KP3
9 WRITE(6,301)(NI(I,J),J=1,NP3)
91 WRITE(6,210)

CURRENT
LOCAL CURRENT
DO 51 J=3,N
51 PJ(J)=(32.*NI(3,J)-12.*NI(4,J)+NI(6,J))/(12.*RD)
WRITE(6,206)
WRITE(6,501)(PJ(J),J=3,N)

TOTAL CURRENT
PI1=0.0
DO 50 J=4,NP2,2
50 PI1=PI1+TD*(PJ(J-1)+4.*PJ(J)+PJ(J+1))/3.
WRITE(6,502)PI1
NPP=(N-3.)/2.
PI2=0.
DO 48 I=2,NP8,2
48 PI2=PI2+TD*2.*(PJ(2*I-1)+4.*PJ(2*I+1)+PJ(2*I+3)) /3.
WRITE(6,502)PI2
WRITE(6,207)
PIC=(16.*PI1 -PI2 )/15.
WRITE(6,500)PIC,PI1,PI2
DO 52 J=3,N

```

UUUUUU
UUUUUU
UUUUUU

```

52 PJJ(J)=PJ(J)*T1(J)
   WRITE(6,211)
   WRITE(6,501)(PJJ( J),J=3,N)
   PI3=0.0
   DO 47 J=4,NP2,2
47 PI3=PI3+TD*(PJJ(J-1)+4.*PJJ(J)+PJJ(J+1))/3.
   WRITE(6,502)PI3
   PI4=0.0
   DO 46 J=2,NP8,2
46 PI4=PI4+TD*2.*(PJJ(2*J-1)+4.*PJJ(2*J+1)+PJJ(2*J+3))/3.
   WRITE(6,502)PI4
   WRITE(6,212)
   PICC=(16.*PI3-PI4)/15.
   WRITE(6,500)PICC,PI3,PI4
   GO TO 1
201 FORMAT(45HOCONVERGENCE CONDITION HAS BEEN REACHED AFTER,13,10MITER
1ATIONS)
203 FORMAT(15HONO CONVERGENCE)
204 FORMAT(9HODISTENCE)
206 FORMAT(5HOFUX)
207 FORMAT(14HOPROBE CURRENT)
208 FORMAT(4HOUT)
209 FORMAT(4HOUR)
210 FORMAT(4HONI)
211 FORMAT(14HLOCAL NUSSELT)
212 FORMAT(14HOTOTAL NUSSELT)
215 FORMAT(4HORE)
503 FORMAT(7E11.5)
300 FORMAT(7E11.4)
500 FORMAT(F10.6,F10.6,F10.6)
301 FORMAT(12F10.5/12F10.5/9F10.5/)
501 FORMAT(11E12.5)
502 FORMAT(F10.6)
504 FORMAT(12E11.5)
505 FORMAT(F10.3)
STOP
END

```

SENTRY

***** THIS IS END OF JOB *****

JOB WATF IV

R42C

THEORY OF ELECTROSTATIC PROBES IN A FLOWING CONTINUUM PLASMA

SUR-SONIC, INCOMPRESSIBLE FLOW

POTENTIAL PROFILE=LAPLACE POTENTIAL

NEUTRAL FLOW PROFILE=NUMERICAL SOLUTION OF NAVIER-STOKES EQUATION

CYLINDRICAL PROBE
CYLINDER IN CROSS-FLOWNI=ION DENSITY, UT, UR=FLOW FIELD, S=STREAM FUNCTION, R=RADIUS,
PJ=LOCAL CURRENT, PI=TOTAL CURRENT, F=SURFACE POTENTIAL,
RE=DIFFUSION REYNOLDS NUMBER/2., ITER=ITERATIVE TIME, EPS=RESIDUAL

```

REAL NI,UT,UR,S,R,TD,PI1,RD,PI2,0,CO,DQ,PJ,01,00,PJJ,T,TT
DIMENSION NI(65,65),UT(65,65),UR(65,65),S(65,65),R(65),O(65,65)
1,CO(65,65),DQ(65),PJ(65),00(65,65),01(65,65),PJJ(65),T(65)
2,TT(65)
N=63
TD=3.141615/60.
RD=3.141615/60.
ITMAX=2000
RE=2500
CD=4.116
EPSMAX=1.0E-3
NP1=N+1
NP5=N/2.-1.
NP6=N/2.+1.
NP4=N-2
NP2=N-1
NP3=N+2

FLOW PROFILE
READ(1,300)((S(I,J),I=3,NP2),J=4,NP2)
DO 53 J=1,NP3
T(J)=SIN((J-3.)*TD)
TT(J)=COS((J-3.)*TD)
S(2,J)=0.
S(N,J)=(EXP(RD*NP4))*T(J)-CD*(1.-(J-3.)*TD/3.141615)/2.
S(NP3,J)=(EXP(RD*N))*T(J)-CD*(1.-(J-3.)*TD/3.141615)/2.
S(NP1,J)=(EXP(RD*NP2))*T(J)-CD*(1.-(J-3.)*TD/3.141615)/2.
53 S(1,J)=0.0
DO 54 I=2,NP3
S(I,N)=0.0
S(I,3)=0.0
S(I,NP3)=-S(I,NP4)
S(I,NP1)=-S(I,NP2)
S(I,2)=-S(I,4)
54 S(I,1)=-S(I,5)
WRITE(3,205)
DO 10 I=1,NP3
10 R(I)=EXP(RD*(I-2.))
WRITE(3,204)
WRITE(3,301)(R(I),I=1,NP3)
DO 21 I=3,N
DO 21 J=3,N
UT(I,J)=-R.*(S(I+1,J)-S(I-1,J))-(S(I+2,J)-S(I-2,J)))/(RD*R(I)*12)
21 UR(I,J)=R.*(S(I,J+1)-S(I,J-1))-(S(I,J+2)-S(I,J-2)))/(TD*R(I)*12.)
WRITE(3,208)
WRITE(3,209)

IGN DENSITY PROFILE
BOUNDARY CONDITIONS
DO 2 J=1,NP3
NI(1,J)=0.0
NI(2,J)=0.0

```



```

61 NI(I,J)=((1.-QQ(I,J))*NI(I,J-1)*((3.*QQ(I,J)-1.)*QQ(I,J)+2.)
9+NI(I+2,J-1)*(QQ(I,J)-1.)*QQ(I,J)-NI(I-1,J-1)*(QQ(I,J)**2.))/2.
3+NI(I+1,J-1)*QQ(I,J)*(4.+QQ(I,J)*(-5.+3.*QQ(I,J)))/2.)
1*(CO(I,J)/(CO(I,J)+DQ(I) ))+(NI(I+1,J)+NI(I-1,J))*U+(NI(I,
2J+1)+NI(I,J-1))*V*(DQ(I)/(((CO(I,J) )+DQ(I))*2.*(U+V)))
3+((NI(I+1,J)-NI(I-1,J))*F/PD)*(1./((CO(I,J)+DQ(I))*2.*R(I)))
GO TO 90
71 IF(UT(I,J)-0.0)73,85,75
73 IF(QI(I,J)-1.0)74,79,79
74 NI(I,J)=((1.-Q(I,J))*NI(I-1,J)*((3.*Q(I,J)-1.)*Q(I,J)+2.)
9+NI(I-1,J+2)*Q(I,J)*(Q(I,J)-1.)*NI(I-1,J-1)*(Q(I,J)**2.))/2.
4+Q(I,J)*(NI(I-1,J+1)*(4.+Q(I,J)*(-5.+3.*Q(I,J)))/2.)
1*(CO(I,J)/(CO(I,J)+DQ(I)))+(NI(I+1,J)+NI(I-1,J))*U+(NI(I,J+1)+
2*NI(I,J-1))*V*(DQ(I)/((CO(I,J)+DQ(I))*2.*(U+V)))
3+((NI(I+1,J)-NI(I-1,J))*F/RD)*(1./((CO(I,J)+DQ(I))*2.*R(I)))
GO TO 90
79 NI(I,J)=((1.-QQ(I,J))*NI(I,J+1)*((3.*QQ(I,J)-1.)*QQ(I,J)+2.)
9+NI(I-2,J+1)*(QQ(I,J)-1.)*QQ(I,J)-NI(I+1,J+1)*(QQ(I,J)**2.))/2.
8+NI(I-1,J+1)*QQ(I,J)*(4.+QQ(I,J)*(-5.+3.*QQ(I,J)))/2.)
1*(CO(I,J)/(CO(I,J)+DQ(I) ))+(NI(I+1,J)+NI(I-1,J))*U+(NI(I,
2J+1)+NI(I,J-1))*V*(DQ(I)/(((CO(I,J) )+DQ(I))*2.*(U+V)))
3+((NI(I+1,J)-NI(I-1,J))*F/RD)*(1./((CO(I,J)+DQ(I))*2.*R(I)))
GO TO 90
85 NI(I,J)=NI(I-1,J)
1*(CO(I,J)/(CO(I,J)+DQ(I) ))+(NI(I+1,J)+NI(I-1,J))*U+(NI(I,
2J+1)+NI(I,J-1))*V*(DQ(I)/(((CO(I,J) )+DQ(I))*2.*(U+V)))
3+((NI(I+1,J)-NI(I-1,J))*F/RD)*(1./((CO(I,J)+DQ(I))*2.*R(I)))
GO TO 90
75 IF(QI(I,J)-1.0)82,83,83
82 NI(I,J)=((1.-Q(I,J))*NI(I-1,J)*((3.*Q(I,J)-1.)*Q(I,J)+2.)
9+NI(I-1,J-2)*Q(I,J)*(Q(I,J)-1.)*NI(I-1,J+1)*(Q(I,J)**2.))/2.
5+Q(I,J)*(NI(I-1,J-1)*(4.+Q(I,J)*(-5.+3.*Q(I,J)))/2.)
1*(CO(I,J)/(CO(I,J)+DQ(I)))+(NI(I+1,J)+NI(I-1,J))*U+(NI(I,J+1)+
2*NI(I,J-1))*V*(DQ(I)/((CO(I,J)+DQ(I))*2.*(U+V)))
3+((NI(I+1,J)-NI(I-1,J))*F/RD)*(1./((CO(I,J)+DQ(I))*2.*R(I)))
GO TO 90
83 NI(I,J)=((1.-QQ(I,J))*NI(I,J-1)*((3.*QQ(I,J)-1.)*QQ(I,J)+2.)
9+NI(I-2,J-1)*(QQ(I,J)-1.)*QQ(I,J)-NI(I+1,J-1)*(QQ(I,J)**2.))/2.
8+NI(I-1,J-1)*QQ(I,J)*(4.+QQ(I,J)*(-5.+3.*QQ(I,J)))/2.)
1*(CO(I,J)/(CO(I,J)+DQ(I) ))+(NI(I+1,J)+NI(I-1,J))*U+(NI(I,
2J+1)+NI(I,J-1))*V*(DQ(I)/(((CO(I,J) )+DQ(I))*2.*(U+V)))
3+((NI(I+1,J)-NI(I-1,J))*F/RD)*(1./((CO(I,J)+DQ(I))*2.*R(I)))
90 CONTINUE
4 EPS=EPS+ABS(NI(I,J)-HOLDT)
IF(EPS.LE.EPSMAX)GO TO 6
IF(ITER-ITMAX)3,3,8
6 WRITE (3,201) ITER
DO 7 I=3,N
7 WRITE (3,501)(NI(I,J),J=3,N )
GO TO 91
8 WRITE (3,203)
DO 9 I=1,NP3
9 WRITE (3,301)(NI(I,J),J=1,NP3)
91 WRITE (3,210)

```

CURRENT

LOCAL CURRENT

```
DO 51 J=3,N
```

```
51 PJ(J)=(32.*NI(3,J)-12.*NI(4,J)+NI(6,J))/(12.*RD)
WRITE (3,206)
WRITE (3,501)(PJ(J),J=3,N)
```

TOTAL CURRENT

```
PI1=0.0
```

```
DO 50 J=4,NP2,2
```

```
50 PI1=PI1+TD*(PJ(J-1)+4.*PJ(J)+PJ(J+1))/3.
WRITE (3,502)PI1
NPF=(N-3.)/2.
```

```
PI2=0.
```

```
DO 48 I=2,NP3,2
```

```
48 PI2=PI2+TD*2.*(PJ(2*I-1)+4.*PJ(2*I+1)+PJ(2*I+3)) /3.
WRITE (3,502)PI2
WRITE (3,207)
```

```
PIC=(16.*PI1 -PI2 )/15.
```

```
WRITE (3,500)PIC,PI1,PI2
```

```
GO TO 1
```

```
201 FORMAT(45HCONVERGENCE CONDITION HAS BEEN REACHED AFTER,13,10HITER
```

IATIONS)
203 FORMAT(15HNO CONVERGENCE)
204 FORMAT(9HDI STENCE)
205 FORMAT(16H0STEARM FUNCTION)
206 FORMAT(5H0FLUX)
207 FORMAT(14H0PROBE CURRENT)
208 FORMAT(4H0 UT)
209 FORMAT(4H0 UR)
210 FORMAT(4H0 NI)
220 FORMAT(4H0 EE)
300 FORMAT(6E13.6)
500 FORMAT(F10.6,F10.6,F10.6)
301 FORMAT(12F10.5/12F10.5/12F10.5/12F10.5/12F10.5/SF10.5/)
501 FORMAT(11E12.5/11F12.5/11E12.5/11E12.5/11E12.5/6E12.5/)
502 FORMAT(F10.6)
215 FORMAT(4H0 RE)
504 FORMAT(F10.3)
STOP
END

SENTRY

***** THIS IS END OF JOB *****

TABLE I Choices of $\Delta\theta, \Delta s$ and r_b for various Reynolds numbers.

	Re	$\Delta\theta$	Δs	r_b
Sphere	0.1	$\pi/30$	0.06	122
	0.5,1	$\pi/30$	0.06	54
	5,10	$\pi/30$	0.06	38
	20~60	$\pi/60$	0.03	38
Cylinder	0.1~1	$\pi/60$	$\pi/60$	58
	2	$\pi/40$	$\pi/40$	30
	5~40	$\pi/60$	$\pi/60$	30
	70~100	$\pi/40$	$\pi/40$	30

TABLE II Cylindrical Probe : Computed values of probe current per unit length for values of Reynolds number from 0.1 to 100. In some entries, values of exponents are omitted, and are implied by exponent values in preceding rows.

	Re=0.1		Re=0.4				
	$\phi_p / e \ln \Delta$	Sc=10 ⁴	10 ³	10 ⁵	10 ⁴	10 ³	10 ²
10	9.901	9.964	10.814	9.967	9.929	9.974	
8	7.950	7.979	9.298	8.140	7.949	7.998	
6	6.052	5.975	7.889	6.422	5.996	6.001	
4	4.294	4.010	6.606	4.876	4.163	3.989	
2	2.797	2.220	5.460	3.561	2.601	2.142	
0	1.671	9.559x10 ¹	4.460	2.480	1.451	8.381x10 ¹	
-2	9.377x10 ¹	3.320	3.602	1.727	7.588x10 ¹	2.511	
-4	5.115	1.076	2.879	1.169	3.844	6.530x10 ²	
-6	2.775	2.903x10 ²	2.277	7.856x10 ¹	1.941	1.509	
-8	1.505	7.472x10 ³	1.779	5.265	9.776x10 ²	3.079	
-10	5.171x10 ²	1.766	1.367	3.506	4.900		
-12	4.479		1.025	2.316	2.463		

$\Phi_p / \ln \Lambda$	Re=1			Re=5	
	$Sc=10^4$	10^3	10^2	10^3	10^2
10	10.173	9.905	9.967	9.999	9.977
8	8.496	7.964	7.979	8.182	7.889
6	6.906	6.099	5.977	6.626	5.982
4	5.499	4.404	4.025	5.263	4.274
2	4.282	2.981	2.311	4.108	2.877
0	3.272	1.905	1.102	3.160	1.845
-2	2.459	1.171	4.601×10^1	2.401	1.151
-4	1.822	7.097×10^1	1.783	1.804	7.123×10^1
-6	1.334	4.314	7.012×10^2	1.342	4.426
-8	9.624×10^1	2.643	2.588	9.846×10^1	2.769
-10	6.801	1.631	9.139×10^3	7.071	1.741
-12	4.645	1.018	3.126	4.906	

$\Phi_p / \ln \Lambda$	Re=7				Re=10		
	$Sc=10^4$	10^3	10^2	10	10^3	10^2	10
10	11.513	9.905	9.810		9.832	9.669	9.940
8	10.468	8.281	7.842	7.970	8.368	7.752	7.925
6	9.567	6.824	5.992	5.951	7.059	5.990	5.909
4	8.624	6.824	4.363	4.002	5.908	4.464	4.012
2	7.818	5.549	3.039	2.344	4.910	3.225	2.438
0	7.083	3.550	2.046	1.202	4.050	2.290	1.335
-2	6.415	2.800	1.350	5.708×10^1	3.332	1.584	7.082×10^1
-4	5.810	2.191	8.845×10^1	2.650	2.630*	1.093	3.750*
-6	5.264	1.698	5.791	1.217	2.209	7.502×10^1	1.911
-8	4.771	1.300	3.796	5.484×10^2	1.777	5.115	9.878×10^2
-10	4.326	9.772×10^1	2.486	2.414	1.414	3.450	5.071

$\phi_p / e \ln \Delta$	Re=20				Re=40			
	$Sc=10^3$	10^2	10	1	10^3	10^2	10	1
10	10.194	9.303	9.773	9.972	11.912	9.482	9.488	9.927
8	9.061	7.606	7.747	7.982	11.003	8.022	7.555	7.912
6	8.033	6.096	5.800	5.961	10.153	6.720	5.785	5.980*
4	7.180*	4.820*	4.063	3.948	9.362	5.580	4.260	3.941
2	6.271	3.721	2.670	2.172	8.630	4.568*	3.033	2.317
0	5.527	2.849	1.674	9.703×10^1	7.954	3.768	2.107	1.214
-2	4.865	2.160	1.029	3.785	7.334	3.071	1.444	6.016×10^1
-4	4.277	1.623	6.301×10^1	1.408	6.765	2.488	9.843	2.934
-6	3.785	1.206	3.870	$4.610 \times 10^{2*}$	6.244	2.005	6.684	1.385*
-8	3.295	8.843×10^1	2.383	1.496	5.769	1.602	4.518	6.366×10^2
-10	2.886	6.341	1.470	4.211	5.337	1.265	3.024	2.903

$\phi_p / e \ln \Delta$	Re=100			
	$Sc=10^2$	10	1	10^1
10	10.582	9.236	9.600	9.844
8	9.550	7.691	7.720	7.923
6	8.753	6.288	5.748	5.936
4	8.115	5.053	3.989	3.921
2	7.398	3.996	2.591	2.088
0	6.737	3.116	1.590	8.538×10^1
-2	6.135	2.402	9.433×10^1	2.931
-4	5.588	1.829	5.490	8.872×10^2
-6	5.093	1.374	3.115	2.302
-8	4.648	1.012	1.692	5.15×10^3
-10	4.249	7.225×10^1	8.620×10^2	1.050

TABLE III Spherical Probe : Computed values of probe current for values of Reynolds number from 5 to 60. In some entries, values of exponents are omitted, and are implied by exponent values in preceding rows.

ϕ_p/ϕ_s	Re=5			Re=20			
	Sc=10 ³	10 ²	10	10 ²	10	1	0
10	11.292	9.985		10.404	9.747		10.000
8	9.881	8.185		9.015	8.260		8.000
6	8.566	6.573	5.968	7.648	6.375	5.997	6.003
4	7.378 [*]	5.252	4.264	6.456	4.815	3.980	4.075
2	6.316	3.985	2.887	5.502	3.666	2.774	2.313
0	5.378	3.171	1.997	4.577	2.806	1.823	1.000
-2	4.651	2.266	1.263	3.780	2.087	1.186	3.130x10 ¹
-4	4.006	1.681	8.005x10 ¹	3.164	1.572	7.230x10 ¹	7.461x10 ²
-6	3.439	1.226	4.937	2.624	1.191	4.281	1.490
-8	2.944	8.796x10 ¹	2.981	2.190	8.970x10 ¹	2.489	2.683x10 ³
-10	2.513	6.202	1.775	1.834	4.548	1.401	4.536x10 ⁴

ϕ_p/ϕ_s	Re=40			Re=60			
	Sc=10 ²	10	1	10 ²	10	1	0
10	10.067	9.851		10.996	9.891		10.000
8	9.153	8.146		9.796	8.100		8.000
6	8.158	6.493	5.666	8.813	6.791	5.734	6.003
4	7.233	5.251	4.173	8.171	5.778	4.391	4.075
2	6.312	4.198	3.025	6.931	4.650	3.278	2.313
0	5.697	3.345	2.141	6.255	3.804	2.344	1.000
-2	4.815	2.488	1.415	5.508	2.960	1.638	3.130x10 ¹
-4	4.038	1.849	9.478x10 ¹	5.071	2.506	1.203	7.461x10 ²
-6	3.329	1.485	5.927	4.256	1.868	7.660x10 ¹	1.490
-8	2.649	1.091	3.603	3.726	1.415	5.110	2.683x10 ³
-10	2.227	7.345x10 ¹	2.146	3.243	1.082	3.314	4.536x10 ⁴

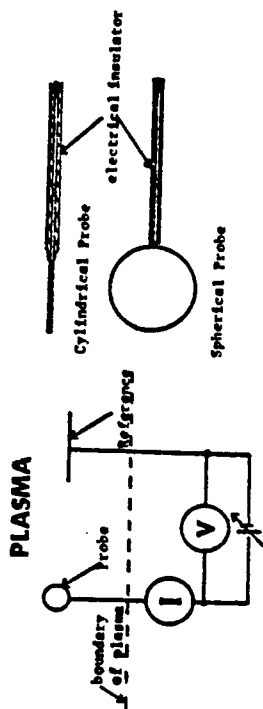


FIGURE 1.1 Probes and basic circuit

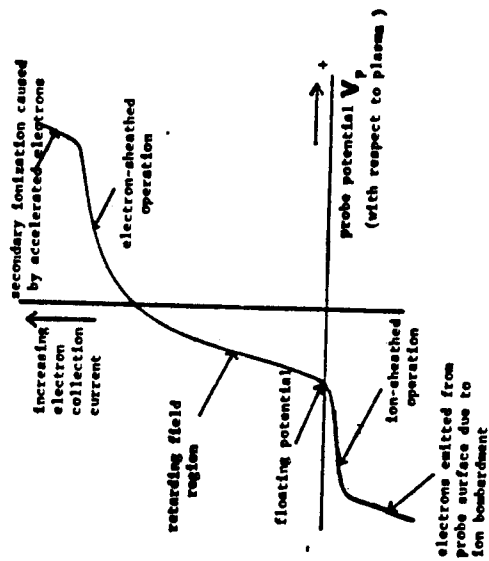


FIGURE 1.2 Complete electrostatic probe current-voltage characteristic. (after Laframboise 1966)

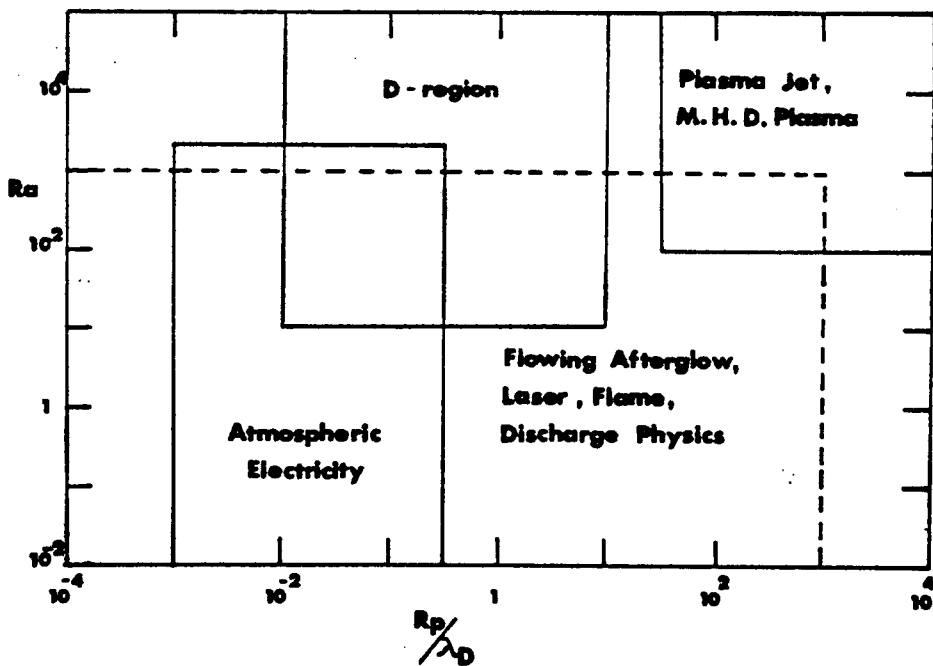


FIGURE 1.3 Approximate range of probe conditions for various continuum flowing plasmas. In all of these applications, typical Reynolds numbers range from 10^{-3} to 10^4 .

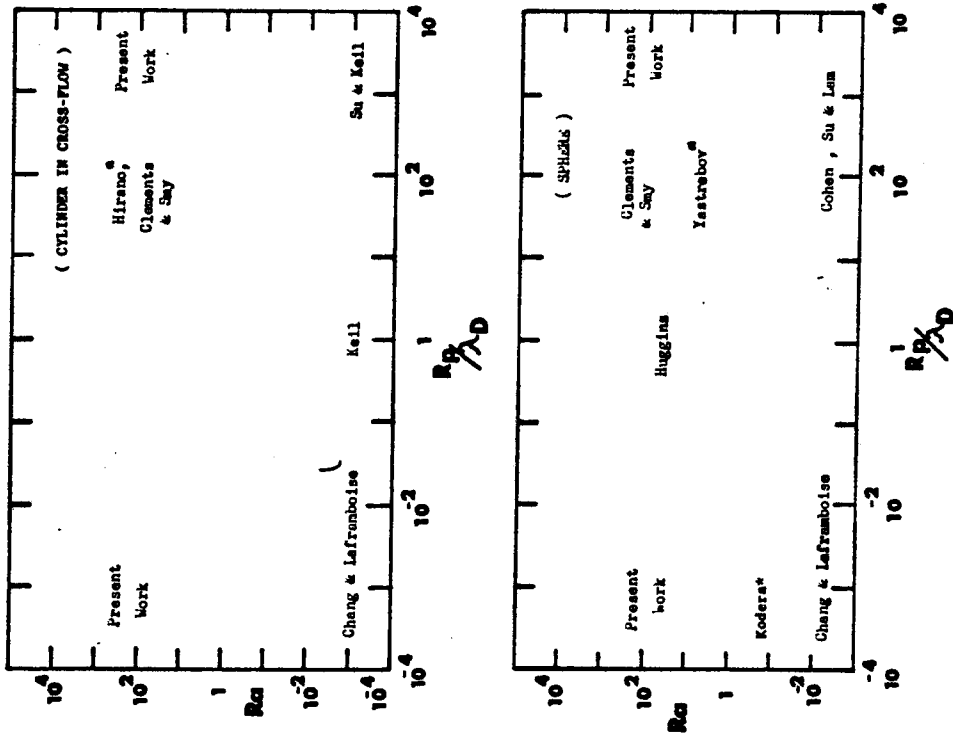


FIGURE 1.4 Summary of previous probe theory for flowing plasma.
 (a) Cylinder in cross-flow (b) Sphere. * stagnation point theory.

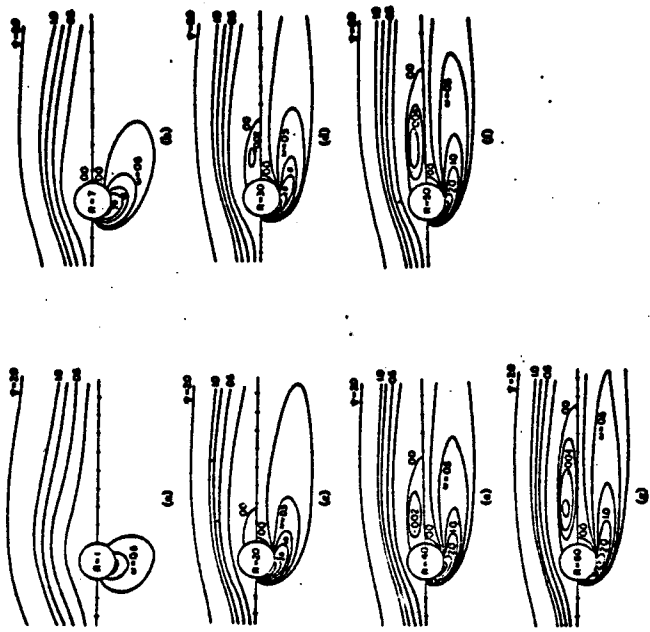


FIGURE 3.1 Streamlines $\Psi = \text{const.}$ and equi-vorticity lines $\omega = \text{const.}$ for steady flow past a circular cylinder. Values of the dimensionless stream function Ψ are shown for each streamline. (a) $Re=1$, (b) $Re=7$, (c) $Re=20$, (d) $Re=30$, (e) $Re=40$, (f) $Re=60$. (from Takami and Keller 1959)

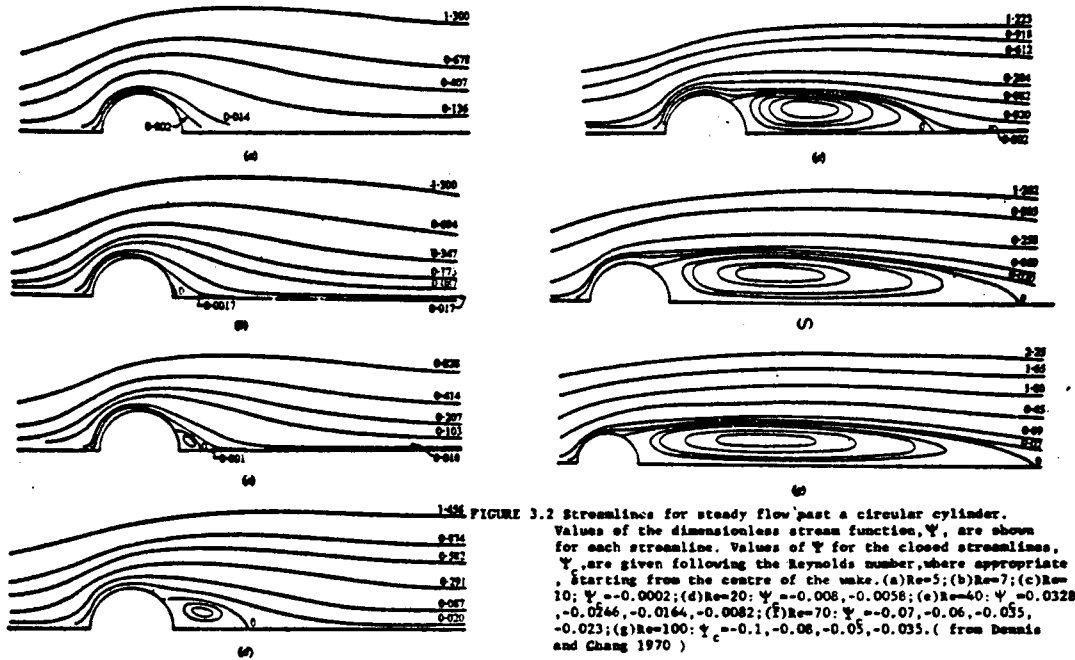


FIGURE 3.2 Streamlines for steady flow past a circular cylinder. Values of the dimensionless stream function, Ψ , are shown for each streamline. Values of Ψ for the closed streamlines, starting from the centre of the wake, are given following the Reynolds number, where appropriate. (a) $Re=5$; (b) $Re=7$; (c) $Re=10$; $\Psi = -0.0002$; (d) $Re=20$; $\Psi = -0.008, -0.0058$; (e) $Re=40$; $\Psi = -0.0328, -0.0264, -0.0164, -0.0082$; (f) $Re=70$; $\Psi = -0.07, -0.06, -0.055, -0.023$; (g) $Re=100$; $\Psi = -0.1, -0.08, -0.05, -0.035$. (from Dennis and Chang 1970)

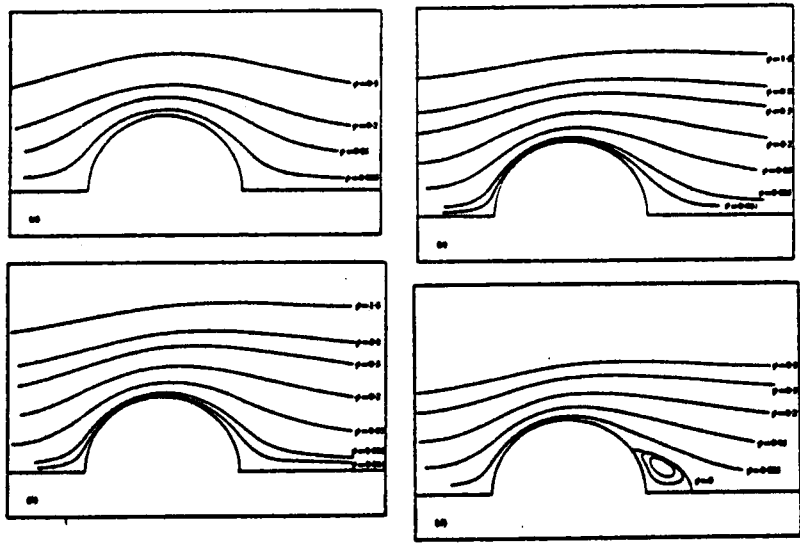


FIGURE 3.3 Streamlines for: (a) $Re=1$, (b) $Re=10$, (c) $Re=20$, (d) $Re=40$ (enclosed streamlines, starting from the centre, are $\Psi = -0.0003$ and $\Psi = -0.0001$). (from Dennis and Walker 1971, Dennis and Hudson 1973)

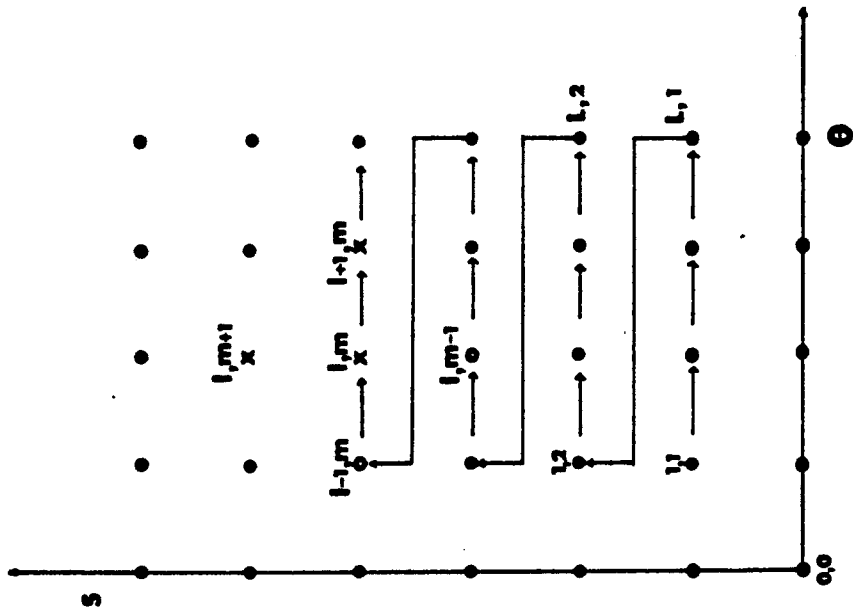


FIGURE 4.1 Identification of mesh point on a finite difference grid of LXM points and arrangement of grid for successive relaxation. Arrows show order of progression through the grid. The residual at $(1, 0)$ is computed using old guesses at the points indicated with x and new guesses at the circled points.

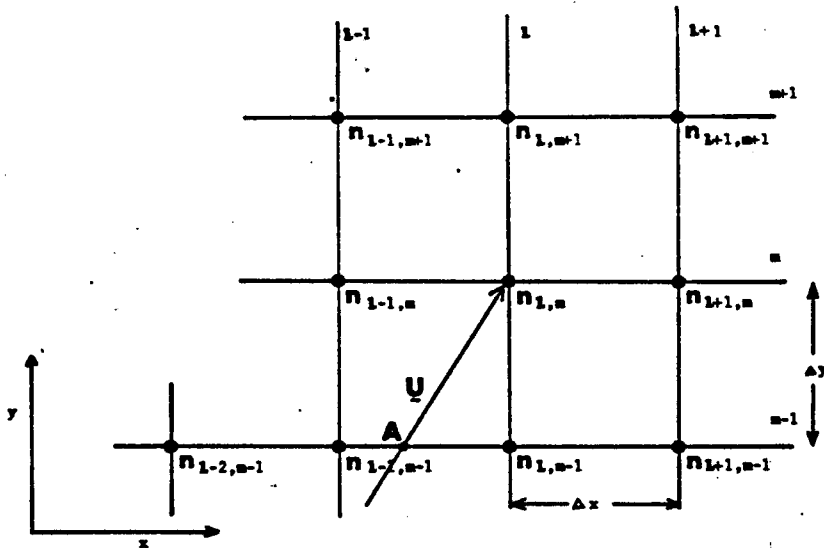


FIGURE 4.2 Grid structure and upwind difference methods.

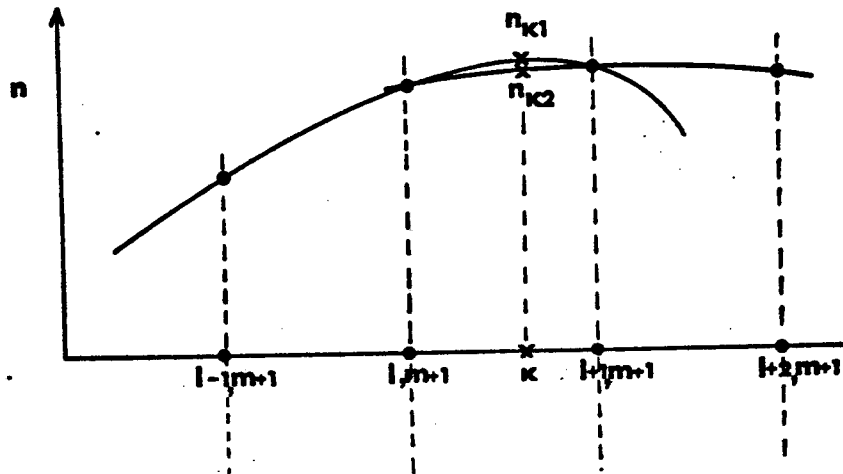


FIGURE 4.3 Interpolation procedure for higher order upwind difference methods.

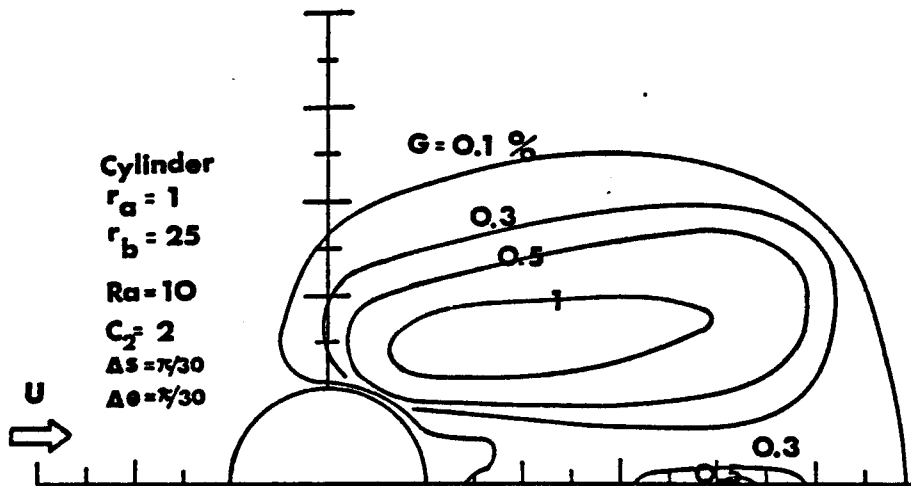


FIGURE 4.4 Contour map of relative error G between analytic solutions and numerical higher order upwind difference solutions. (a) cylinder (b) sphere.

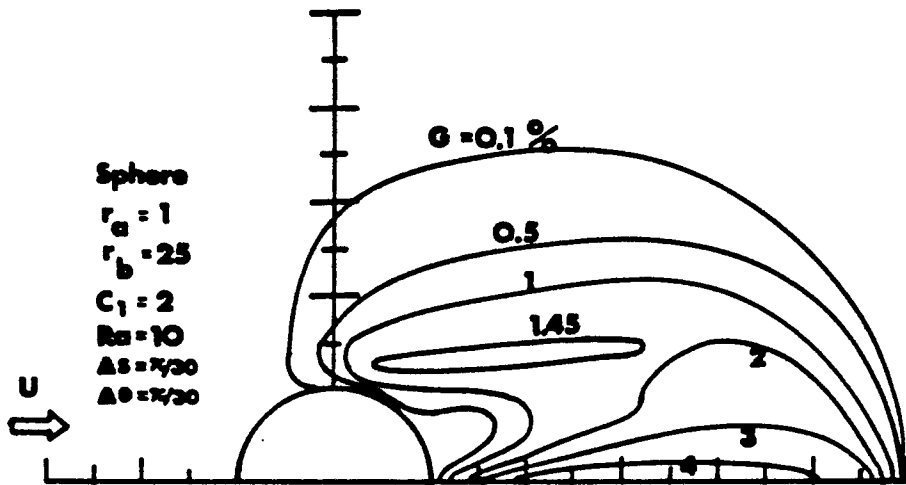


FIGURE 4.4b Contour map of relative error G between analytic solutions and numerical higher order upwind difference solutions.

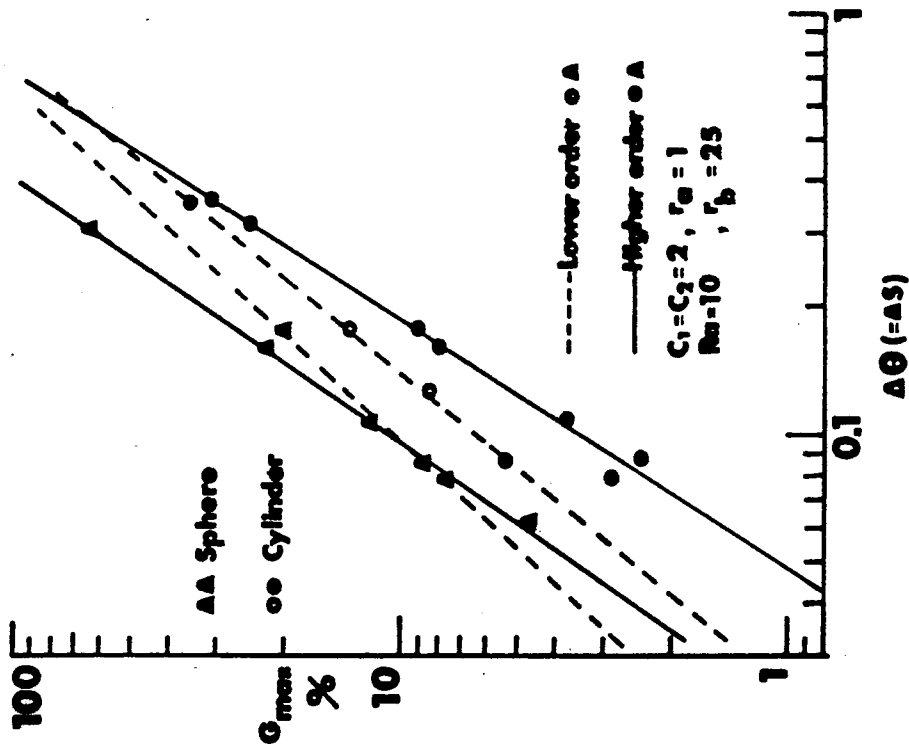


FIGURE 4.5 Maximum error vs grid size for both lower order and higher order upwind difference methods.

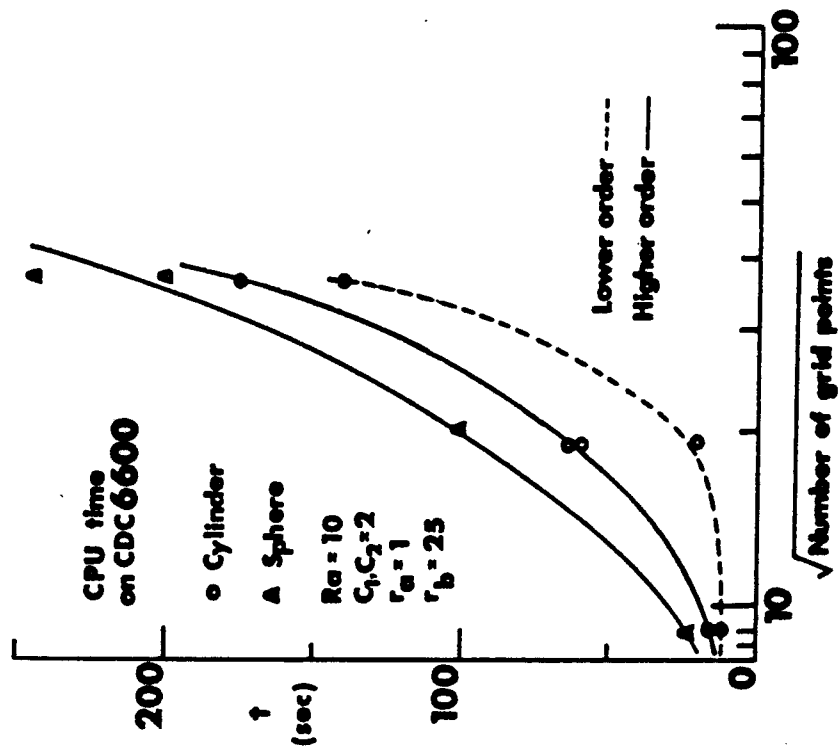


FIGURE 4.6 Computation time on CDC 6600 for upwind difference test problems.
 Time per iteration and cutoff condition are given in Sec. 4.13

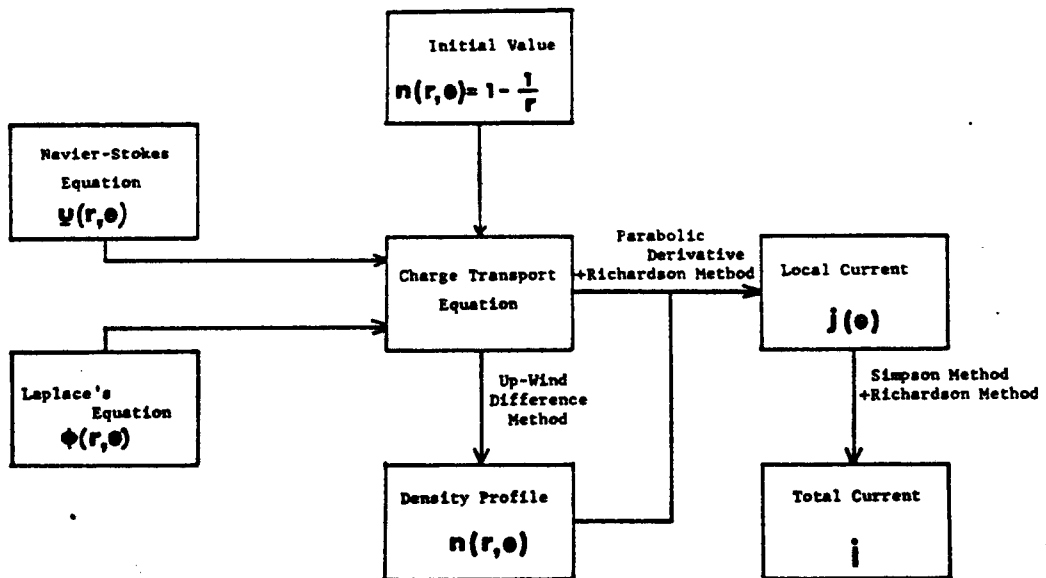


FIGURE 4.7 Block diagram of mathematical methods.

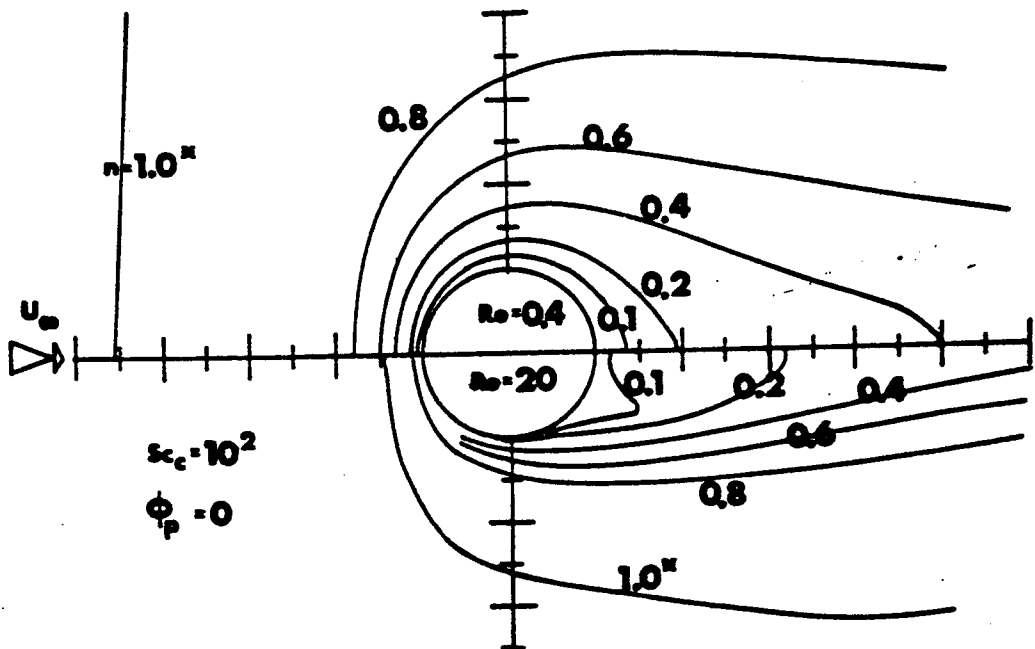


FIGURE 5.1 Charge density contour maps for cylinder in cross-flow
 (a) Comparison for flow without wake ($Re=0.4$) and flow with wake ($Re=20$) at space potential, $Sc_c=10^2$.
 * where we define $n=0.9999$ equal to 1.0 .

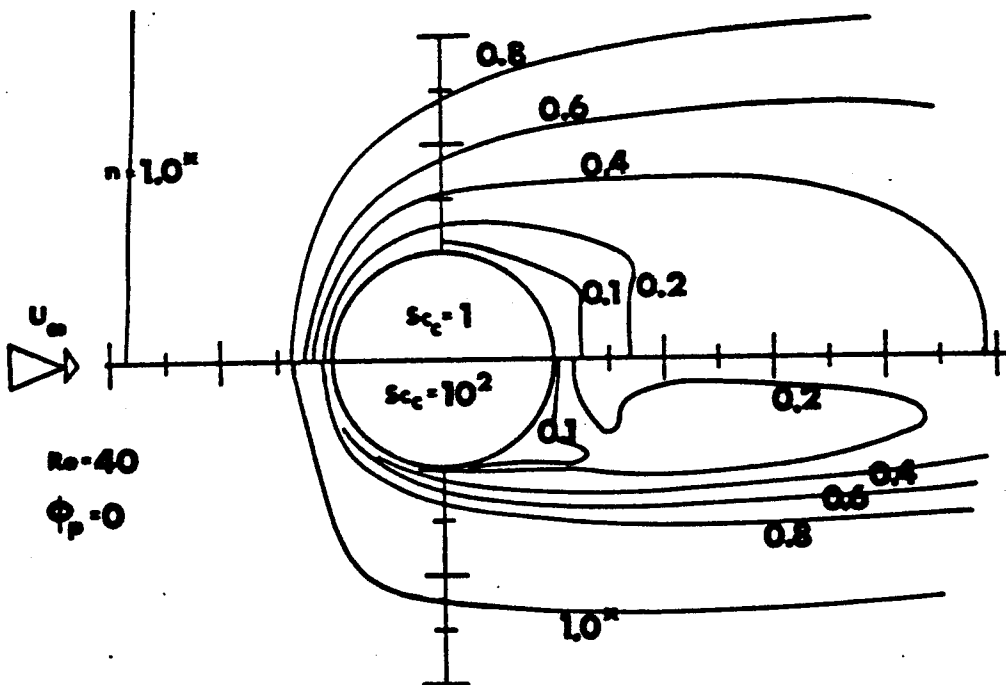


FIGURE 5.1b Comparison of charged particle Schmidt number effects on charge density at $Re=40$, space potential.

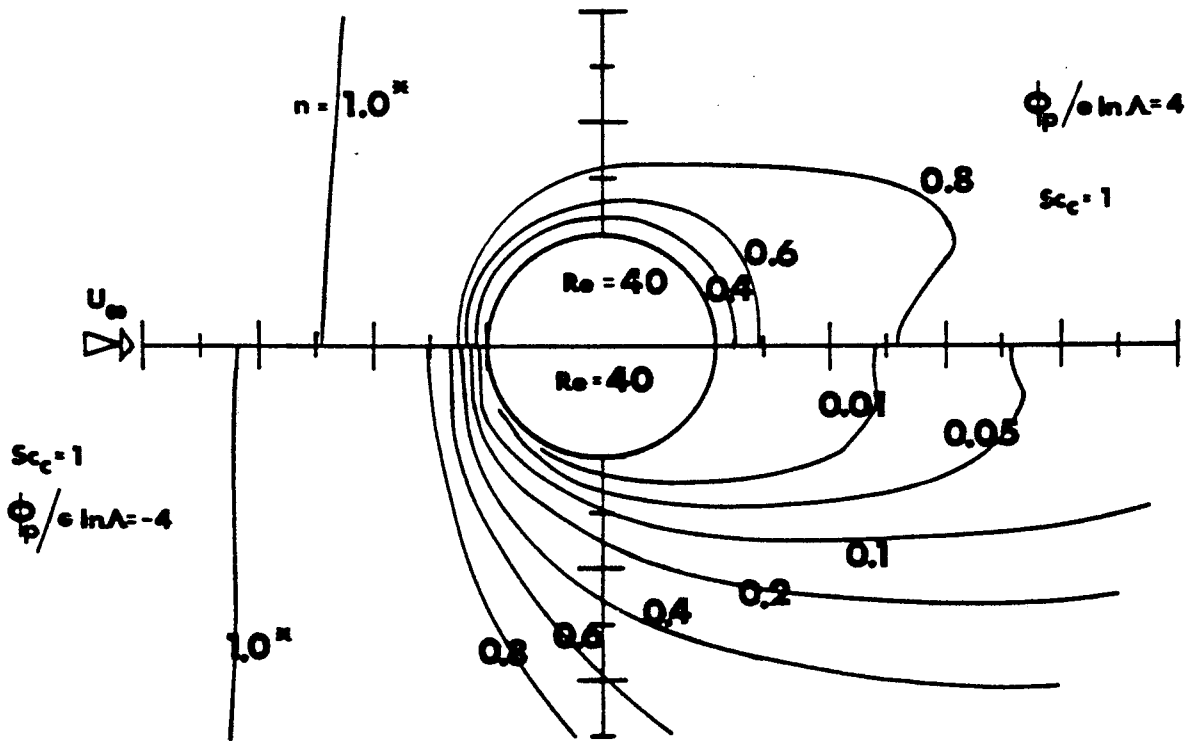


FIGURE 5.1c Comparison of surface potential effects on charge density for flow with wake, $Re=40, Sc_c=1$.

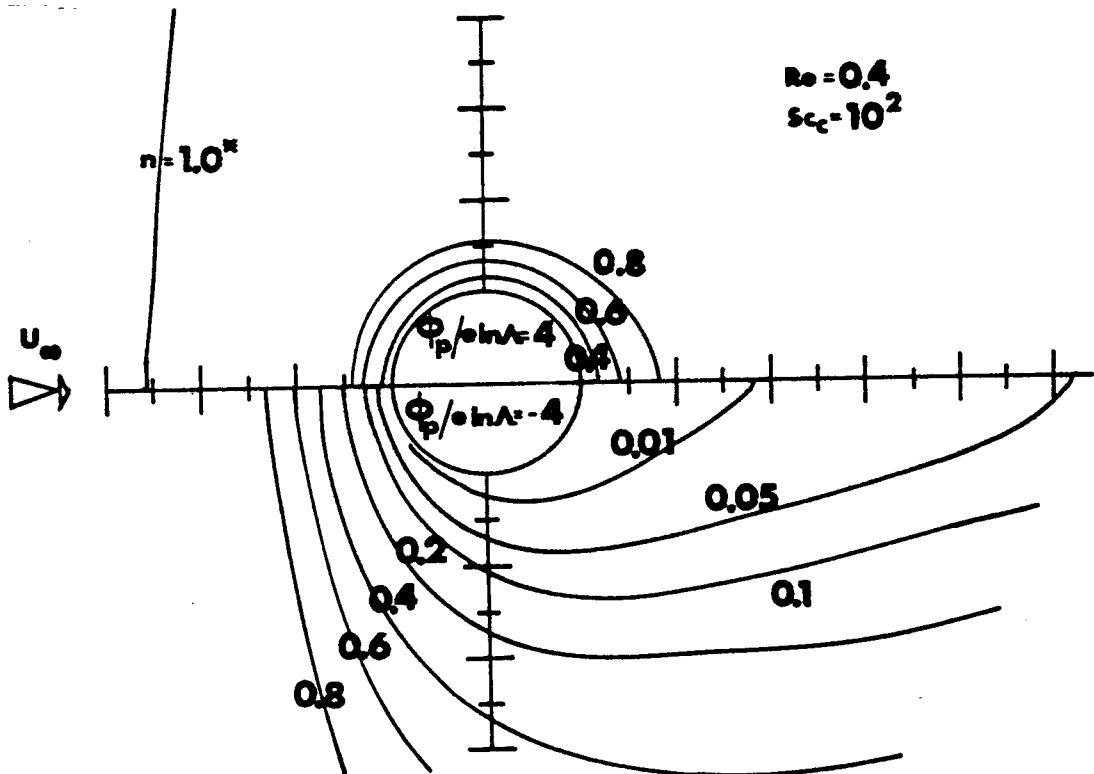


FIGURE 5.1d Comparison of surface potential effects on charge density for flow without wake, $Re=0.4, Sc_c=10^2$.

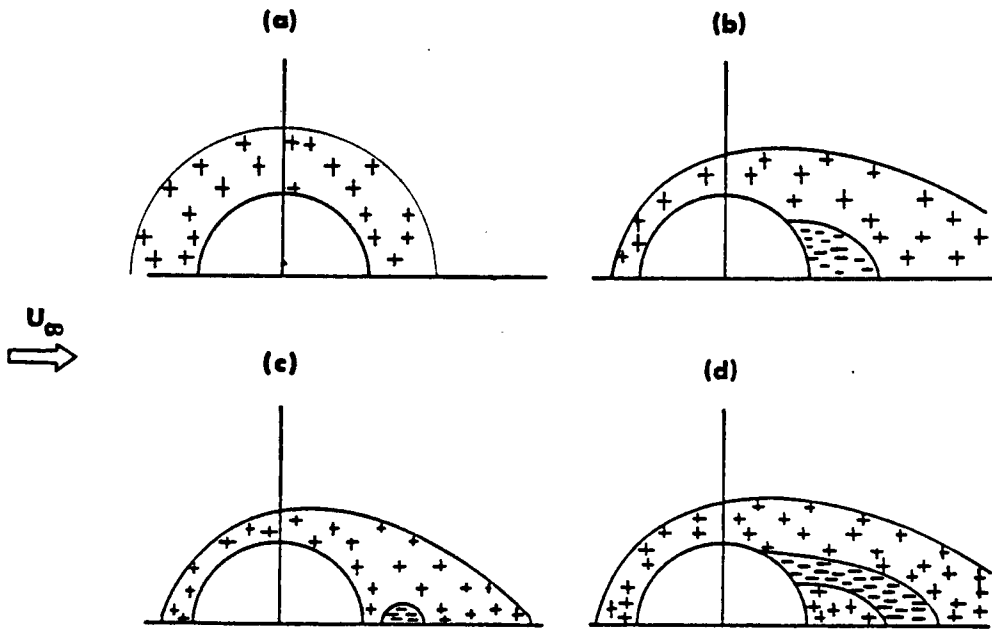


FIGURE 5.2 General appearance of net charge density ($n_+ - n_-$) contour map. (a) stationary case (b) flow without wake (c) (d) flow with wake (sphere $Re=20$, cylinder $Re=7$).

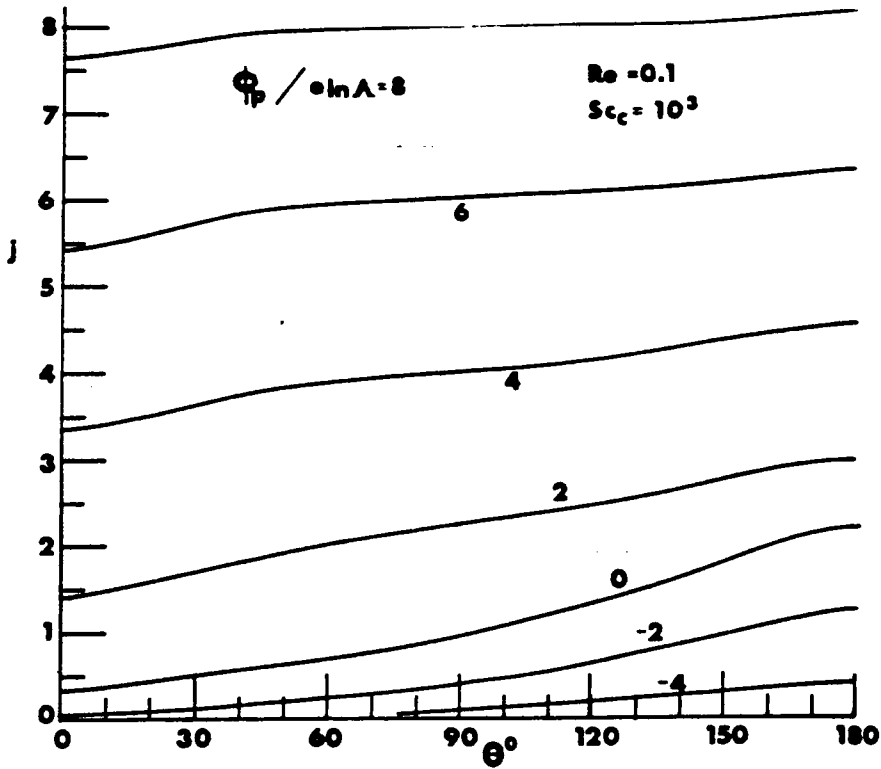


FIGURE 5.3 Angle dependence of local current to cylinder in cross-flow for various surface potentials. We define the rear stagnation point as $\theta=0$. (a) $Re=0.1, Sc_c=10^3$ (b) $Re=0.1, Sc_c=10^4$ (c) $Re=1, Sc_c=10^3$ (d) $Re=10, Sc_c=10$ (e) $Re=10, Sc_c=10^2$ (f) $Re=40, Sc_c=10$ (g) $Re=100, Sc_c=0.1$ (h) $Re=100, Sc_c=10$. Effects of wake are observed in Fig. 5.3(d)-(h) at the rear stagnation region.

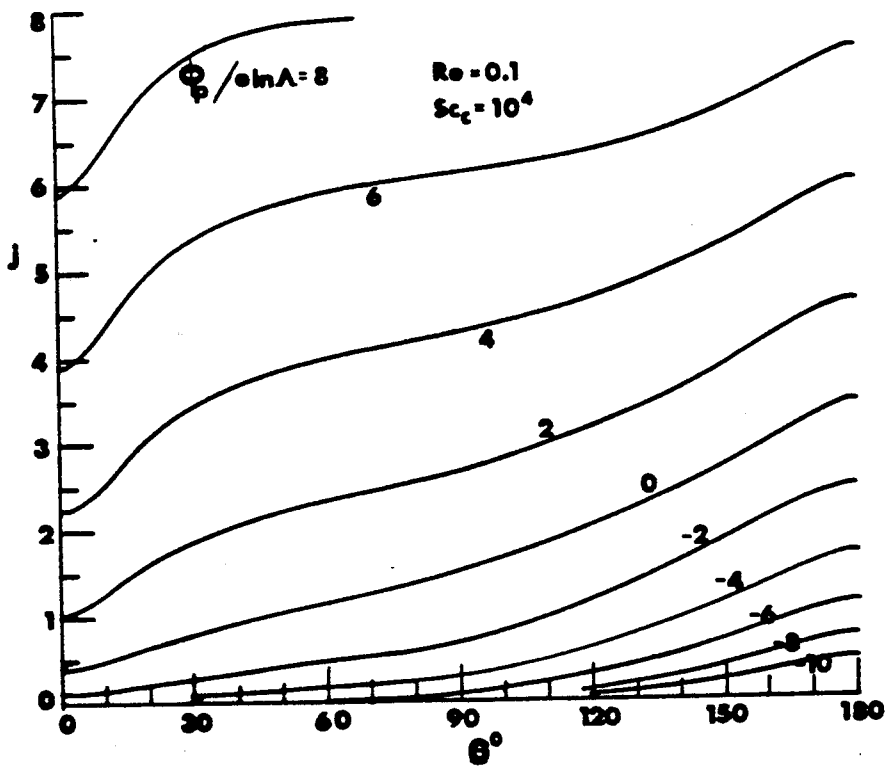


FIGURE 5.3b Angle dependence of local current for various surface potentials. $Re=0.1, Sc_c=10^4$.

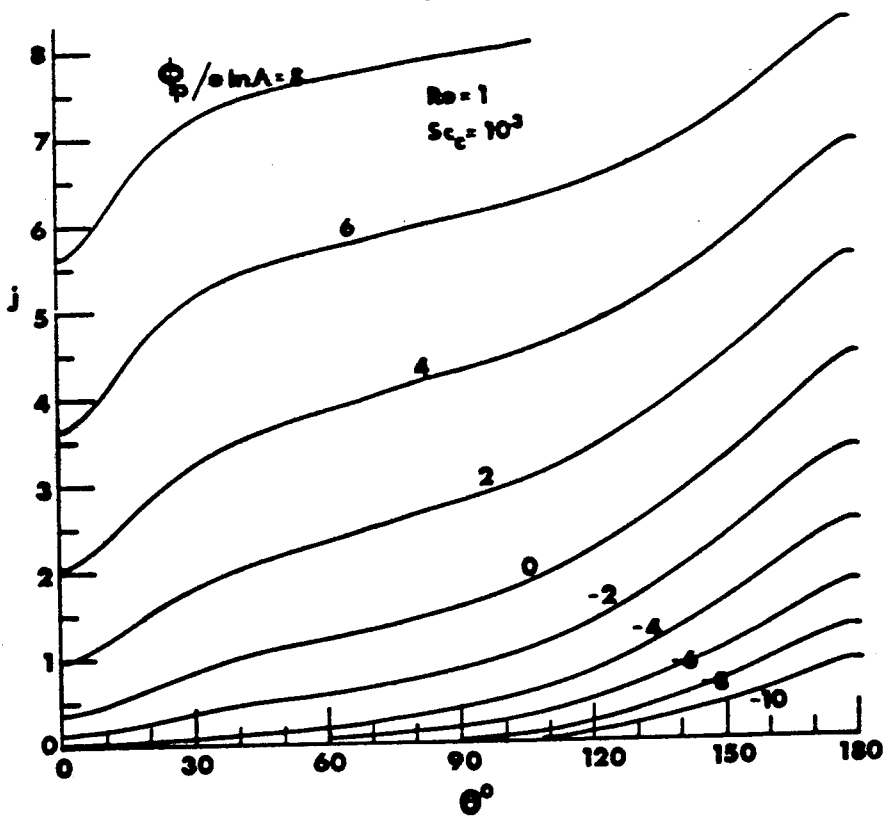


FIGURE 5.3c Angle dependence of local current for various surface potentials. $Re=1, Sc_c=10^3$.

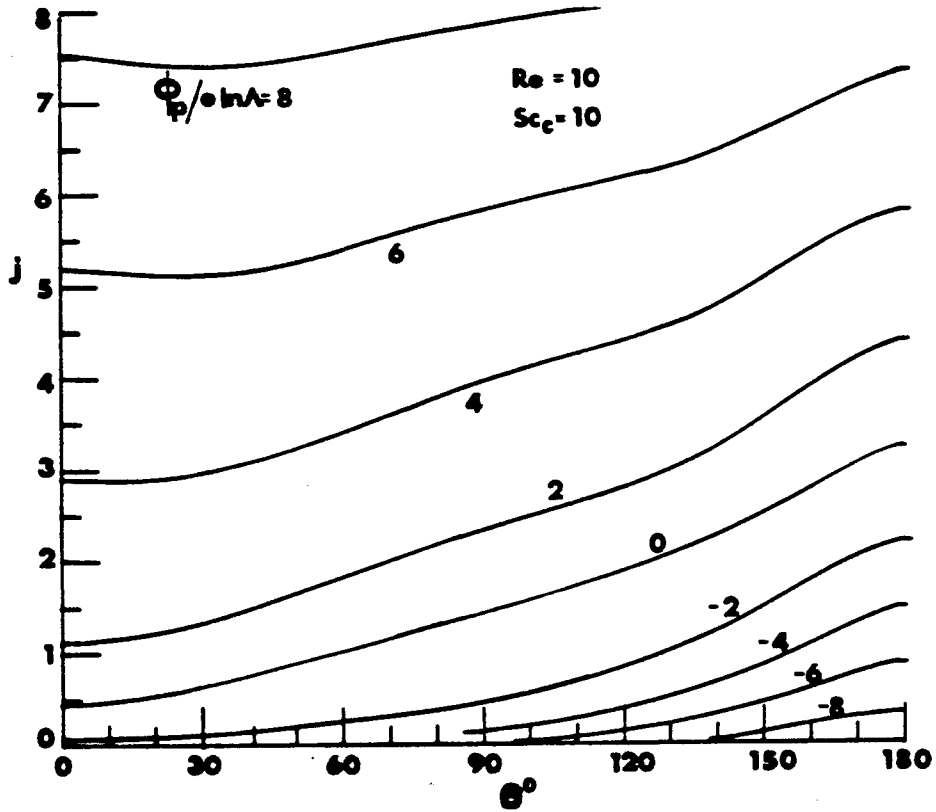


FIGURE 5.3d Angle dependence of local current for various surface potentials. $Re=10, Sc_c=10$.

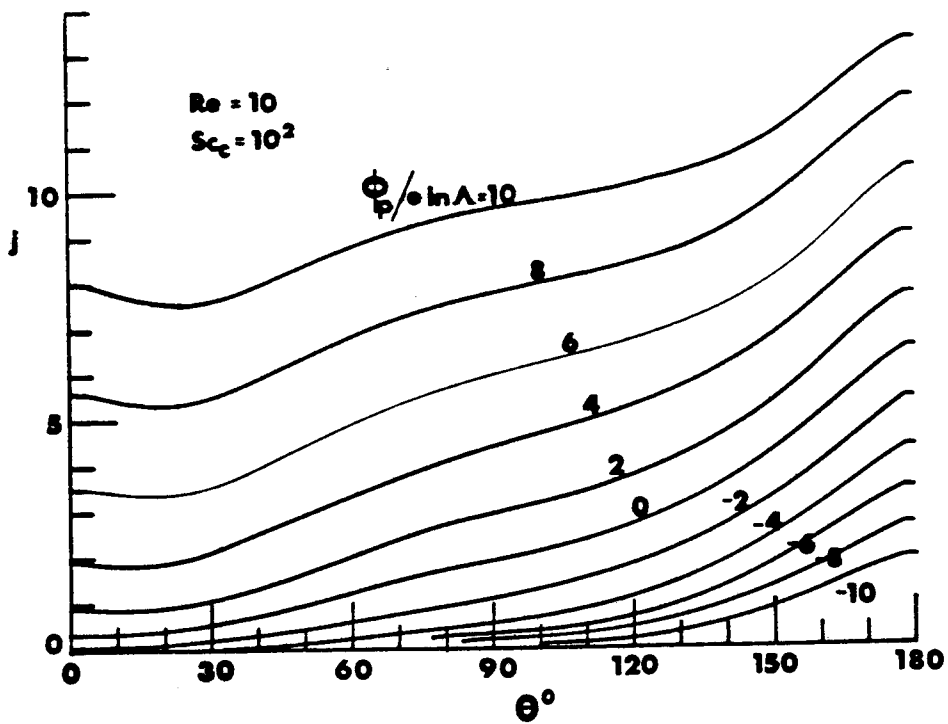


FIGURE 5.3e Angle dependence of local current for various surface potentials. $Re=10, Sc_c=10^2$.

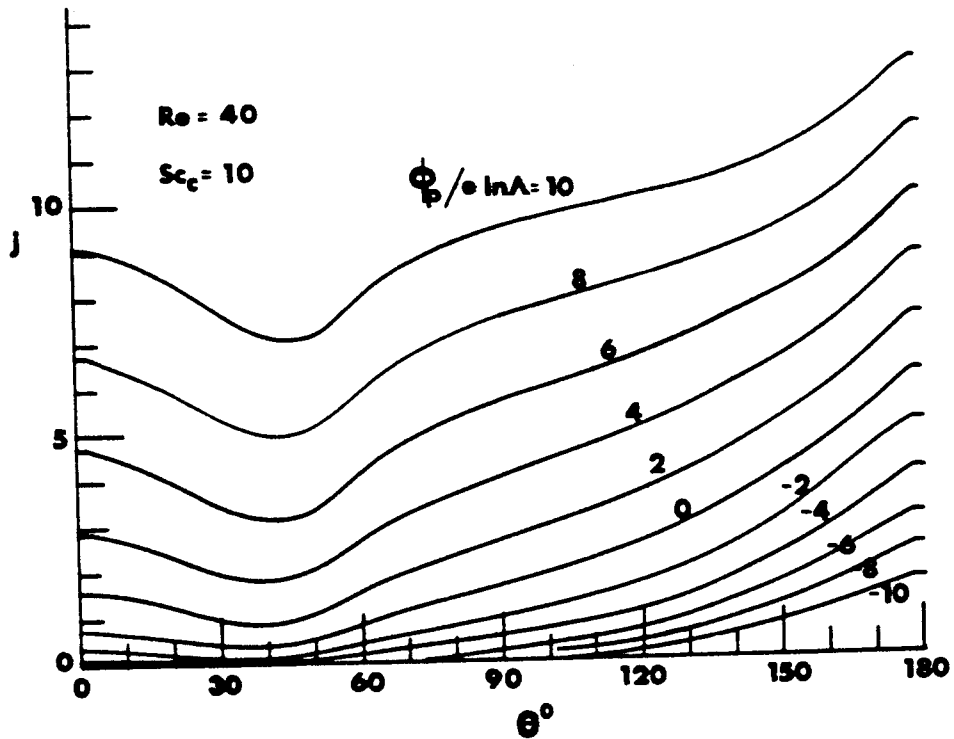


FIGURE 5.3f Angle dependence of local current for various surface potentials. $Re=40$, $Sc_c=10$.

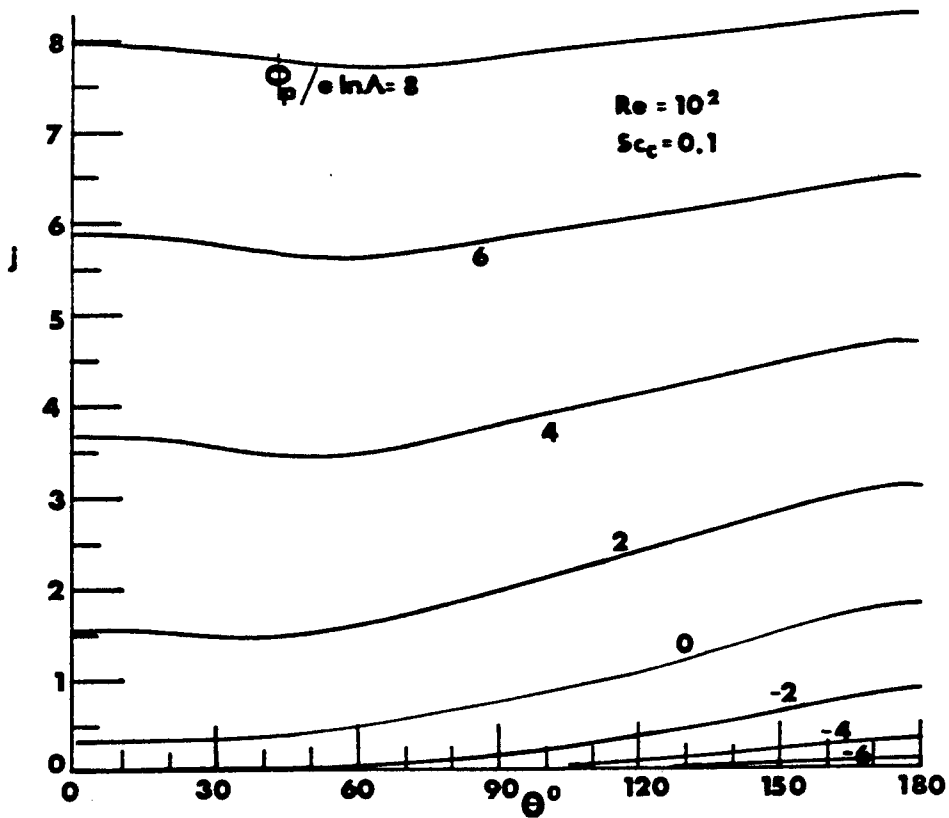


FIGURE 5.3g Angle dependence of local current for various surface potentials. $Re=100$, $Sc_c=0.1$.

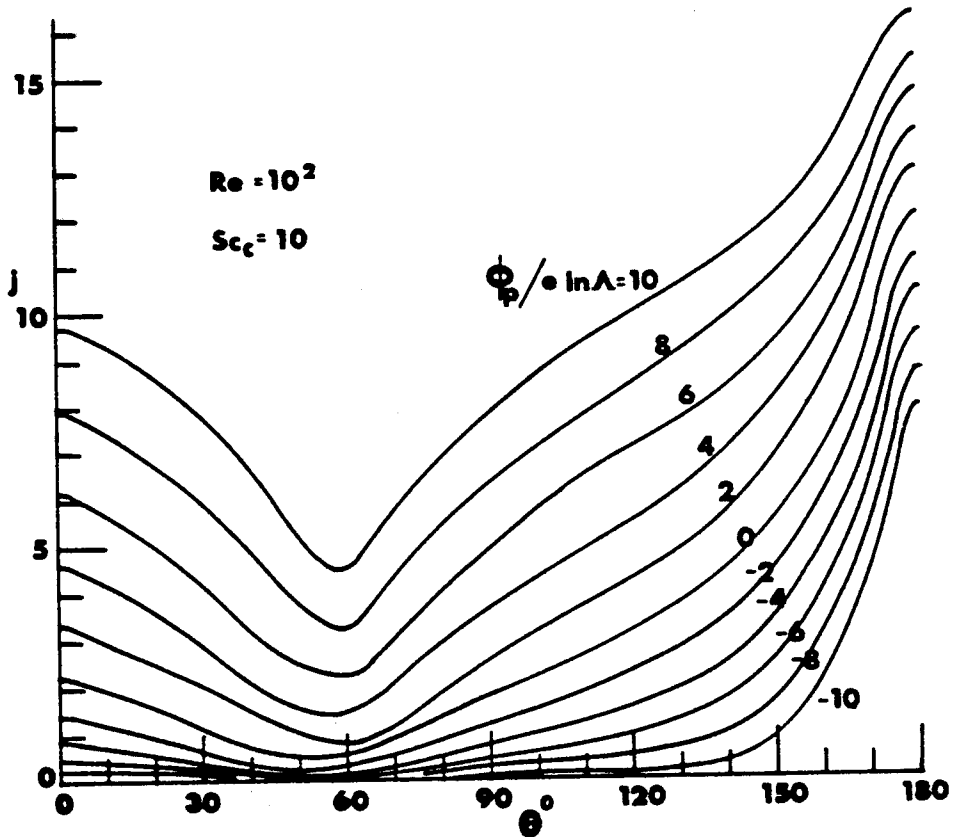


FIGURE 5.3h Angle dependence of local current for various surface potentials. $Re=100$, $Sc_c=10$.

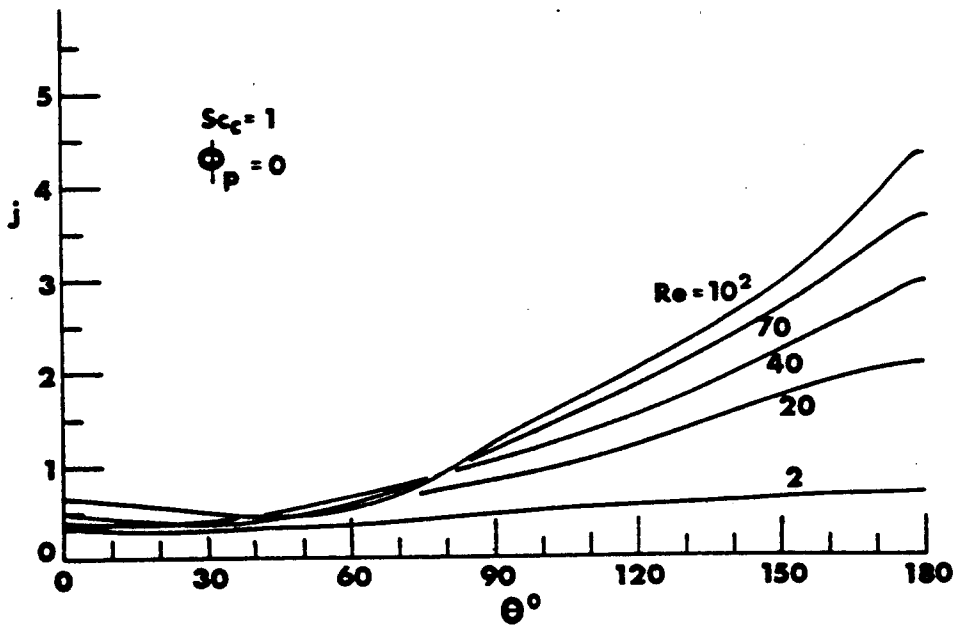


FIGURE 5.4 Angle dependence of local current to cylinder in cross-flow for various Reynolds numbers. (a) $Sc_c=1, \phi_p/e \ln \Lambda = 0$ (b) $Sc_c=1, \phi_p/e \ln \Lambda = 4$ (c) $Sc_c=1, \phi_p/e \ln \Lambda = -2$ (d) $Sc_c=10^2, \phi_p/e \ln \Lambda = 0$ (e) $Sc_c=10^2, \phi_p/e \ln \Lambda = 4$ (f) $Sc_c=10^2, \phi_p/e \ln \Lambda = -2$.

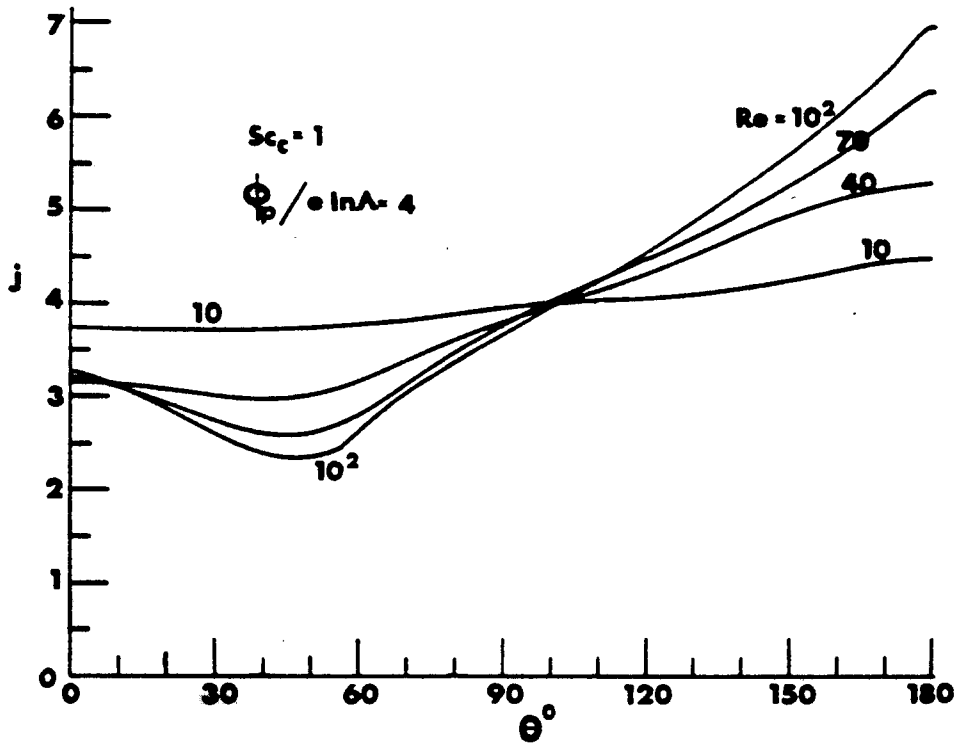


FIGURE 5.4b Angle dependence of local current for various Reynolds numbers. $Sc_c = 1$, $\phi_p / \epsilon \ln A = 4$.

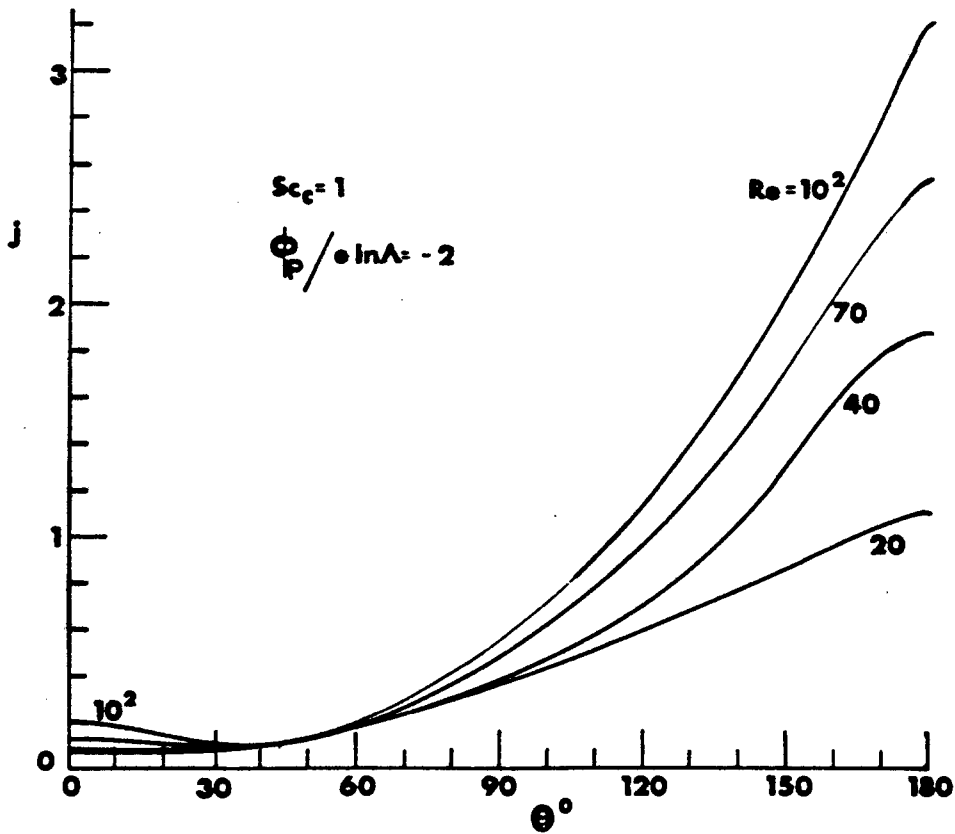


FIGURE 5.4c Angle dependence of local current for various Reynolds numbers. $Sc_c = 1$, $\phi_p / \epsilon \ln A = -2$.

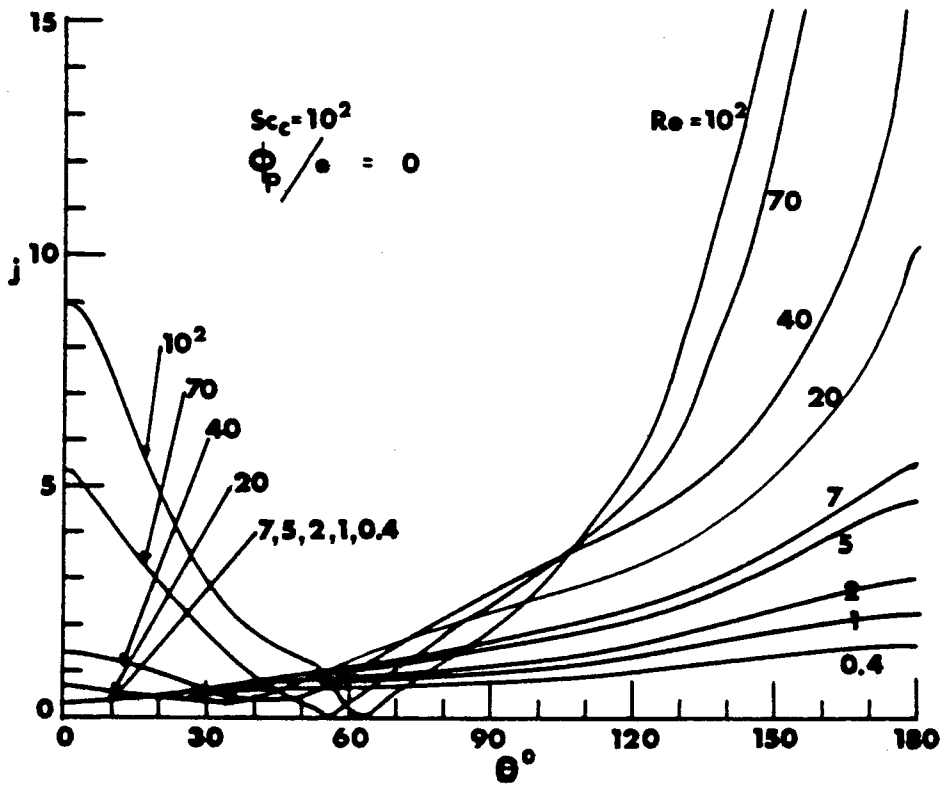


FIGURE 5.4d Angle dependence of local current for various Reynolds numbers. $Sc_c = 10^2$, $\phi_p/\epsilon = 0$.

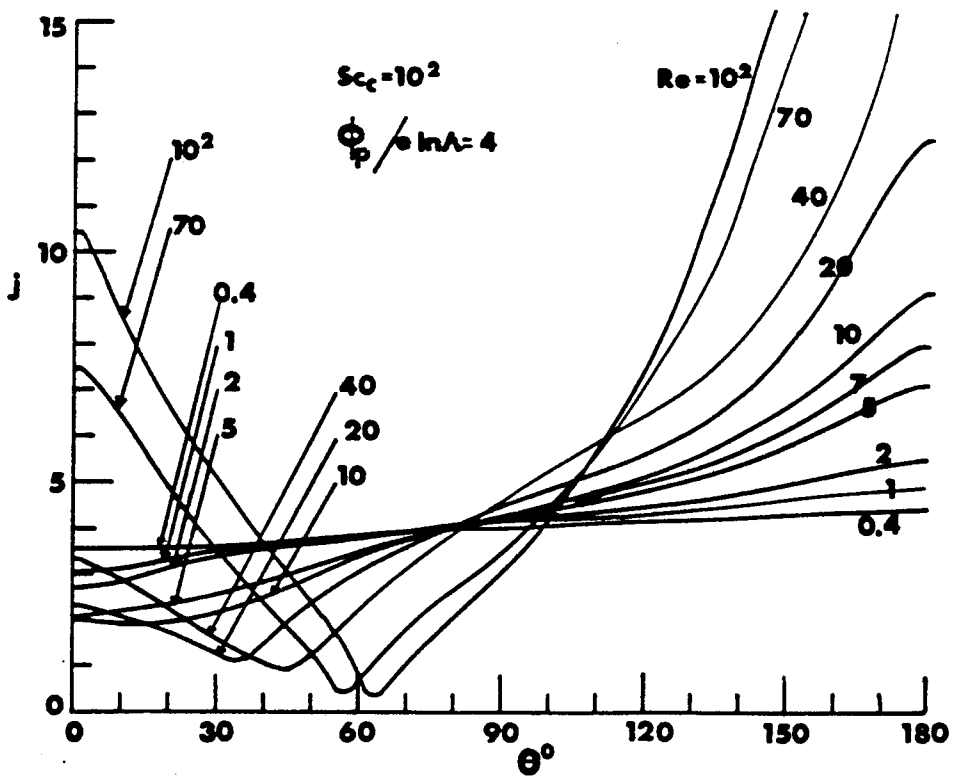


FIGURE 5.4e Angle dependence of local current for various Reynolds numbers. $Sc_c = 10^2$, $\phi_p/\epsilon \ln A = 4$.

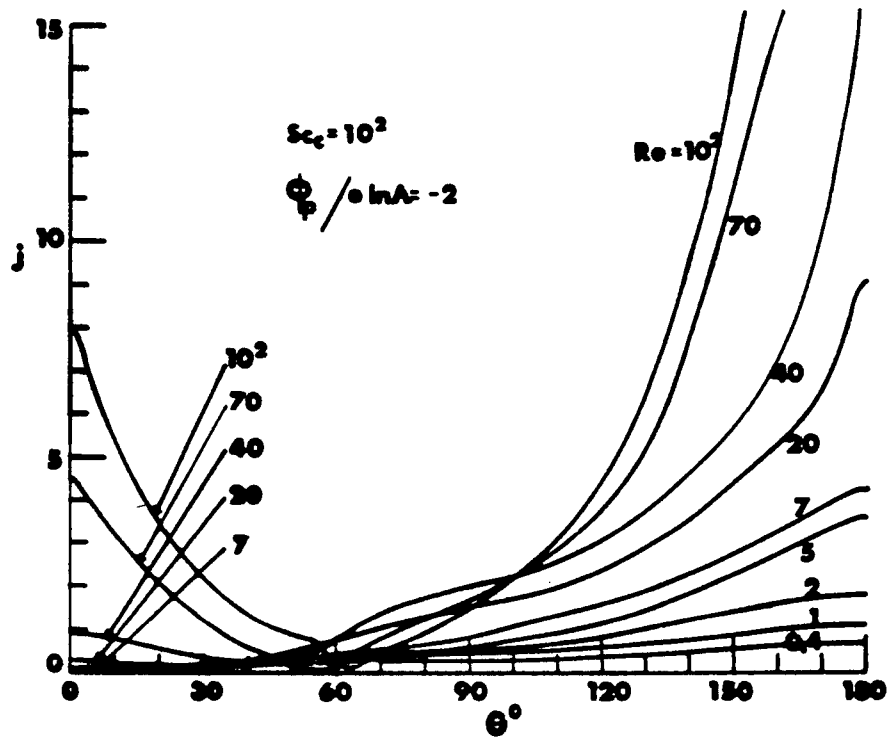


FIGURE 5.4f Angle dependence of local current for various Reynolds numbers. $Sc_c = 10^2$, $\phi_p / \epsilon \ln A = -2$.

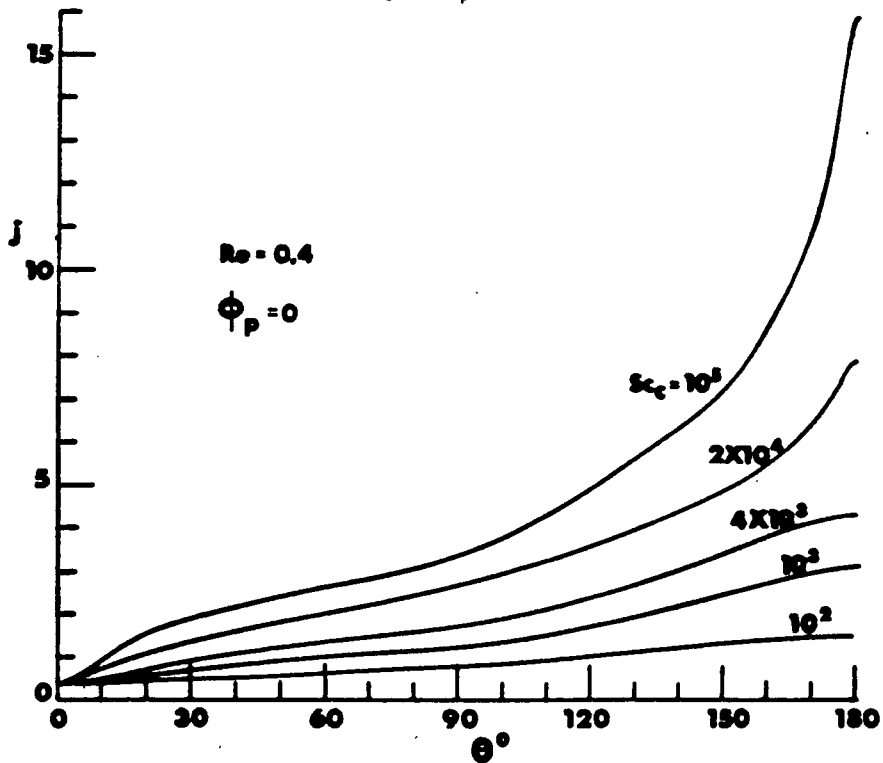


FIGURE 5.5 Angle dependence of local current to cylinder in cross-flow for various charged particle Schmidt numbers. (a) $Re = 0.4$, $\phi_p / \epsilon \ln A = 0$ (b) $Re = 0.4$, $\phi_p / \epsilon \ln A = 4$ (c) $Re = 0.4$, $\phi_p / \epsilon \ln A = -4$ (d) $Re = 20$, $\phi_p / \epsilon \ln A = 0$ (e) $Re = 20$, $\phi_p / \epsilon \ln A = 2$ (f) $Re = 20$, $\phi_p / \epsilon \ln A = -4$.

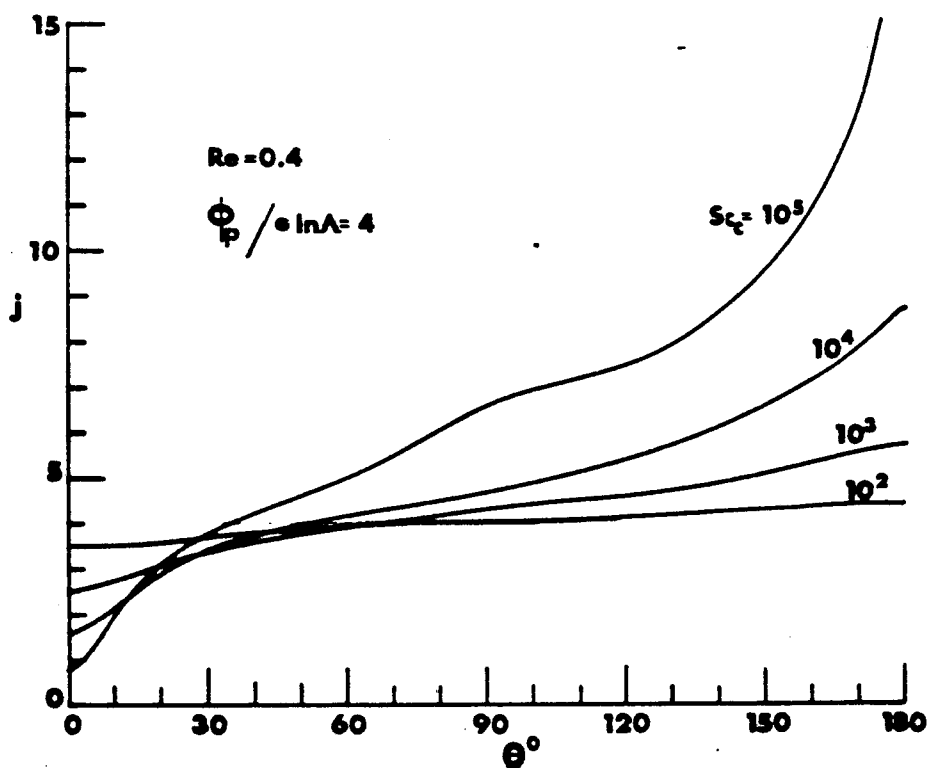


FIGURE 5.5b Angle dependence of local current for various charged particle Schmidt numbers. $Re=0.4$, $\phi_p / \epsilon \ln \Lambda = 4$.

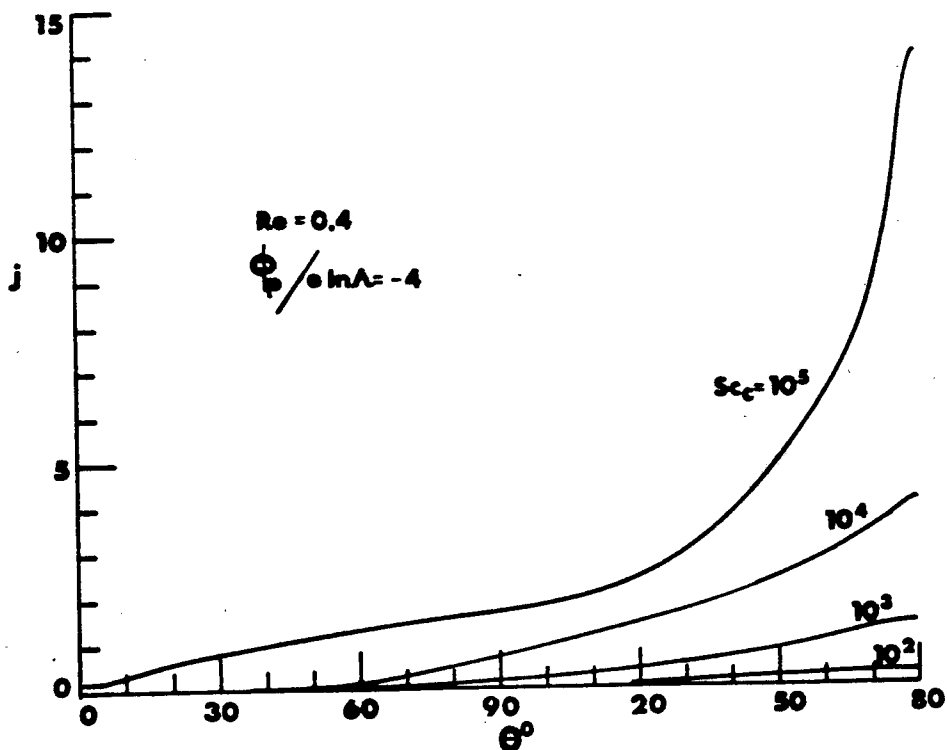


FIGURE 5.5c Angle dependence of local current for various charged particle Schmidt numbers. $Re=0.4$, $\phi_p / \epsilon \ln \Lambda = -4$.

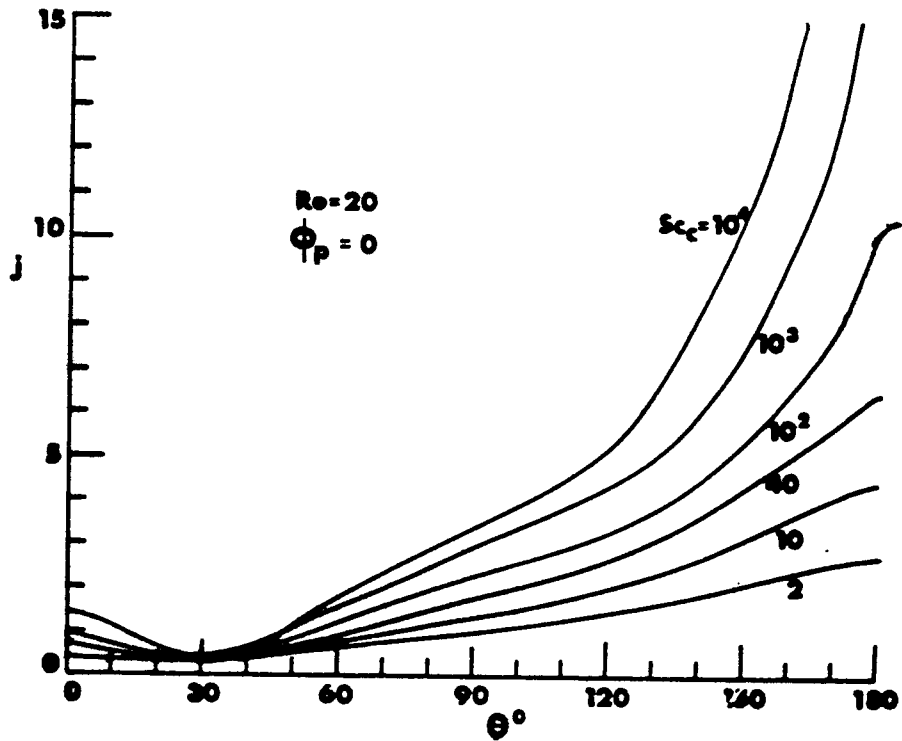


FIGURE 5.5d Angle dependence of local current for various charged particle Schmidt numbers. $Re=20$, $\phi_p / \epsilon \ln \Lambda = 0$.

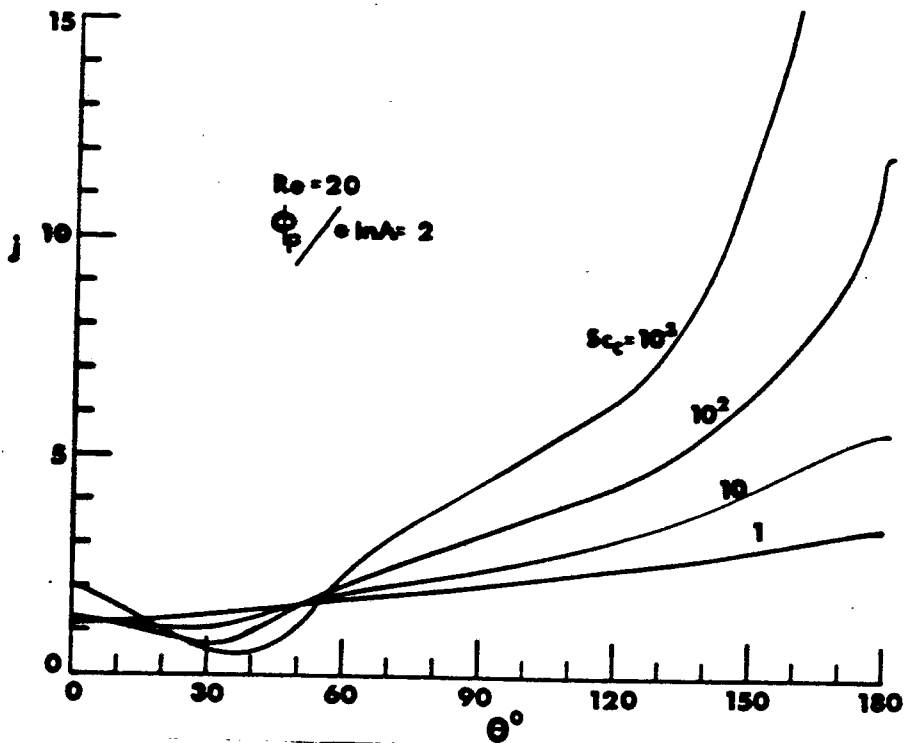


FIGURE 5.5e Angle dependence of local current for various charged particle Schmidt numbers. $Re=20$, $\phi_p / \epsilon \ln \Lambda = 2$.

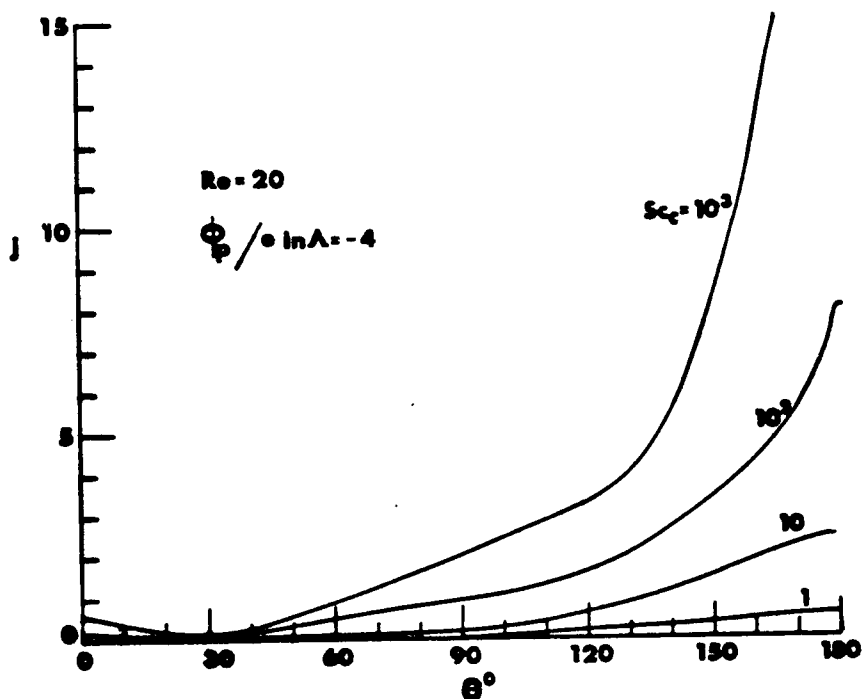


FIGURE 5.5f Angle dependence of local current for various charged particle Schmidt numbers. $Re=20$, $\phi_p / \epsilon \ln A = -4$.

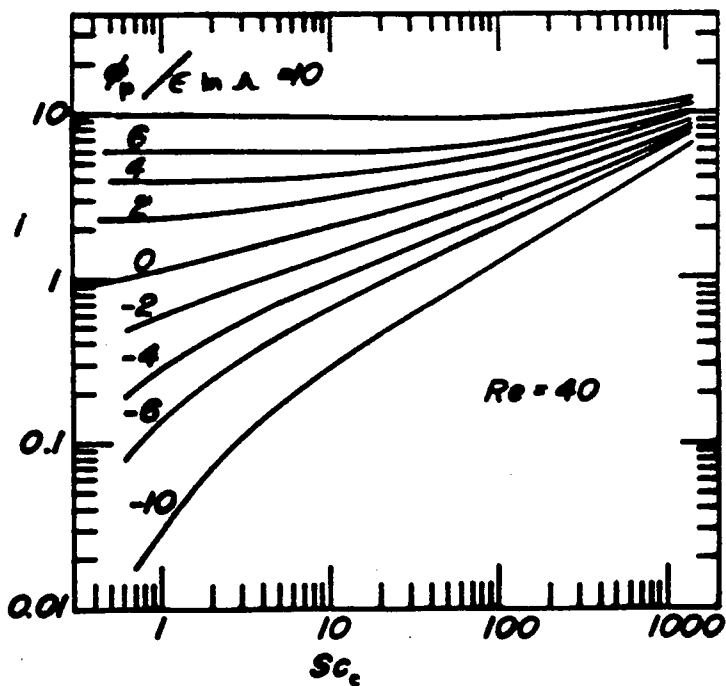


FIGURE 5.6 Nondimensional probe current $i = I/I_d$ as a function of charged particle Schmidt number for various surface potentials for cylinder in cross-flow with $Re=40$.

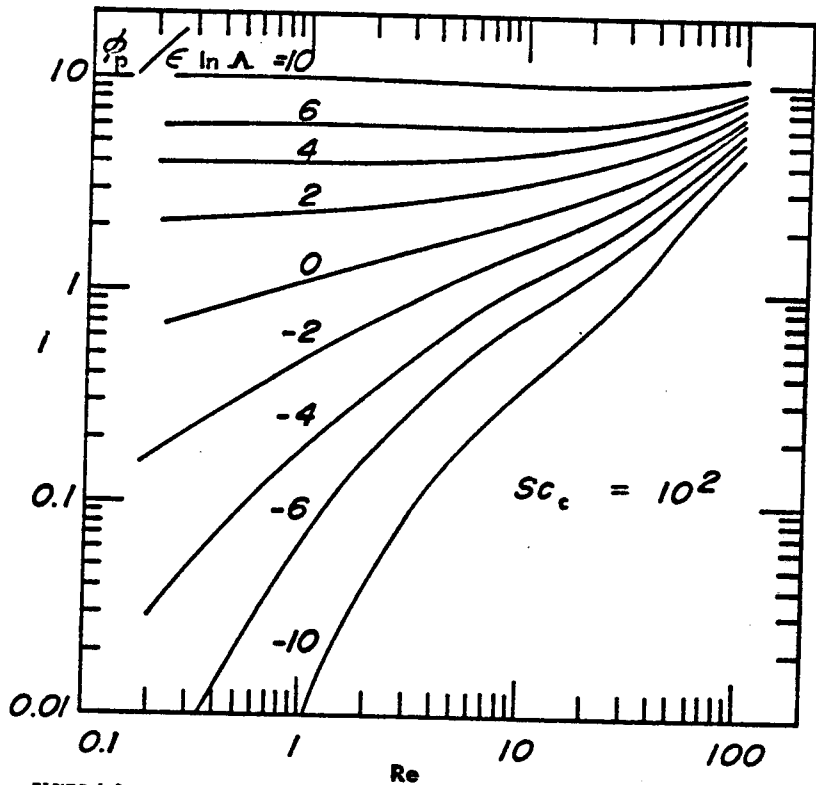


FIGURE 5.7 Nondimensional probe current as a function of Reynolds number for various surface potentials for cylinder in cross-flow with $Sc_c = 10^2$.

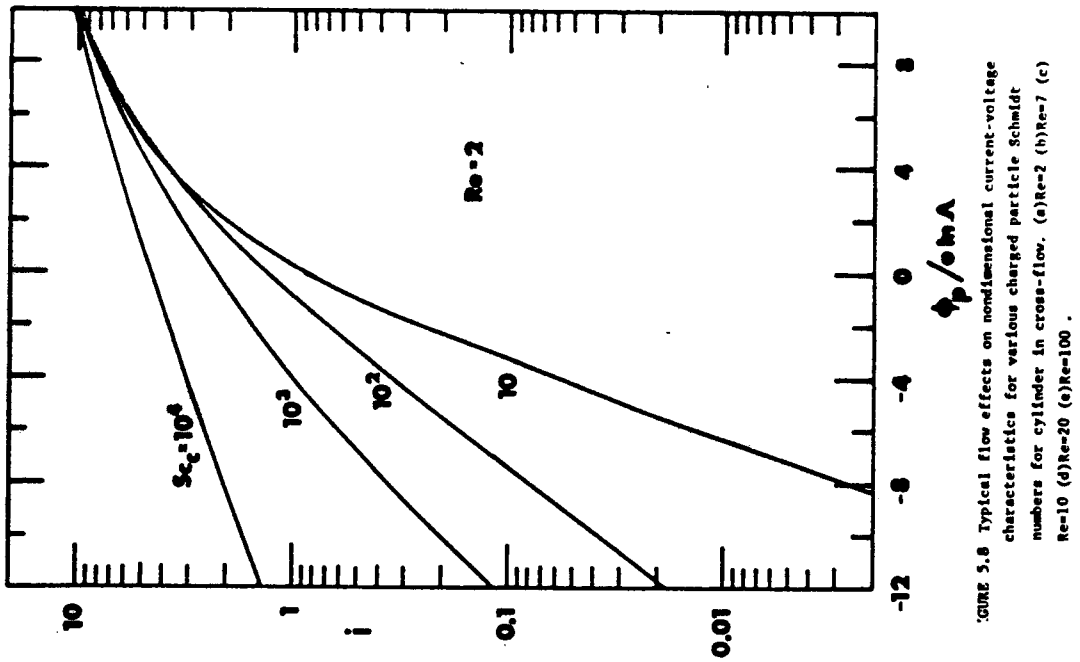


FIGURE 5.8 Typical flow effects on nondimensional current-voltage characteristics for various charged particle Schmidt numbers for cylinder in cross-flow. (a) $Re=2$ (b) $Re=7$ (c) $Re=10$ (d) $Re=20$ (e) $Re=100$.

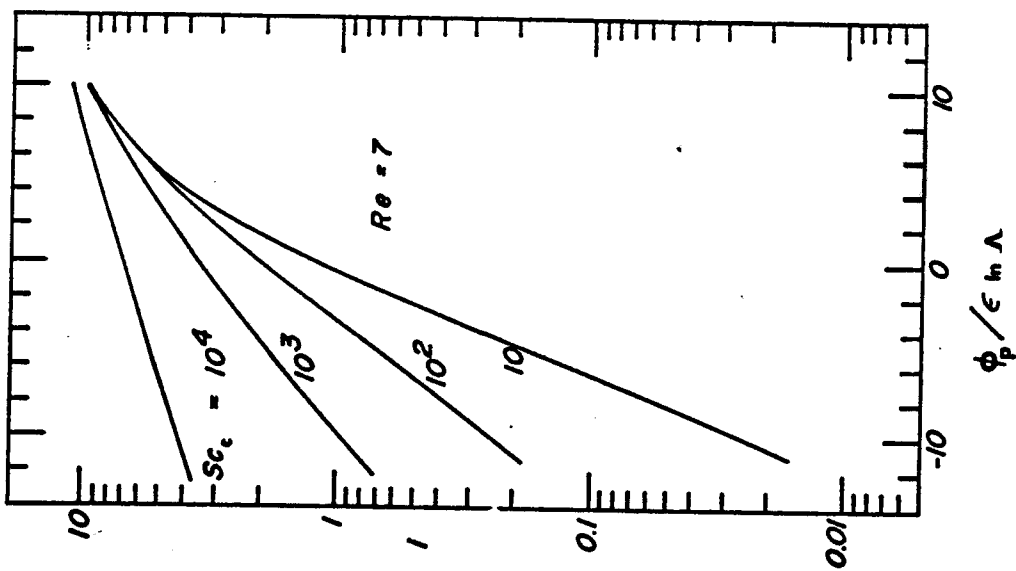


FIGURE 5.8b Nondimensional current-voltage characteristics for various charged particle Schmidt numbers. $Re=7$.

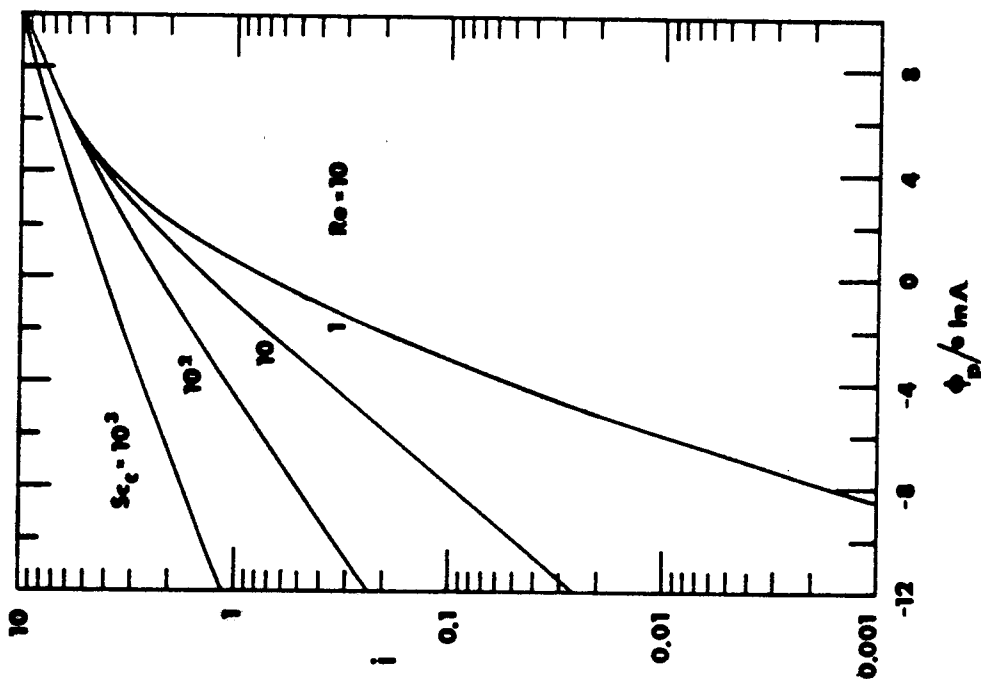


FIGURE 5.8c Nondimensional current-voltage characteristics for various charged particle Schmidt numbers. $Re=10$.

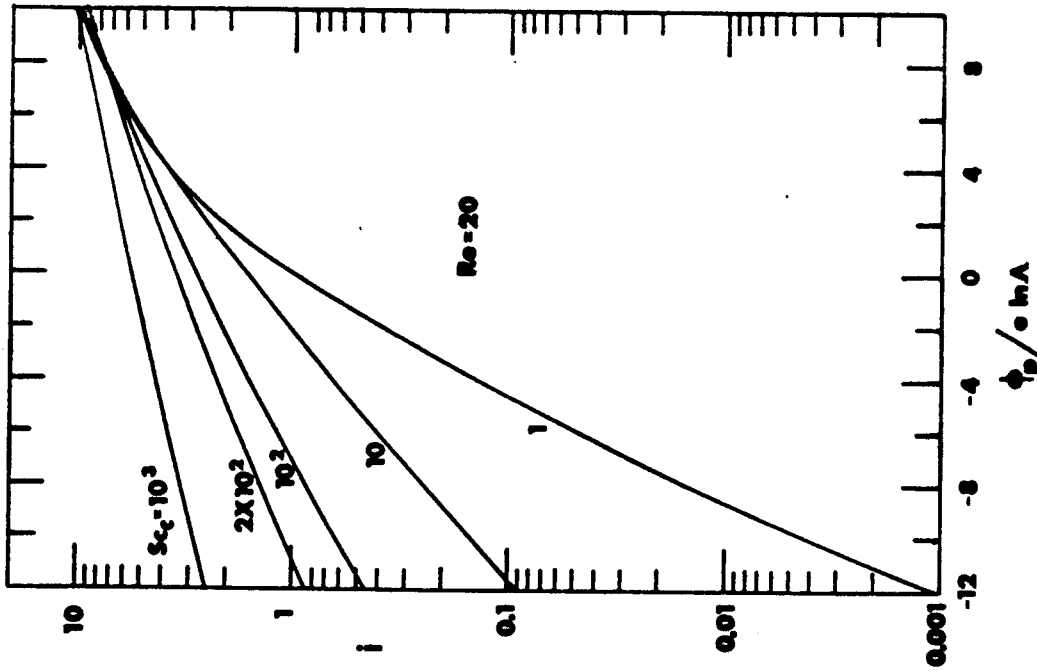


FIGURE 5.64 Nondimensional current-voltage characteristics for various charged particle Schmidt numbers. $Re=20$.

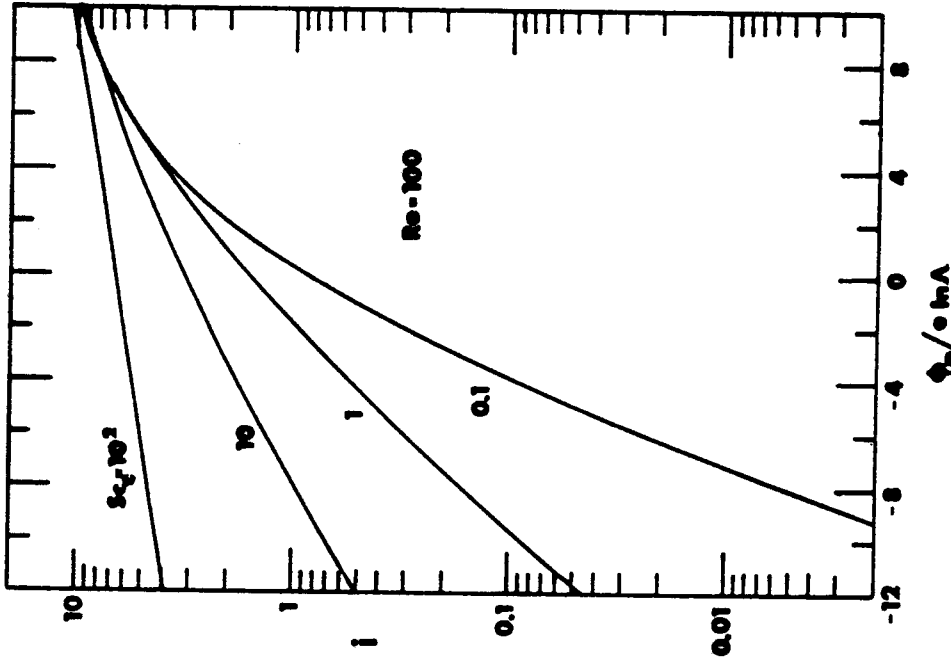


FIGURE 5.6e Nondimensional current-voltage characteristics for various charged particle Schmidt numbers. $Re=100$.

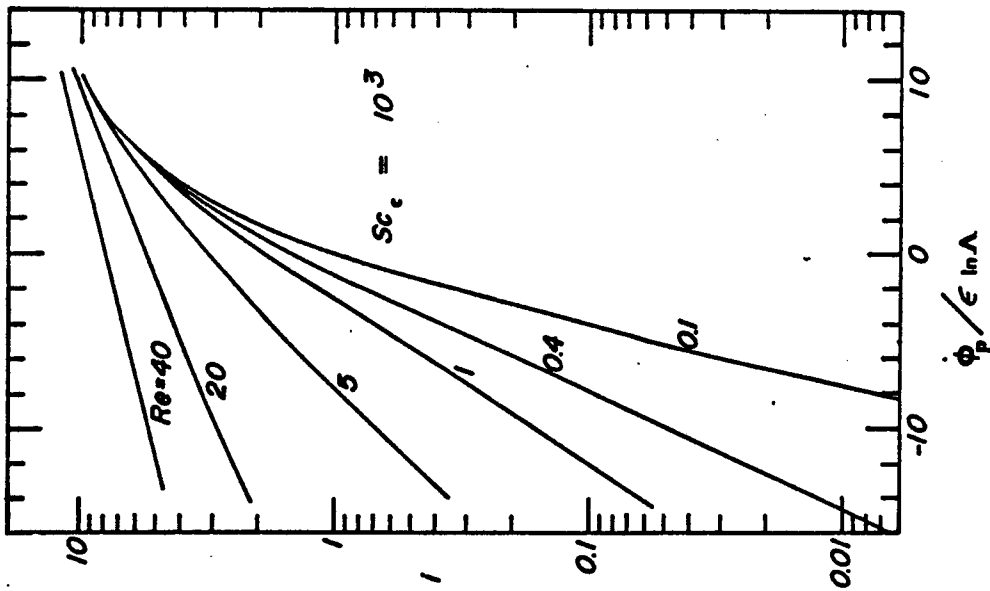


FIGURE 5.9 Nondimensional current-voltage characteristics for various Reynolds numbers for cylinder in cross-flow, $Sc_c = 10^3$.

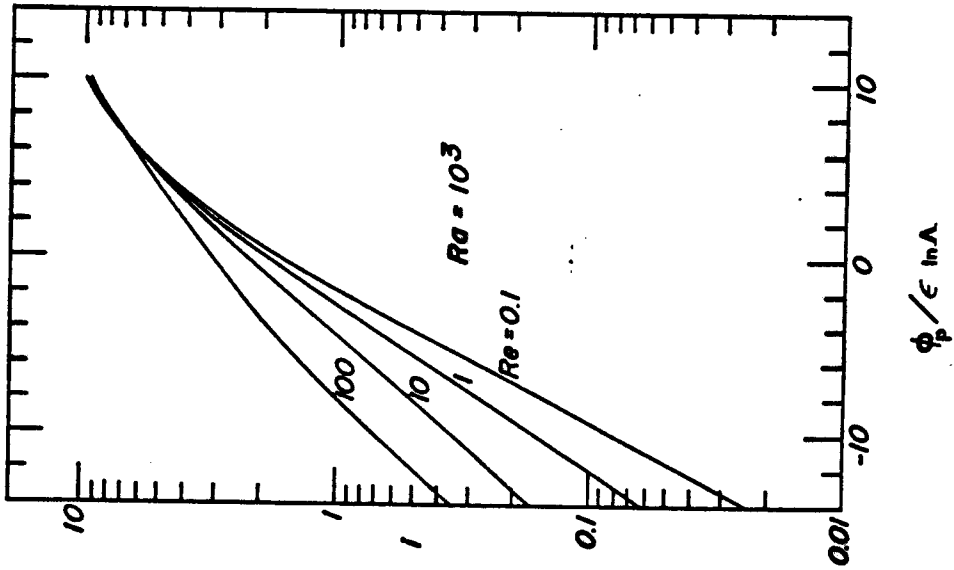


FIGURE 5.10 Comparison of Reynolds number effects on nondimensional current-voltage characteristics at diffusion Reynolds number $Ra=10^3$.

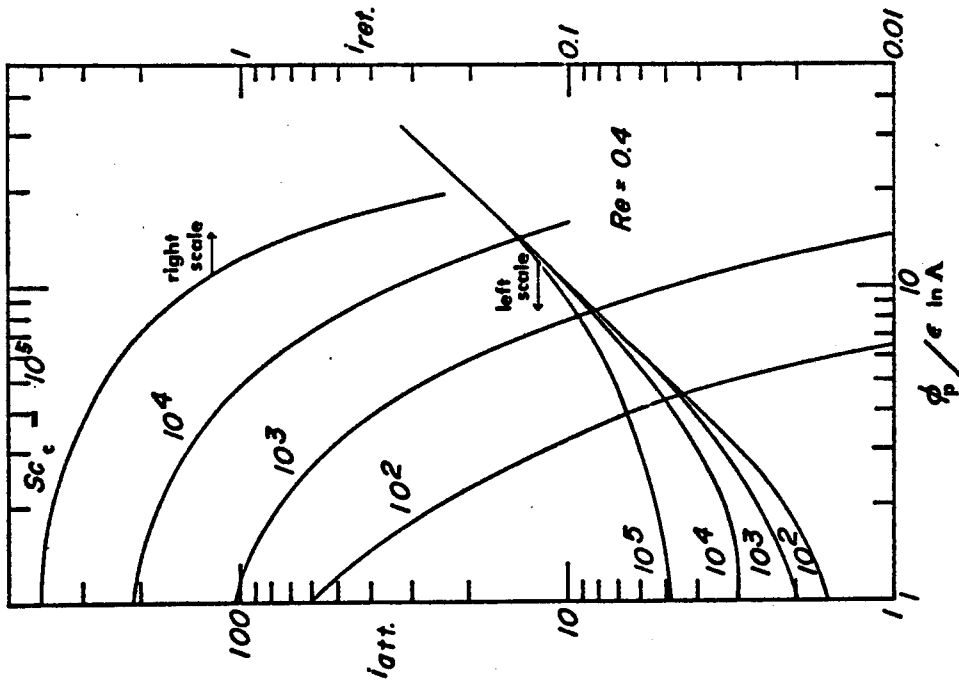


FIGURE 5.11 Attracted i_{att} and retarded i_{ret} current characteristics for various charged particle Schmidt numbers for cylinder in cross-flow, $Re=0.4$.

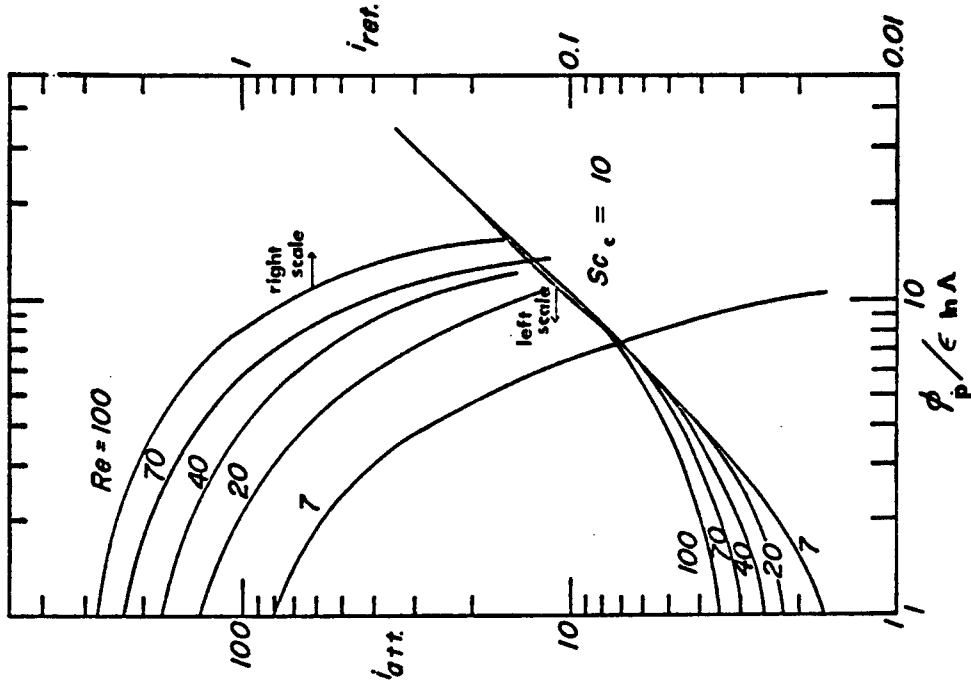


FIGURE 5.12 Attracted and retarded current characteristics for various Reynolds numbers for cylinder in cross-flow, $Sc_c=10$.

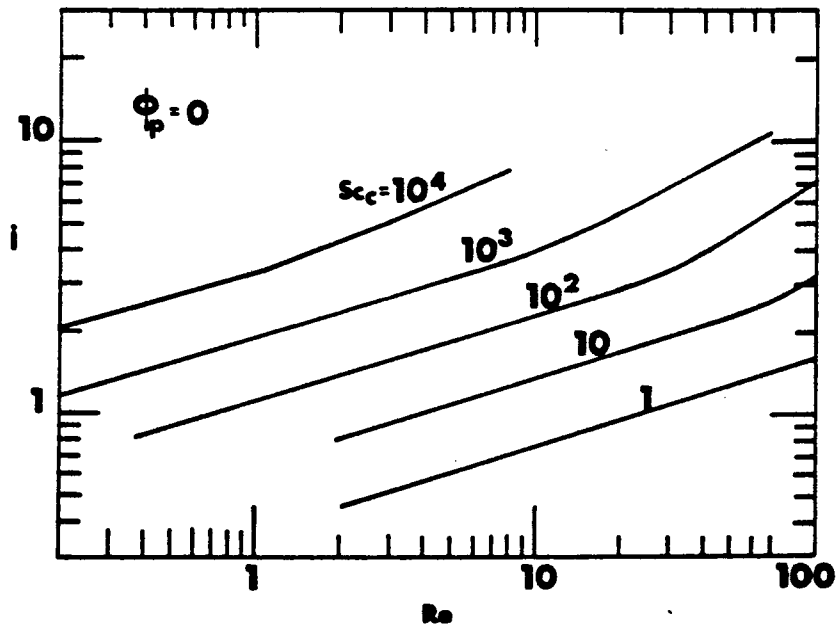


FIGURE 5.13 Nondimensional probe current as a function of Reynolds number for various charged particle Schmidt numbers for cylinder in cross-flow at space potential.

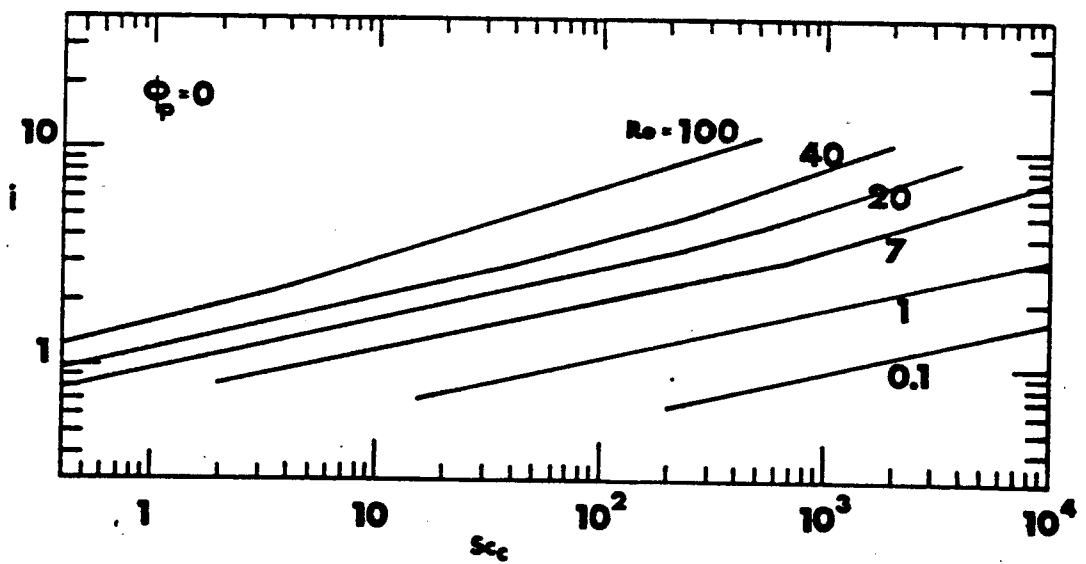


FIGURE 5.14 Nondimensional probe current as a function of charged particle Schmidt number for various Reynolds numbers for cylinder in cross-flow at space potential.

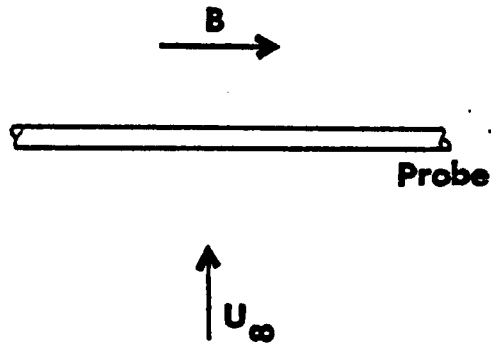


FIGURE 5.15 Application of present theory to magneto-plasma (Sec. 5.4).

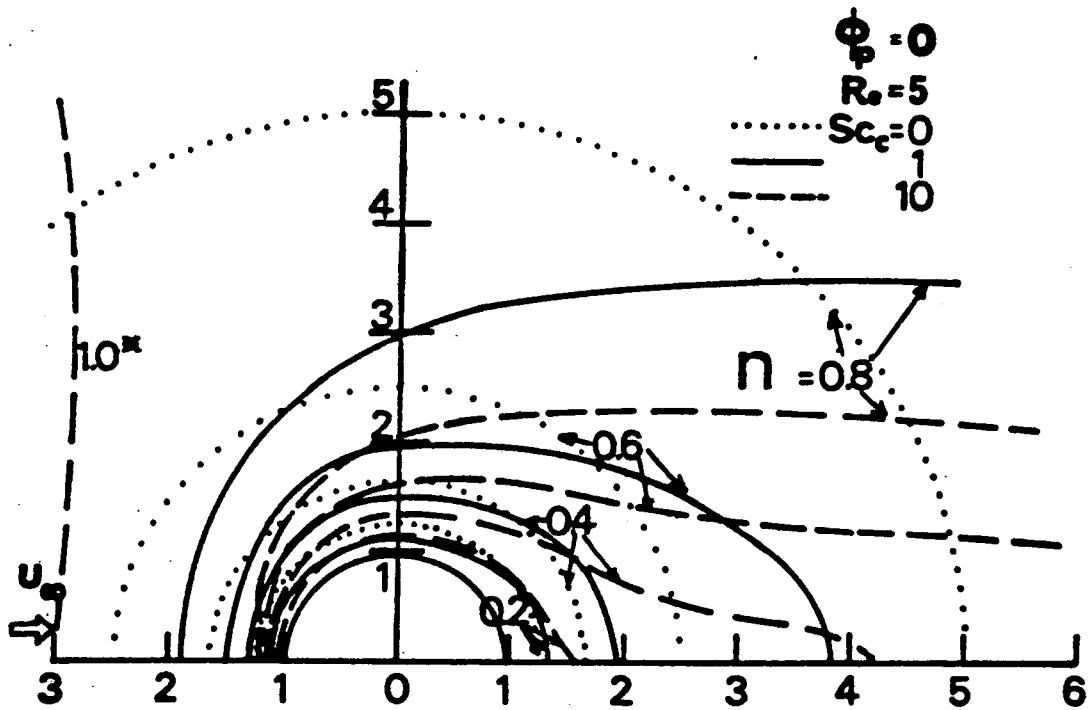


FIGURE 6.1 Charge density contour map for sphere in flow for various charged particle Schmidt numbers at $Re=5$ (flow without wake). *where we define $n=0.9999$ as 1.0 ,

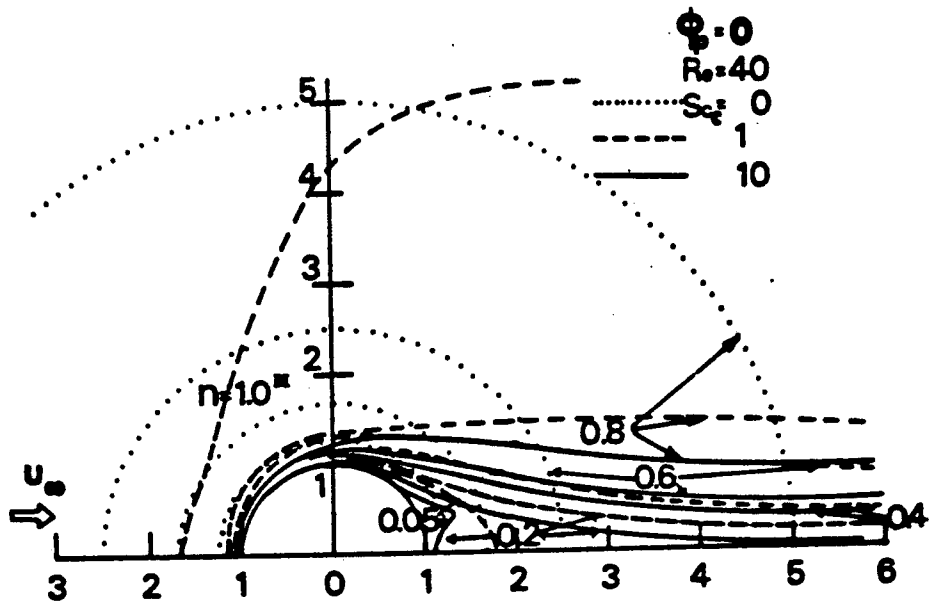


FIGURE 6.2 Charge density contour map for sphere in flow for various charged particle Schmidt numbers at $Re=40$ (flow with wake).

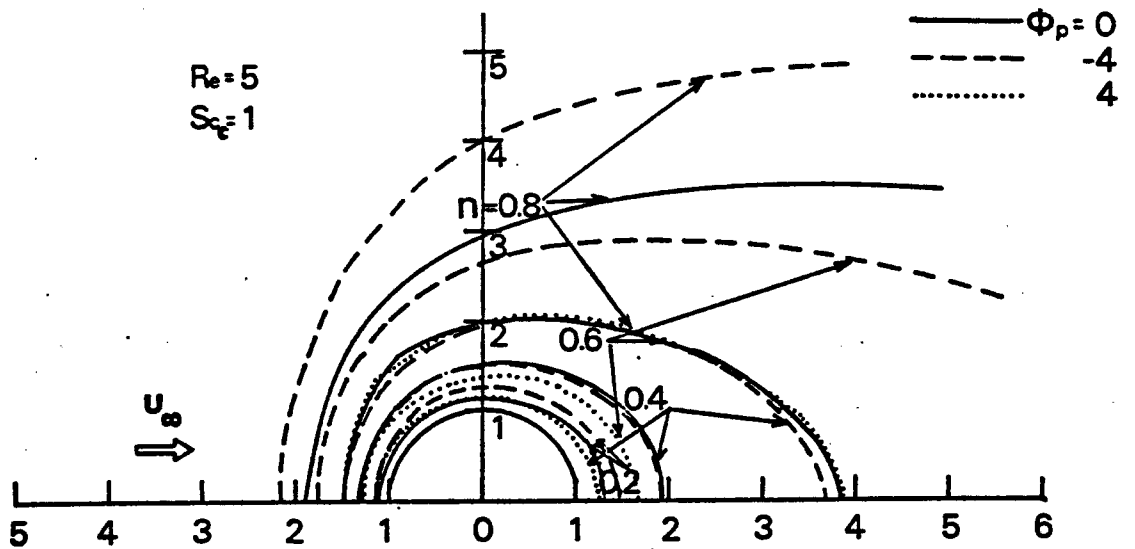


FIGURE 6.3 Surface potential effects on charge density contour map at $Re=5, Sc_c=1$.

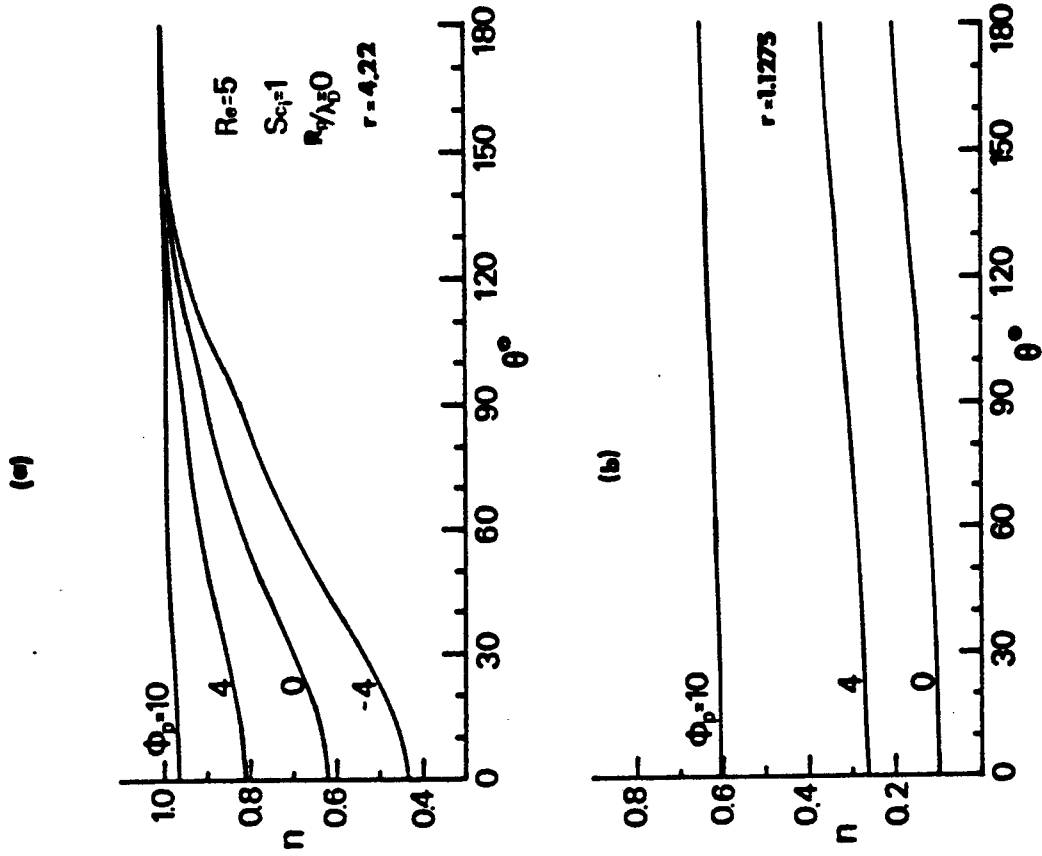


FIGURE 6.4 Angle dependence of charge density for sphere at various surface potentials at radius (a)4.22 (b) 1.1275.

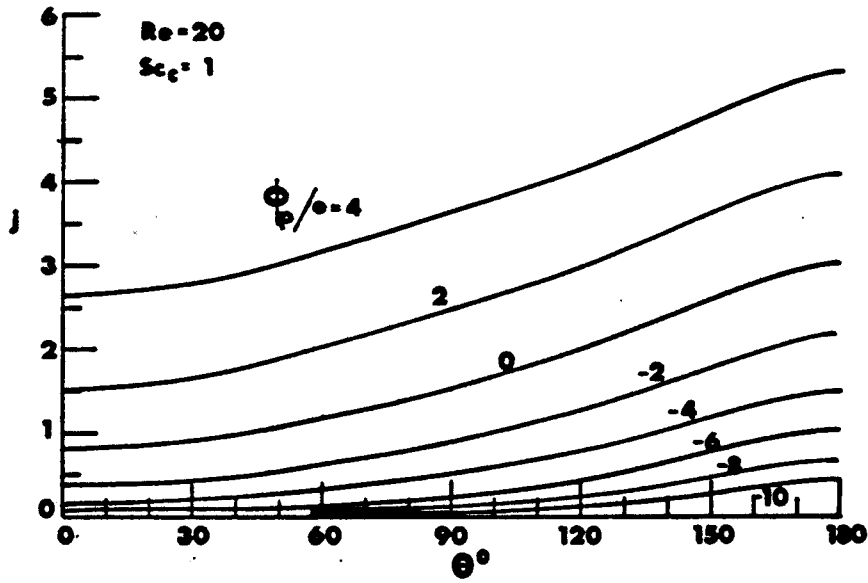


FIGURE 6.5 Angle dependence of local current to sphere for various surface potentials (a) $Re=20, Sc_c=1$ (b) $Re=60, Sc_c=1$.

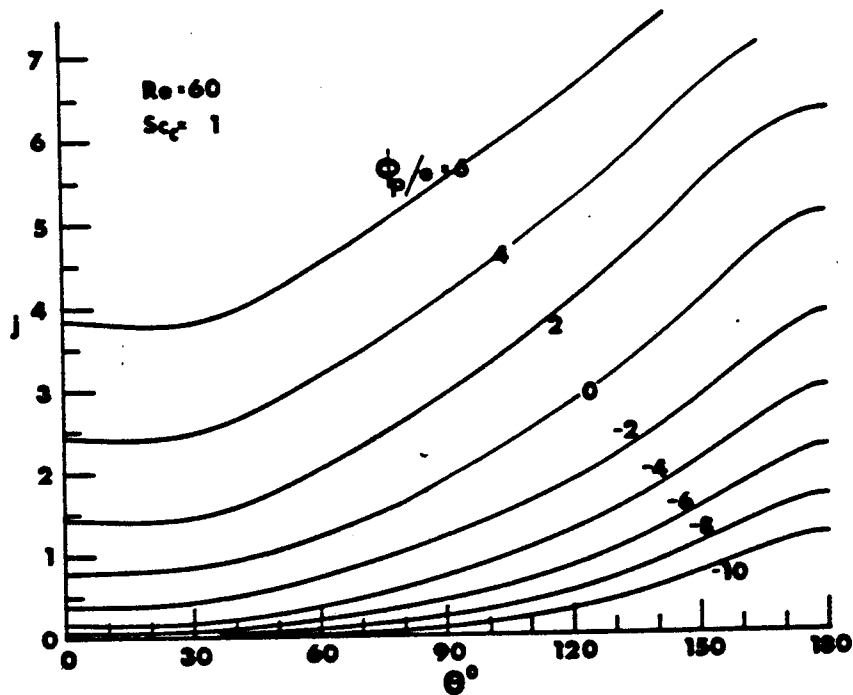


FIGURE 6.5b Angle dependence of local current for various surface potentials, Re=60, Sc_c=1.

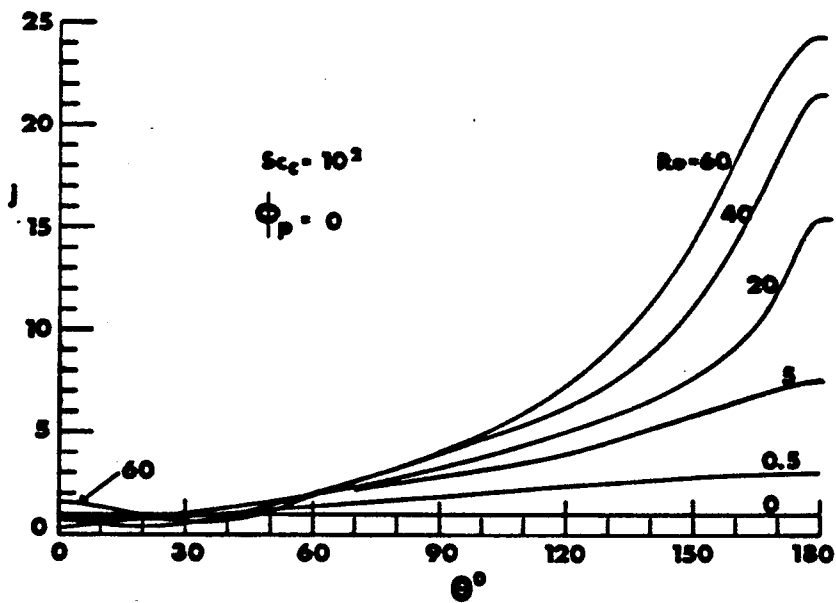


FIGURE 6.6a Angle dependence of local current to sphere for various Reynolds numbers, Sc_c=10² (a) $\phi_p/\mu=0$ (b) $\phi_p/\mu=2$ (c) $\phi_p/\mu=4$.

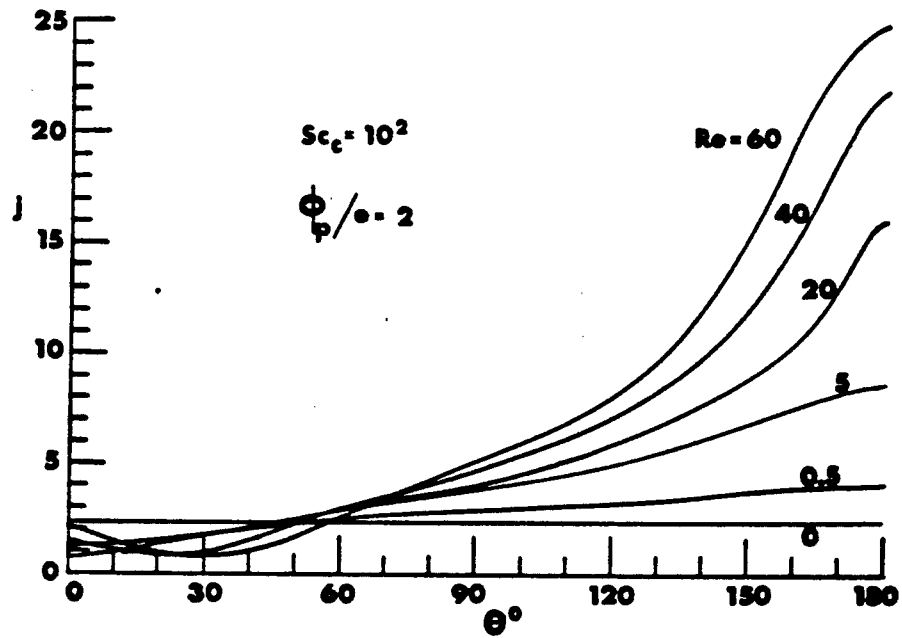


FIGURE 6.6b Angle dependence of local current for various Reynolds numbers, $Sc_c = 10^2$, $\phi_p/\epsilon = 2$.

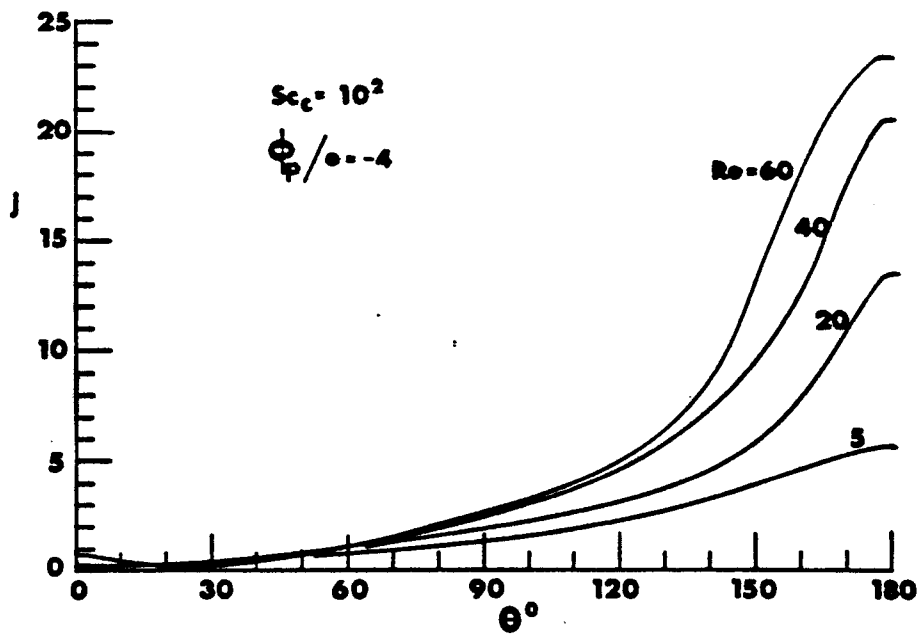


FIGURE 6.6c Angle dependence of local current for various Reynolds numbers at $Sc_c = 10^2$, $\phi_p/\epsilon = 4$.

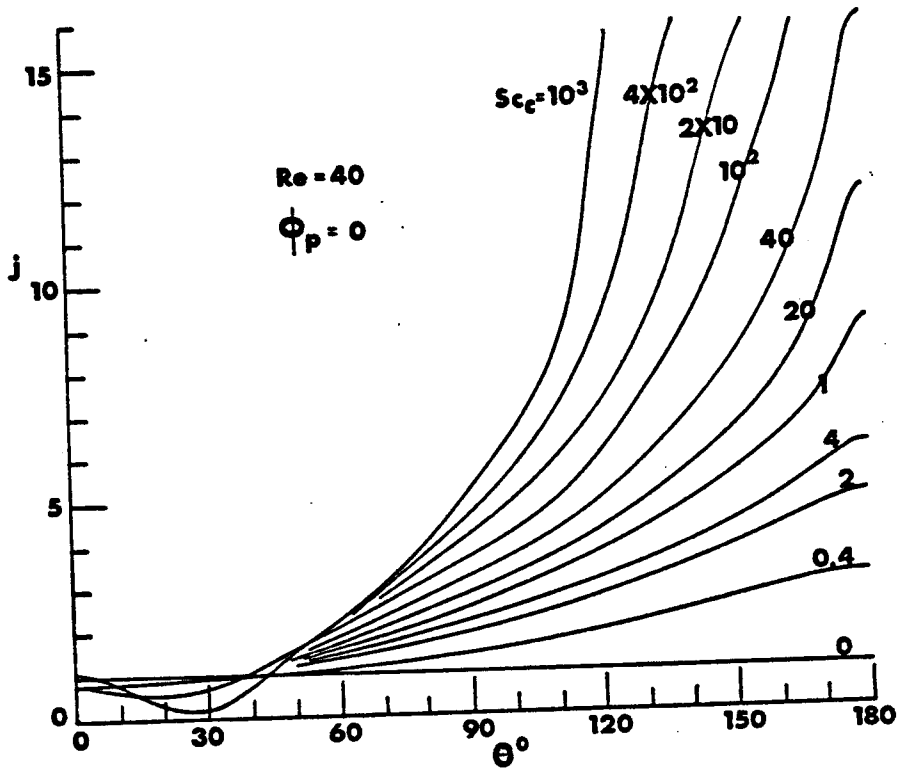


FIGURE 6.7 Angle dependence of local current to sphere for various charged particle Schmidt numbers at $Re=40$ (a) $\phi_p/a=0$ (b) $\phi_p/a=2$ (c) $\phi_p/a=-2$.

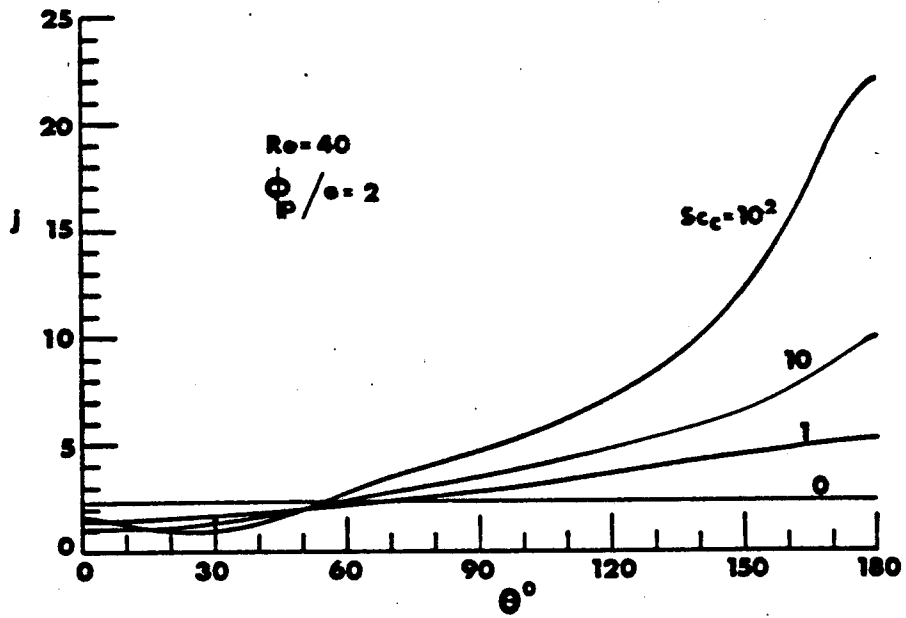


FIGURE 6.7b Angle dependence of local current for various charged particle Schmidt numbers at $Re=40$, $\phi_p/a=2$.

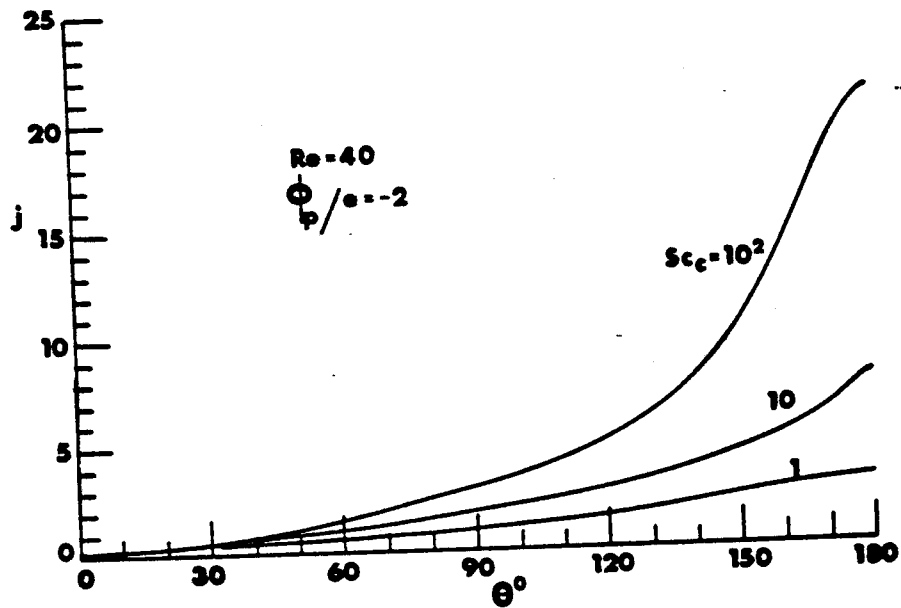


FIGURE 6.7c Angle dependence of local current for various charged particle Schmidt numbers at $Re=40$, $\Phi_p/e=-2$.

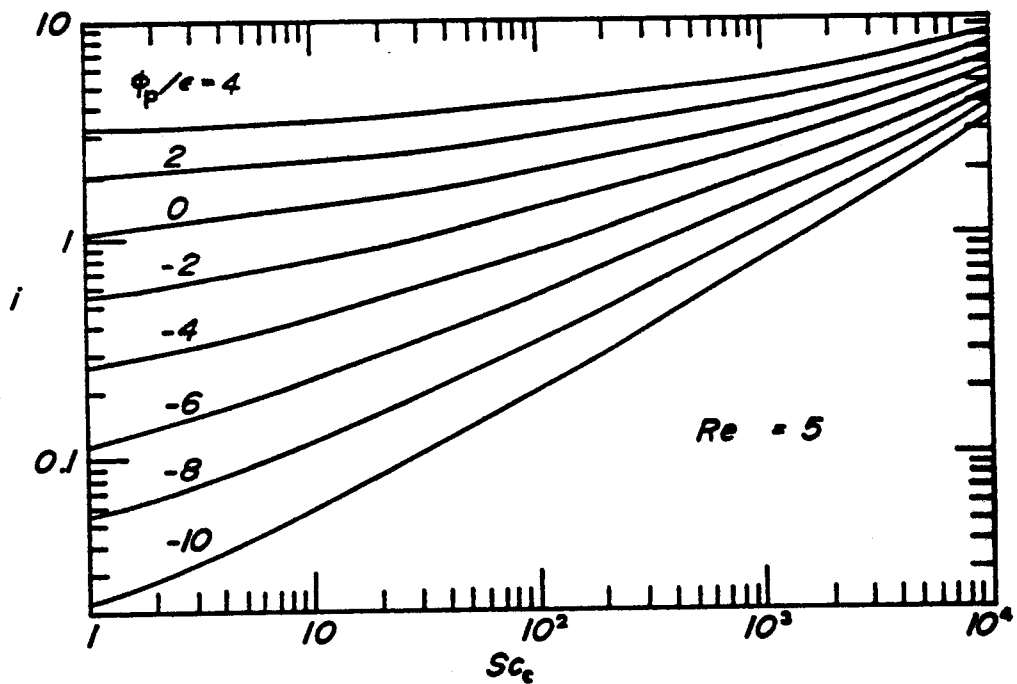


FIGURE 6.8 Nondimensional probe current as a function of charged particle Schmidt number for various surface potentials for sphere, $Re=5$.

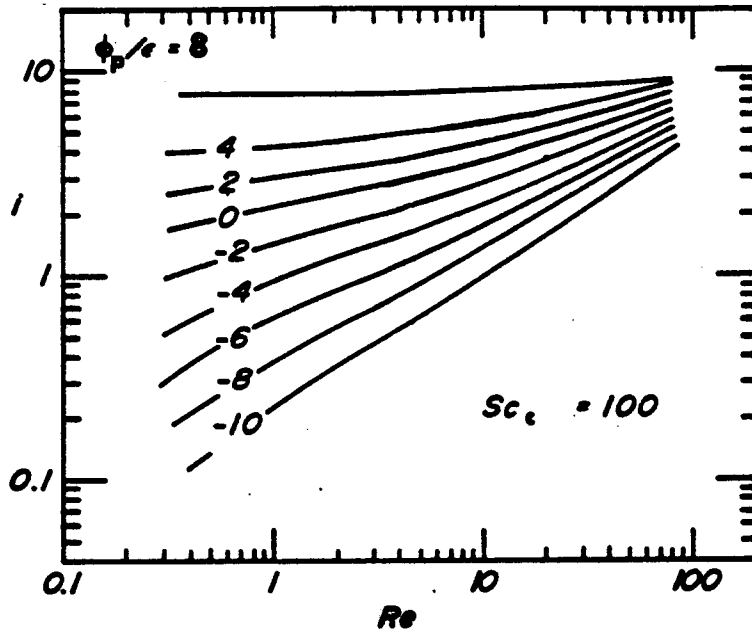


FIGURE 6.9 Nondimensional probe current as a function of Reynolds number for various surface potentials for sphere at $Sc_c = 10^2$.

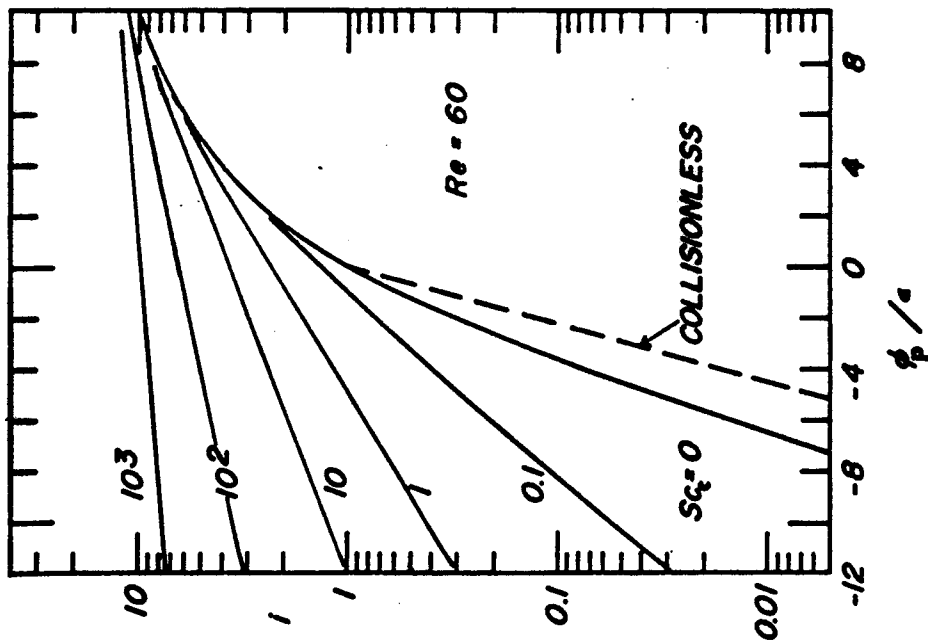


FIGURE 6.10 Nondimensional current-voltage characteristics for various charged particle Schmidt numbers for sphere. $Re=60$. The result for $Sc_c=0$ is given by Eq. B.1.

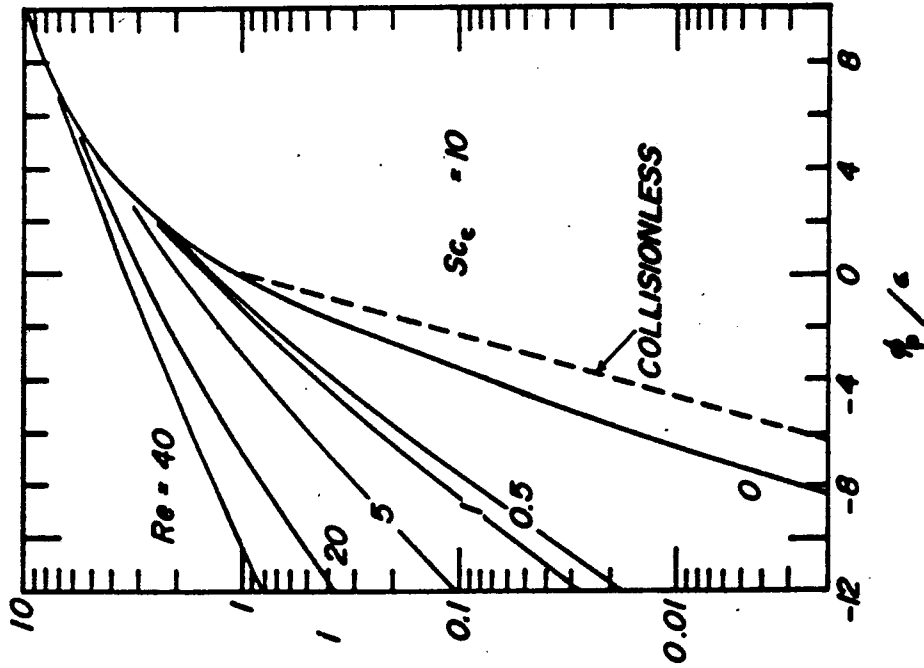


FIGURE 6.11 Nondimensional current-voltage characteristics for various Reynolds numbers for sphere, $Sc_c=10$. The result for $Re=0$ is given by Eq. 3.1.

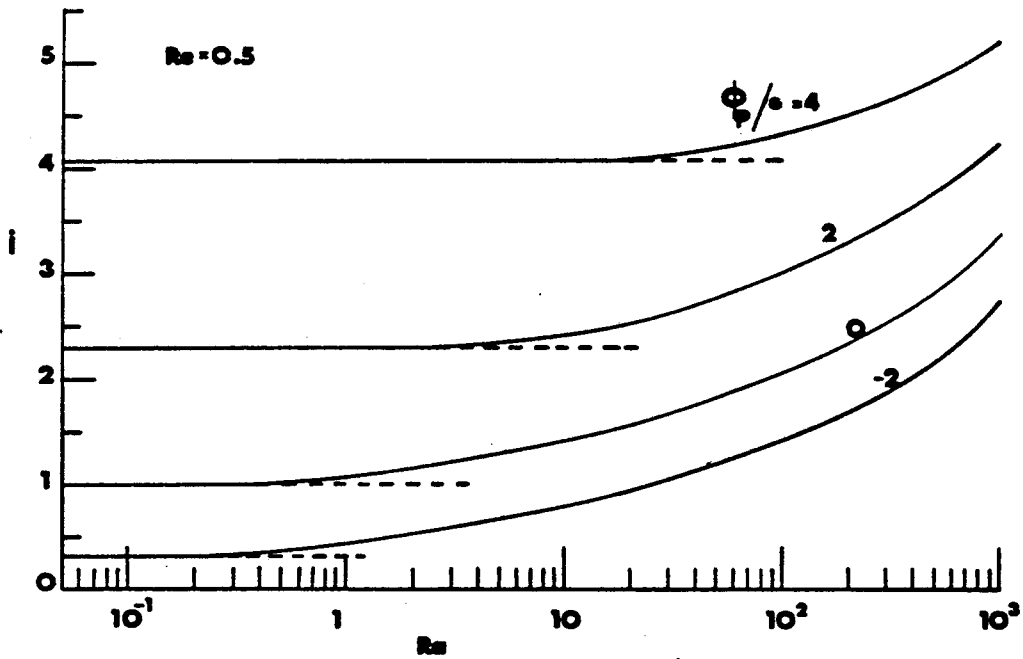


FIGURE 6.12 Nondimensional current as a function of diffusion Reynolds number for various surface potentials at $Re=0.5$.

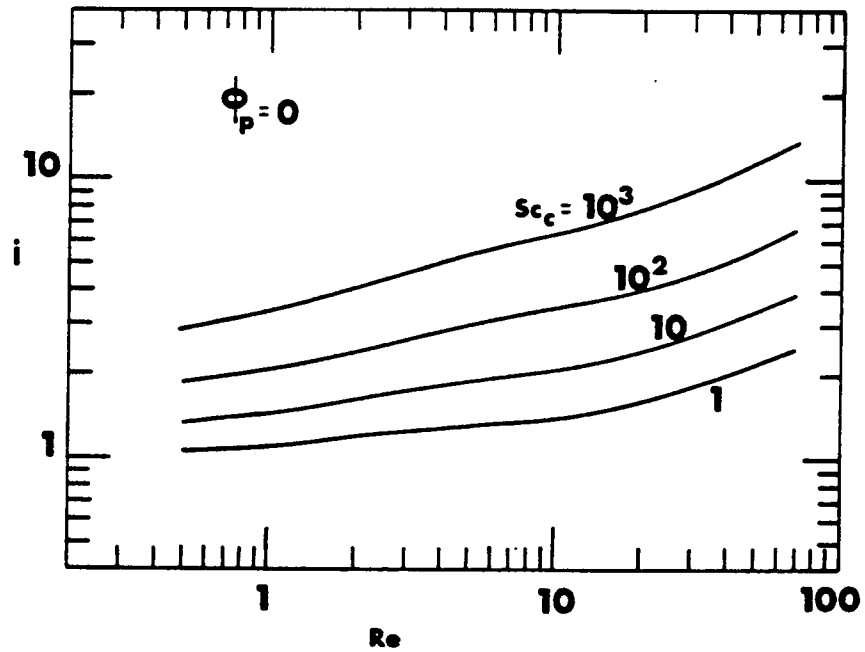


FIGURE 6.13 Nondimensional probe current as a function of Reynolds number for various charged particle Schmidt numbers for sphere in flow at space potential.

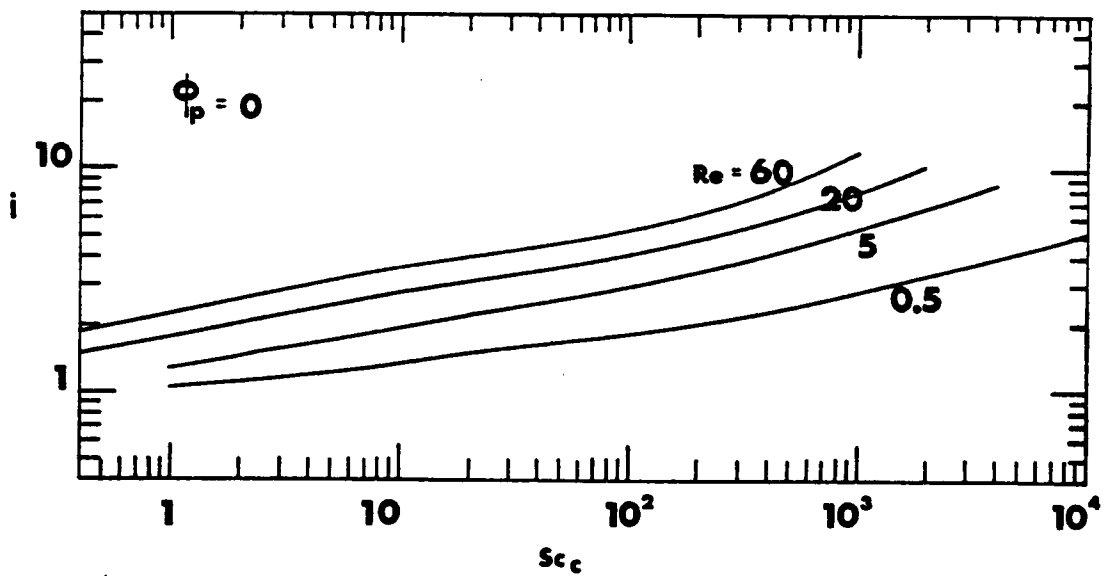


FIGURE 6.14 Nondimensional probe current as a function of charged particle Schmidt number for various Reynolds numbers for sphere in flow at space potential.

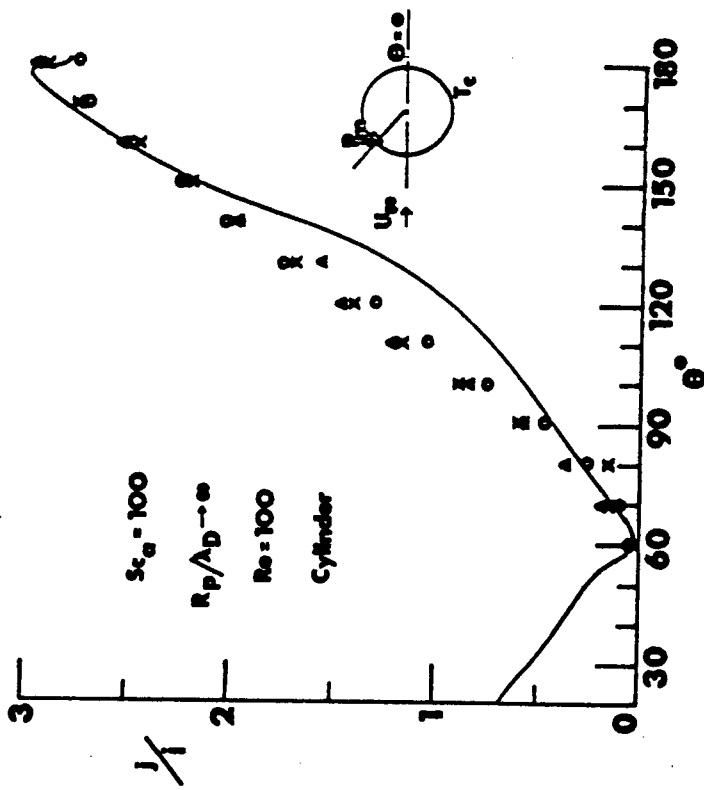


FIGURE 7.2 Comparison of the ratio of local current density to total current of present work with experiment of Tsuji and Hirano (1973), where P_m is their probe for local ion current measurement and T_c is the test cylinder in their experiment. — present work at $Sc_a = 100, R_p/L_D \rightarrow \infty, Re = 100$.
 Experimental data : ooo $Re = 87, Sc_a = 1.02 \times 10^2, L = 5, R_p/L_D = 10^3$.
 xxx $Re = 115, Sc_a = 1.07 \times 10^2, L = 3.75, R_p/L_D = 10^3, \text{aaa } Re = 166, Sc_a = 1.0 \times 10^2, L = 3, R_p/L_D = 10^3$. The quantity Sc_a is defined in Appendix A.

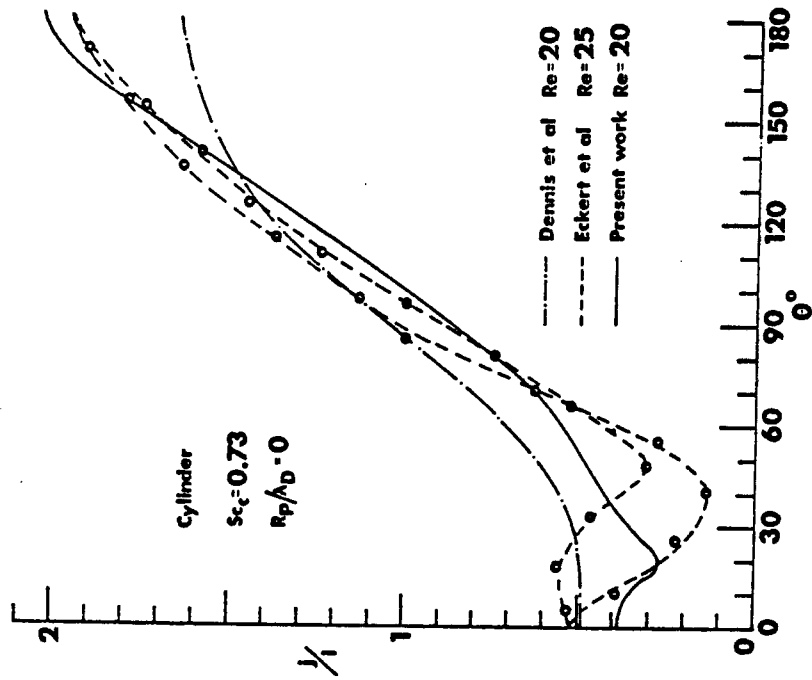


FIGURE 7.1 Comparison of the ratio of local current to total current of present work with theory of Dennis et al (1968) and experiment of Eckert and Soehngen (1952).

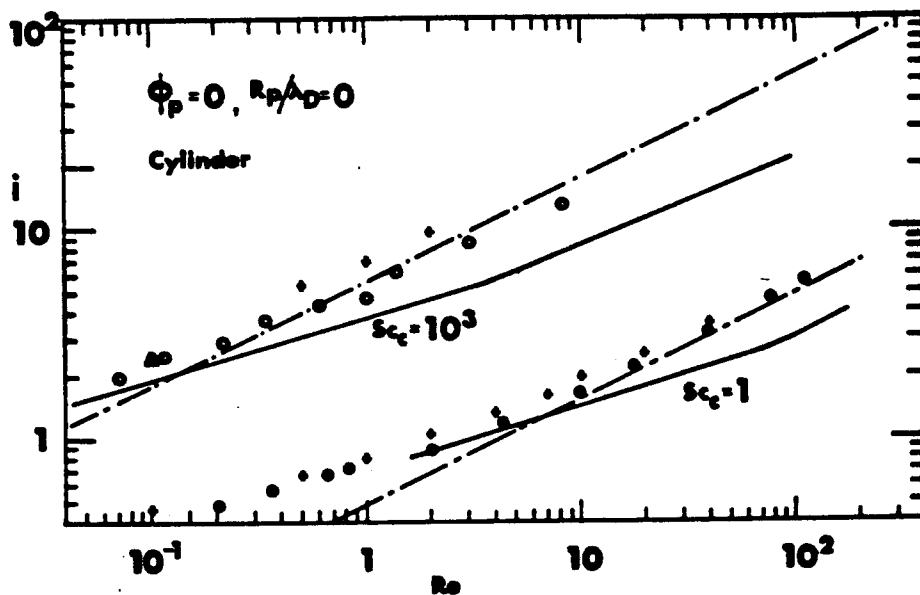


FIGURE 7.3 Comparison of total current of present work with other theories and experiments at space potential $\phi_p/\lambda_D=0$, cylinder in cross-flow. Theories: (1) — present work for $Sc_c=1$ and 10^3 (2) +++ Dennis et al (1968) for $Sc_c=0.73$ and 10^3 (3) Δ Friedlander (1957) for $Sc_c=1$. Experiments: (a) \circ Dobry and Finn (1956) for $Sc_c=1200$ (b) \square Collins and Williams (1959) for $Sc_c=0.73$ (c) \dashv experimental correlations of Jensen and Ertzius (1969).

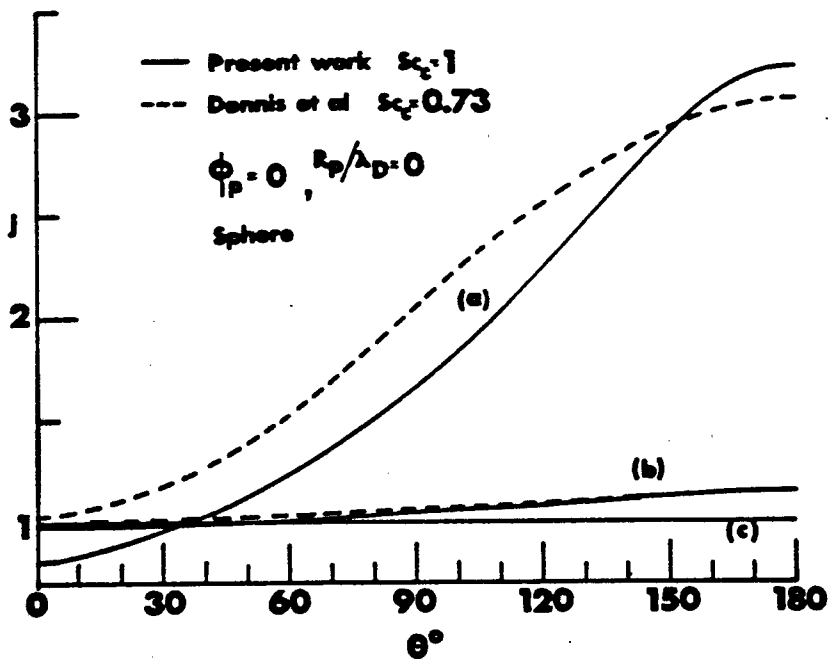


FIGURE 7.4 Comparison of local current of present work with theory of Dennis et al (1973) for sphere at space potential $\phi_p=0$ and $R_p/\lambda_D=0$. (a) $Re=20$ (b) $Re=0.5$ (c) $Re=0$.

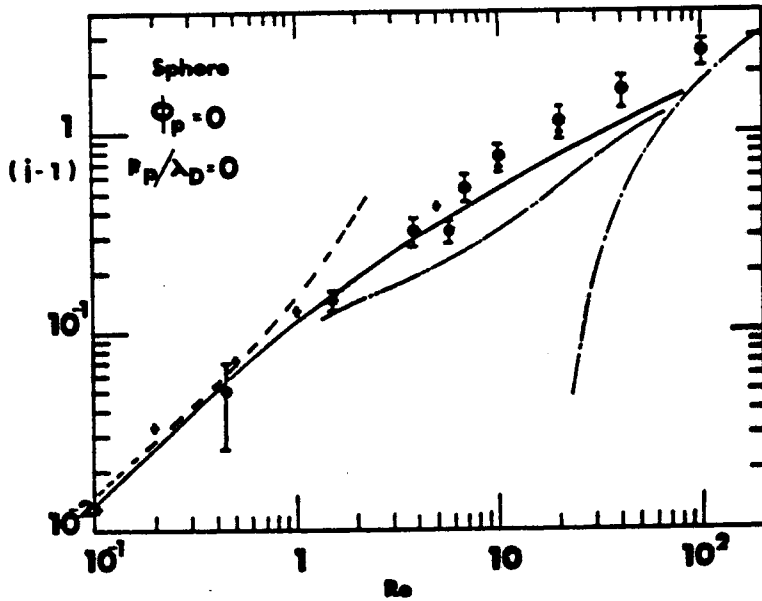


FIGURE 7.5 Comparison of total current of present work with other theories and experiments for a sphere at space potential with $R_p/\lambda_D=0$. Theory: (1)—— present work at $Sc_c=1$ (2)----- Rimmer(1968,1969) at $Sc_c=0.7$ (3)+ + Dennis et al(1973)at $Sc_c=0.73$ (4)----- Gupalo and Ryzantsev (1969)at $Sc_c=1$ (5)see Yuge (1956)at $Sc_c=0.73$ (6)----- Williams(1954)at $Sc_c=0.73$. Experiment: (a) oo Yuge(1960) at $Sc_c=0.73$.

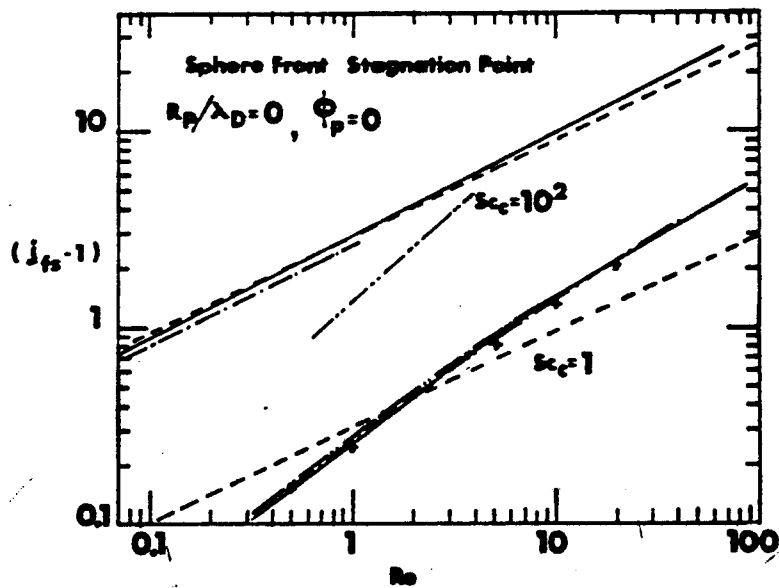


FIGURE 7.6 Comparison of front stagnation current density j_{fs} of present work with other theories for a sphere at space potential with $R_p/\lambda_D=0$. (1)—— present work for $Sc_c=1$ and 10^2 (2)----- Eckart and Drake (1972) for $Sc_c=1$ and 10^2 (3)----- Kodera(1975) for $Sc_c=1$ and 10^2 (4)----- Gupalo and Ryzantsev (1969)for $Sc_c=1$ and 10^2 (5)+ + Dennis et al (1973) at $Sc_c=0.73$.

CRPE
*Centre de Recherches
en Physique de l'Environnement
terrestre et planétaire*

*Avenue de la Recherche scientifique
45045 ORLEANS CEDEX*

Département PCE
*Physique et Chimie
de l'Environnement*

*Avenue de la Recherche scientifique
45045 ORLEANS CEDEX*

Département ETE
*Etudes par Télédétection
de l'Environnement*

*CNET - 38-40 rue du général Leclerc
92131 ISSY-LES-MOULINEAUX*